Measurement of Electrical, Thermal, and Photo-conductivity of Nanomaterials

AJIT SINGH

A thesis submitted for the partial fulfillment of

the degree of Doctor of Philosophy

Institute of Nano Science and Technology (INST)

Knowledge City, Sector 81, SAS Nagar, Manauli PO, Mohali-140306, Punjab, India.

Indian Institute of Science Education and Research (IISER) Mohali

Knowledge City, Sector 81, SAS Nagar, Manauli PO, Mohali-140306, Punjab, India.

August 2022

Dedicated to My Family,

&

Friends

Declaration

The work presented in this thesis has been carried out by me under the guidance of Dr. Chandan Bera and Dr. Suvankar Chakraverty at the Institute of Nano Science and Technology, Mohali, India. This work has not been submitted in part or in full for a degree, a diploma, or a fellowship to any other university or institute. Whenever contributions of others are involved, every effort is made to indicate this clearly, with due acknowledgment of collaborative research and discussions. This thesis is a bonafide record of original work done by me and all sources listed within have been detailed in the bibliography.

Ajit Singh

(Candidate)

In my capacity as the supervisor of the candidate's Ph.D. thesis work, I certify that the above statements by the candidate are true to the best of my knowledge.

Dr. Chandan Bera

(Thesis Supervisor)

Acknowledgment

This thesis summarizes my research work in the Group of Dr. Chandan Bera at the "Institute of Nano Science and Technology-Mohali" from 2017 to 2022. At the end of my five-year Ph.D. career, I would like to express my heartful gratitude to the people who have been part of this beautiful journey of my Ph.D. This thesis would not have been possible without all these people and their constant encouragement.

First of all, I would like to express my sincere gratitude to my Ph.D. supervisor, **Dr. Chandan Bera,** for their constant support, encouragement, and guidance throughout my Ph.D. His deep insights and extensive knowledge about the subject proved to be of great help. I admire how he teaches many complicated things and gives freedom to work in different aspects without any pressure. Insightful discussions with him and his excellent guidance were a perfect opportunity for me to excel in my scientific and academic pursuits. I sincerely thank my Ph.D. co-supervisor **Dr. Suvankar Chakraverty** for his kind help and cooperation throughout my study period. I am highly obliged to have research collaborations and scientific discussions with him during my work.

I also place on record my sense of gratitude to my thesis and annual review committee members: Dr. Kaushik Ghosh and Dr. Dipankar Mandal, for their time, suggestions, insightful comments, and encouragement.

I am also grateful to my experimental collaborators, Dr. Kamalakannan Kailasam, Dr. Sangita Roy and Dr. Monika Singh. My work with their group has greatly widened my perspective and approach to my research.

I express my sincere thanks to the founder director of INST, Prof. A.K. Ganguly, and the present director Prof. Amitava Patra, for allowing me to work in the prestigious Laboratory and making all the facilities available for my research work. I would like to acknowledge the Department of science and technology (DST) for the financial assistance in the form of an Inspire research fellowship.

I am highly grateful to Dr. R. Lenin, a former postdoc student of our group, who helped a lot in my starting days of Ph.D. and performing experiments. His positive attitude and immense knowledge inspired me to carry out my research work without giving up. Whenever I go to him with a problem, I always come back with a solution. His positive attitude and

immense knowledge always inspired me a lot. The valuable suggestions given by him helped me to shape the thesis more perfectly.

I thank all my seniors, Dr. Prabhjot Kaur, Dr. Neha Wadhera, Dr. Ruchi, Dr. Nand Kumar, and Dr. Renu Rani, for their help and support in the initial stages of my work. I would also like to thank my beloved group members: Sonali Kakkar, Parry Sachdeva, Raveena Gupta, Gaurav Rana, Naveen Kumar, Baljinder Kaur, Ajay, and Ayushi. It was a pleasure to be involved with them freely in many scientific discussions.

I extend my thanks and appreciation to my close friends: Saveena Goyal and Manish Kumar Mohanta, for being a source of great joy and for many of their unmentioned support during my years at INST. Special thanks to my friends who made my life more cheerful during my stay at INST. Vibhav Katoch, Anamika Kumari, Anshu Gupta, Bibek Ranjan Sathyapathi, Manish Dumen, Mayank, Mansi Pahuja, Harsha, Mamta Raturi, Gagandeep Kaur, Ridhima, Chirag Miglani, Rakesh Mishra, Hari Krishna Mishra, Nandan Ghorai, Jijo Thomas, Sourav Sen, Deepika Rani.

I want to thank my university friends: Vishal bhateja, Vaibhav Arora, Vishal Thakur, Ajay Devangan, Arun Bhalla, Davinder, Murli Manglam, Mani Manchanda, Vinay Kumar, Prabhleen Kaur, Juno, Vandana Verma, Nisha Mittal and Depika Rani for always being there for me and refreshing me up by small outing.

Finally, I would like to thank my lovely parents, Shri. Ram Sewak Pal & Smt. Sushila Devi, and my beloved younger brother Surjit Singh for being a constant source of inspiration, motivation, and courage. A debt of gratitude for their continuous unwavering love and encouragement over the years. This accomplishment would not have been possible without them.

Ajit Singh

Abstract

A basic understanding of electron and phonon transport mechanisms in nanomaterials can open doors for many applications. Many intrinsic and extrinsic factors contribute to these transport mechanisms in nanomaterials. Surface and interface are one of the important factors and play a very critical role in electron and phonon transport in nanomaterials. In this thesis, electrical, thermal, and photo-conductivity are investigated and special attention is given to the surface or interface effect to optimize the performance of many potential devices.

Thermal conductivity plays a significant role in many areas such as thermoelectrics, nano and microelectronics, insulation, efficient thermal management becomes crucial. The steady increase of interest in nanomaterials in thermal physics and for thermoelectrics has motivated the development of accurate thermal conductivity measurement techniques. Many static or dynamic methods have been developed to measure the thermal conductivity of new materials such as 3ω, transient hot wire, thermoreflectance, or steady-state methods. Among the different approaches mentioned above for determining thermal conductivity, the Transient Hot-Wire (THW) method possesses some unique advantages. It is capable of accurately measuring the thermal conductivity of solids, liquids, and gases. THW measurement method can be carried out much faster by reducing equilibrium time to a few seconds. THW setup is designed to measure the thermal conductivity of nanofluids at room temperature.

The role of nanofluids in thermal management, exchange, and insulations is gaining tremendous attention in biological and clinical applications. Surfactants on the nanoparticle surface play an important role in the dispersion and stability of the nanoparticles in the fluid. Hence to deepen the understanding of the role of surfactants associated with nanoparticles in different fluid mediums, it is essential to study their cumulative properties. In this work, monodispersed nanoparticles (Fe_3O_4) were synthesized and stabilized with different surfactants (citric acid/oleic acid) and dispersed in different mediums (water/toluene) at different concentrations. The thermal conductivity of iron oxide nanofluids has been studied theoretically as well as experimentally using a self-made Transient hot wire (THW) measurement setup. The thermal conductivity of water is found to be reduced by 67% by adding nanoparticles coated with citric acid whereas 4% enhancement occurs for toluene when oleic acid-coated nanoparticles are added. In this work, increasing/decreasing of thermal conductivity has been related to surface properties of nanoparticles and polarity of the base fluid which has been supported by theoretical work. The same measurement techniques were

further used for the thermal conductivity measurement of Cellulose nanofibers (CNF**)** aerogel and iron oxide@CNF nanohybrid materials for thermal insulation applications. The nanohybrid demonstrated very low thermal conductivity as low as 0.024 W/mK at 2 wt% of iron oxide@CNF, indicating the better insulating potential of these nanohybrids as compared to other conventional insulating materials.

The tunable electrical conductivity in the conducting polymer is one of the significant advantages of focusing on these materials for flexible electronics and electrical applications. In this work, the polyaniline electrical conductivity is tuned by doping with different dopant materials, varying doping concentrations, and different morphologies. The experimental measurement was done on the pellets using the van der Pauw method. The experimental electrical conductivity results are correlated with the optical band gaps and their corresponding electronic transitions. Increasing the doping concentration from 0 to 1.0 M HCl increases electrical conductivity five-fold from 1.98 to 10.2 S/cm. The measured electrical conductivity is larger for the polyaniline nano-whisker and nanofiber (~2 S/cm) samples than for the sample with highly entangled polymer chains (0.26 S/cm). Moreover, it was found that the polyaniline nanofibers with ordered polymer chains show larger electrical conductivity (1.75 and 1.27 S/cm) as compared with the disordered polymer chains (0.22 S/cm).

The phenomenon of 'persistent photoconductivity (PPC)' has gained tremendous attention because of its prospective applications in the field of optoelectronics. PPC was well studied in semiconductor materials. Another important class of materials showing potential persistent photocurrent is "oxides". Among oxides, STO can be considered an important member of the perovskite oxide family which exhibits many novel phenomena and is a prime candidate for device applications. This work studied the effect of the light illumination for an insulating (3 unit cell of LaVO3(LVO) on SrTiO3(STO)) and a conducting (5u.c. of LVO on STO) oxide interface using different wavelengths of light 405 nm and 532. For the insulating interface, under light illuminations transient photoconductivity (TPC) has been observed from 76K to 300K. The conducting interface shows small PPC under only 405nm illumination but zero PPC under 532nm illumination.

In the other work, the effect of light illumination on the transport properties was studied on 2-D electron gas at the conducting interface of EuO and $KTaO_3$ using different wavelengths (405 nm, 532 nm, 705 nm) of light. This conducting interface showed wavelength, power, and carrier density-dependent PPC at 76K and 300K.

Contents

List of Figures

List of Tables

List of Abbreviations

EMT	Effective Medium Theory
MCNTs / MWCNTs	Multiwalled Carbon Nano Tubes
CNT	Carbon Nano Tubes
THW	Transient Hot Wire
LF	Laser Flash
LFA	Laser Flash Apparatus
TPS	Transient Plane Source
DI	Deionization
TC	Thermal Comparator
XRD	X-Ray Diffraction
XPS	X-Ray Photoelectron Spectroscopy
UPS	Ultraviolet Photoelectron Spectroscopy
TEM	Transmission Electron Microscopy
TGA	Thermogravimetric Analysis
RTD	Resistance Thermometer Detector
JCPDS	Joint Committee on Powder Diffraction
PANI	Polyaniline
DSC	Differential Scanning Calorimetry
SMU	Source-Measurement Unit
TID	Thermal Impedance Displacer
CNF	Cellulose Nanofibres
FWHM	Full Width Half Maximum
DLS	Dynamic Light Scattering
HOMO	Highest Occupied Molecular Orbital
LUMO	Lowest Unoccupied Molecular Orbital
CSA	Camphor Sulfonic Acid
PNF-CA	Citric Acid doped Polyaniline Nanofibres

PNF-CSA	Camphor Sulfonic Acid (CSA)
PANI-NW	Polyaniline Nanowhiskers
EB	Emeraldine Base
SEE	Secondary Electron Edge
PC	Photoconductivity
SSPC	Steady State Photoconductivity
TPC	Transient Photoconductivity
PPC	Persistent Photoconductivity
2DEG	2-Dimensional Electron Gas
NPC	Negative Photoconductivity

List of Symbols

ρ_n	Density of Nanofluid
ρ_p	Density of Particles
ρ_f	Density of base fluid
ϕ	Volume fraction of Nanoparticles
k_e	Effective thermal conductivity of nanofluids
k_{nf}	Thermal conductivity of nanofluids
k_f	Thermal conductivity of base fluid
k	Thermal conductivity
ρ_R	Resistivity
σ	Electrical conductivity
μ_n	Electron mobility
μ_p	Hole mobility
E_g	Band gap
q	Heat flux per unit length per unit time
β	Temperature coefficient of resistance
α_D	Thermal diffusivity
β_F	Full width at half maximum
G	Surface Conductance
C_p	Heat Capacity
λ_p	Mean free path of phonon
S	Seebeck coefficient
Φ	Work function
R_s	Sheet resistance
R_D	Dark Resistance
α	Optical absorption coefficient

Chapter 1

Introduction

1.1 Nanofluids and their importance

The colloidal suspension of the nanoparticles having size ranges 1 to 100 nm in a base fluid is known as nanofluids. Nanofluids' exceptional high thermal conductivity makes them a promising candidate for heat conduction enhancement in various applications. In the present scenario, there is a significant inconsistency in the thermal conductivity results of different nanofluids. The enhancement mechanisms of thermal conductivity in nanofluids are still controversial. Investigation about the constrained convection of nanofluids is significant for the possible utilization of nanofluids in heat move gadgets. Ongoing examinations demonstrated that the heat conduction of nanofluids surpasses the thermal conductivity improvement of nanofluids.[1] This additional improvement may be clarified by thermal dispersion, which happens because of the arbitrary movement of nanoparticles in the flow.

Heat conduction or heat transfer is essential in many fields such as electronics, air conditioning, transportation, power generation, etc. High-performance cooling is one of the crucial requirements of the industry so that the waste heat can be expelled out of the system and increase performance. Therefore, various researchers are currently working on the heat conduction capability of the testing fluids. The high heat conduction performance of the nanofluids has drawn the attention of investigators to use it for heat transfer applications. The thermal conductivity of the nanofluids is the prime parameter of the heat transfer performance. Currently, conventional fluids like water, ethylene glycol, and engine oil are used for cooling applications because of the much lower thermal conductivity when compared the metals like iron and copper and non-metallic materials like CuO and carbon nanotubes. This fact is the starting point of the idea which creating the solid and liquid mixture to obtain higher thermal conductivity and improve the heat transferability of the fluids.[2], [3] Maxwell was the one

who started mixing the solid (a millimeter or micrometer) sized particle in the fluid. The large size of the solid particles causes several technical problems like faster settling time of the suspension, abrasion of the surface, Clogging micro-channels of devices, and increasing pressure drop.[4], [5] For the First time, Choi et al.[6] coined the term nanofluids for the fluids with a suspended nanoparticles concentration of less than 5 volume percentage. Nanoparticles have several advantages over microparticles. Nanofluids are more stable, have a much higher surface area, a surface area to volume ratio of Nanofluids are more durable, have a much higher surface area, a surface area to volume ratio of approximately 1000 and higher thermal conductivity, lower erosion, and clogging significant energy saving. Several researchers reported on the higher heat transfer performance of nanofluids. Eastman et al.[6] investigated the higher thermal conductivity of the nanofluid as one of the best features of the nanofluids. They observed a 40% enhancement in the thermal conductivity after the adding 3 vol% of copper nanoparticles in the ethylene glycol. Different researchers investigated the convective heat transfer properties of nanofluids. From this point of view, a large number of reports with discrepancies have been reported. This has been claimed that better heat transport properties of the nanofluids would have numerous advantages like improvement in the efficiency of heat transport, reducing the size of the system, providing much greater safety margins, and reducing costs. The synthesis and preparation of the nanofluids are also important for their better performance and applications. Better synthesis and preparation of the nanofluids further improves the thermal transport capabilities of the nanofluids. At present, researchers put their efforts mostly improving the thermal conductivity of the nanofluids while other thermophysical properties like specific heat and density of nanofluids almost got neglected.

1.2 Properties of nanofluid

1.2.1 Density

The density of the nanofluids directly affects the specific heat of the nanofluids. The temperature of the nanofluids and nanoparticle concentration change the density of the nanofluid. The density of two-phase mixtures for micrometer-size particles is given by Cheremisinoff [7]. This equation is further used by Pak and Cho [8] for the nanoparticles. The density equation is represented as

$$\rho_n = \phi\rho_p + (1-\phi)\rho_f \quad (1.1)$$

Where, ρ_n, ρ_p, and ρ_f is the density of the nanofluid, particle, and base fluid, respectively. ρ_f is the volume fraction of the nanoparticles in the base fluid. Pak and Cho [8] experimented and apply the equation for the density measurement. They proved that the above-mentioned equation is valid for the determination of the density of the nanofluid. The density measurement of various nanofluids at different temperatures has not been presented much in the literature yet.

1.2.2 Specific heat

The specific heat of the nanofluids is defined as the amount of heat required to raise the temperature of one gram of nanofluids by one degree centigrade. The specific heat of the nanofluids is an important thermo-physical property that plays a key role in the improvement of the heat conduction properties of nanofluids. Specific heat acts as a function of the temperature which further affects the heat transfer of the fluids at different temperatures. When the exact concentration of the nanoparticles in the base fluid is known, then the specific heat of nanofluids can be determined by the equation given below [8]

$$c_{p,n} = \phi c_{p,p} + (1-\phi)c_{p,n} \quad (1.2)$$

There are other expressions for determining the specific heat of nanofluids given by Xuan and Roetzel [9]. The equation is

$$(\rho c_p)_n = \phi(\rho c_p)_p + (1-\phi)(\rho c_p)_f \quad (1.3)$$

The specific heat of nanofluids is mass-specific quantity as it depends on the density of the nanoparticles in the nanofluids. So the equation given by Xuan and Roetzel [9] is theoretically more consistent as compared to the Eq. 1.2.

1.2.3 Viscosity

Nanofluid viscosity depicts the internal resistance of fluid during its flow. The viscosity influences the convective heat transfer coefficient. Therefore the importance of viscosity is the same as the thermal conductivity in various engineering systems [1] and thermal applications [11] involving the fluids flow. Viscosity directly influences the pressure drop in constrained convection during the laminar flow of the fluids. Nanofluid viscosity depends on different parameters like particle volume fraction, particle size, temperature, and extent of clustering. There is an increase in viscosity of the nanofluids with an increase in the concentration of the nanoparticles in base fluids and this was observed by numerous investigations.[12], [11], [13] The research on the viscosity of the nanofluids or fluids is limited compared to the research on the thermal conductivity of nanofluids. There is still no standard method to estimate the viscosity of the nanofluids.

1.2.4 Thermal conductivity

In the current scenario, a notable amount of experimental and theoretical research was made to investigate the thermophysical properties of nanofluids. Among all the thermophysical properties, thermal conductivity is the major parameter that affects heat transfer capability of the fluid. At present, water, ethylene glycol, and oils are commonly used for heat transfer applications. These fluids have low thermal conductivity, so researchers tried to increase the thermal conductivity by adding some solid micro size particles because of their much higher thermal conductivity. Researchers found the enhancement in the thermal conductivity results but it serves difficulties in the stability and significant pressure drop of the resultant fluid because of the large size of the solid particles. Further, advancement in nanotechnology helps researchers make and use nano-sized (<100nm)particles instead of microsized.[6] This suspension results in not only enhancement in the thermal conductivity but also in the stability of the suspension. The small size of particles prevents clogging and can be used in microchannels.[14], [15] Furthermore, all the experimental results for the different types of nanoparticles show a significant enhancement in the thermal conductivity of the base fluids suspensions as compared to the large size (millimeter or micrometer) particle suspension. Researchers proposed many theoretical models to explain this anomalous enhancement in the

thermal conductivity of the base fluid after the addition of the nanoparticle. But till now, there is no standard theoretical model which can predict the thermal conductivity of the nanofluids. All the experimental and theoretical studies show that the thermal conductivity of nanofluids depends on various factors such as particle volume fraction, particle material, particle size, particle shape, base fluid material, and temperature.

1.3 Different parameters affecting the thermal conductivity of nanofluids

1.3.1 Volume fraction of nanoparticles

The volume fraction of the nanoparticles is the volumetric concentration of the solid nanoparticles in the whole volume of the nanofluid. The volume fraction of the nanoparticles is the most common parameter which is measured in most of the experiments related to the thermal conductivity measurement of nanofluids. In the reports, the volume fraction of nanoparticles is stated in two forms, volume or weight percentage. As the thermal conductivity of the solid is much higher than the base fluids (as water 0.6 W/mK and Cu = 400W/mK) so the resultant mixture of the particles in the fluid shows an increase in the thermal conductivity as predicted by Maxwell's Effective Medium Theory (EMT). Most of the researchers found the enhancement in the thermal conductivity of the nanofluids with increasing the volume fraction of the nanoparticles and the relation between thermal conductivity and the particle volume fraction is almost linear. Masuda et al.[16] did the first experiment regarding the thermal conductivity measurement of the nanofluids. In this study, they used water as base fluids. They prepared water-based Al_2O_3, SiO_2, and TiO_2 nanofluids using a two-step method. The size of the nanoparticles is 13 nm, 12 nm, and 27 nm respectively. They found the maximum enhancement at 4.3 vol% in water-based Al_2O_3 nanofluids which is 32.4%. They also found the linear relationship between thermal conductivity and volume fraction.

There is another report by Lee et al. [17] on water and ethylene glycol-based Al_2O_3 and CuO nanofluids. The sizes of Al_2O_3 and CuO nanoparticles were 38.5 nm and 23.6 nm respectively. They found a similar trend between thermal conductivity and particle volume fraction as

observed by Masuda et al. [16] . The largest increment was 20% at 4 volume percentage of ethylene glycol-based CuO nanofluids as shown in Figure 1.1. On the other hand, Choi et al.[18] and Eastman et al.[19] performed experiments on oil-based Multiwalled Carbon Nano Tubes (MCNTs) and they observed a non-linear relationship between thermal conductivity and volume fraction. Hong et al.[20] also found a non-linear relationship between these two properties in their measurement of ethylene glycol-based Fe nanofluids. Yu et al.[21] also showed similar results for the ethylene glycol-based ZnO nanofluids. At present, the linear and non-linear relationship between these two properties of nanofluids has been proved by different theoretical and experimental studies. So the increases in volume concentration of the nanofluids surely increase the thermal conductivity. Duangthongsuk and Wongwises [22] have investigated the variation in the thermal conductivity in water-based TiO_2 nanofluids by changing the volume fraction of nanoparticles from 0.2-2% at room temperature. All these experimental results of thermal conductivity versus volume fraction were followed by different theoretical models like Effective Medium Theory [23], Hamilton-Crosser Model [24], Bruggeman model [25], Yu and Choi model [26].

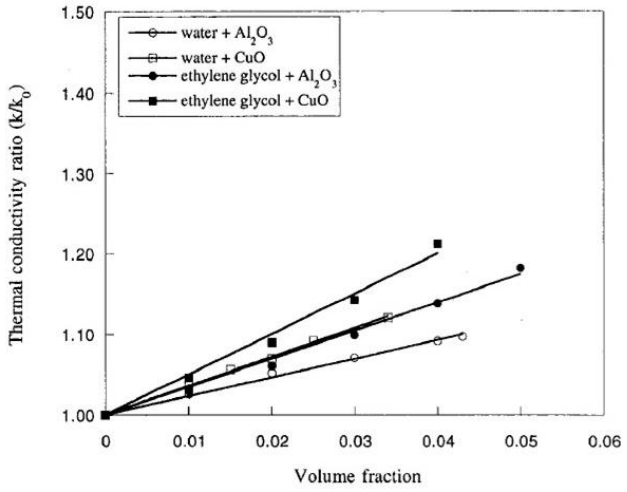

Figure 1.1: Effective thermal conductivity of nanofluid as a function of volume fraction of oxide nanoparticles [14]

1.3.2 Type of Base fluids and nanoparticle material

The Maxwell model [27] shows that the effective thermal conductivity of the nanofluids should be increased with the decrease in the thermal conductivity of the base fluids. The equation is given below as

$$k_e = k_{nf}/k_f \tag{1.4}$$

Where k_e is the effective thermal conductivity of the nanofluid, k_{nf} is the thermal conductivity of the nanofluids and k_f is the thermal conductivity of the base fluid. So according to this model, the base fluid with less thermal conductivity favors the effective thermal conductivity of nanofluids. But the real picture of nanofluids is much more complex as the viscosity of the fluids depends on the type of the base fluid which affects the Brownian motion of the nanoparticle that in succession affects the thermal conductivity [28]. Researchers did various experiments to understand the effect of the base fluid on the thermal conductivity of the nanofluids.

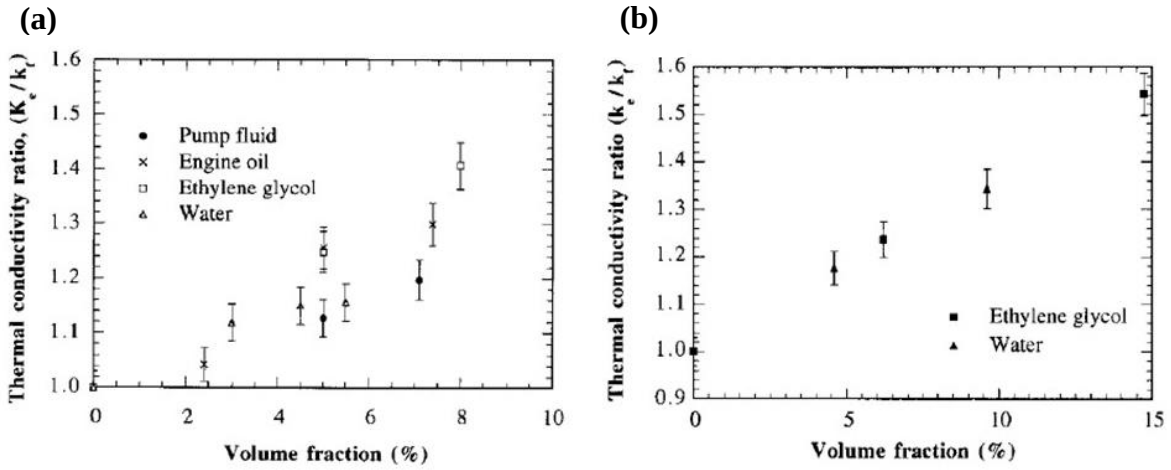

Figure 1.2: (a) Effective thermal conductivity enhancement of different base fluids (pump fluid, engine oil, ethylene glycol and water) as a function of Al_2O_3 nanoparticle's volume fraction (b) Effective thermal conductivity enhancement of ethylene glycol and water as a function of CuO nanoparticle's volume fraction [26].

Wang et al. [29] prepared different types of nanofluids using various base fluids like water, ethylene glycol, engine oil, vacuum pump fluids with Al_2O_3, and CuO nanoparticles. Al_2O_3/Ethylene glycol showed the highest effective thermal conductivity whereas Al_2O_3/Engine oil showed somewhat less effective thermal conductivity. Water and vacuum pump oil-based Al_2O_3 nanofluids showed the least effective thermal conductivity. The effective thermal conductivity of water and ethylene glycol-based CuO nanofluid interestingly exactly matched with previous nanofluids at the same volume fraction of nanoparticles. There was one report by Lee et al. on the nanoparticles forming an electric double layer around their surface affects the thermal conductivity of the nanofluids.[30] This formation of the electric double layer and its thickness depends on the base fluids. Xie et al.[31] also analyzed the effect of the

base fluids on the effective thermal conductivity of the nanofluids. For this, they used deionized water, glycerol, ethylene glycol, and pump oil as base fluids for Al_2O_3 nanofluids preparation. They also made ethylene glycol-water and glycerol-water-based nanofluids with various volume fractions of nanoparticles and examined the effective thermal conductivity of nanofluids. These experiment results qualitatively matched with the maxwell model. But the theoretical analysis made by Hasselman and Johnson [32] found independent thermal conductivity of the base fluids which further contradicts the experimental results. Liu et al.[33] used ethylene glycol and synthetic engine oil as base fluids in their experiment. They achieved higher effective thermal conductivity for MWCNT/Synthetic oil nanofluids as compared to the MWCNT/ethylene glycol.

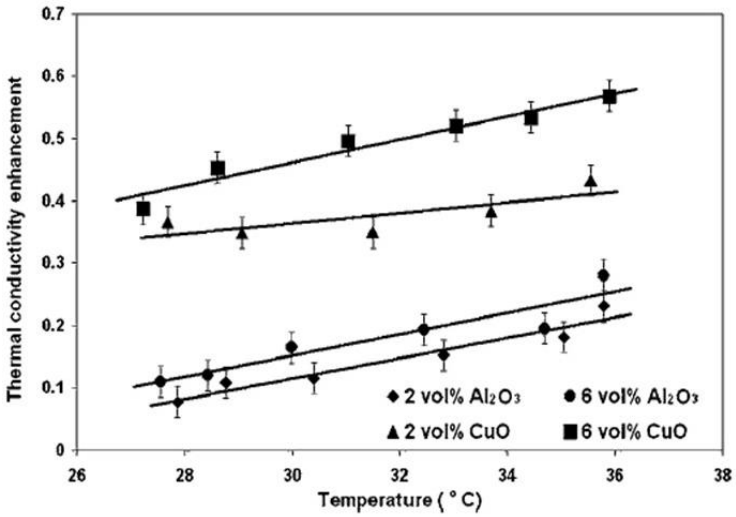

Figure 1.3: The effect of the temperature on the thermal conductivity enhancement of Al_2O_3/water and CuO/water nanofluids at two fixed volume fraction (2 vol% & 6 vol%) of nanoparticles.[31]

Like base fluids, the nanoparticle material also plays an important role in the thermal conductivity of the nanofluids. If the different material nanoparticles possess the same base fluids then their difference in thermal conductivity would greatly influence the effective thermal conductivity of the nanofluids. Higher thermal conductivity of the nanoparticle materials is expected to have a higher thermal conductivity of the nanofluids. Li and Peterson[34] experimented to check this fact. They made Al_2O_3 and CuO suspended water-based nanofluids. They revealed that CuO/water shows higher effective thermal conductivity as compared to the Al_2O_3/water nanofluid at the same volume fraction of particles as shown in Figure 1.3 and this follows the fact as the CuO solid particles show higher thermal conductivity

than Al_2O_3 Sold particles. Chopker et al.[35] suspended Al_2Cu and Ag_2Al in the water and the ethylene glycol. The thermal conductivity results revealed that the Ag_2Al nanoparticles enhanced the thermal conductivity to a greater extent as compared to Al_2Cu because the thermal conductivity of the Ag_2Al solid particles is higher than the Al_2Cu nanoparticles.

1.3.3 Morphology of nanoparticles

The morphology name in material science indicates the study of the shape and size of the objects. A large number of reports have been published on the size of the nanoparticles which indicated the size of the nanoparticles given a great contribution to the enhancement of the thermal conductivity of the nanofluids. The size of the nanoparticle becomes an important parameter of the thermal conductivity of the nanofluids. Regarding the study of the nanoparticles size effect, Chon et al.[36] made the suspension of Al_2O_3 nanoparticles ranging in size from 11nm to 150 nm in the deionized water. Their study revealed the effect of the size of nanoparticles on the thermal conductivity of the nanofluids.

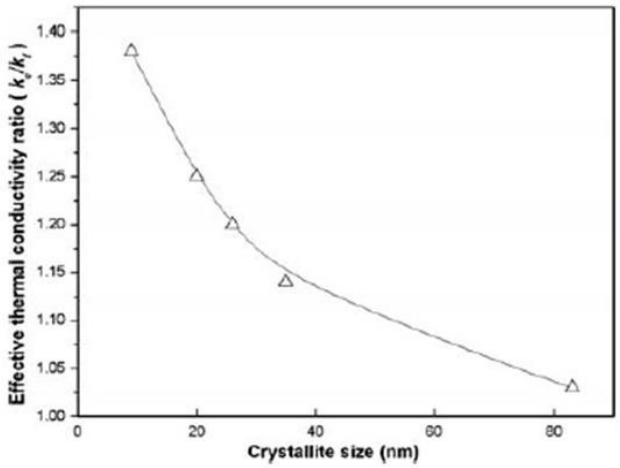

Figure 1.4: Effective thermal conductivity as a function of crystallite size of nanoparticles in ethylene glycol based $Al_{70}Cu_{30}$, 0.5 vol% nanofluid [34]

To study the size effect of the nanoparticle on the thermal conductivity. Chopker et al.[37] prepared nanofluids by dispersing nanocrystalline $Al_{70}Cu_{30}$ particles in ethylene glycol. They found an enhancement in the thermal conductivity of the nanofluid with a reduction in the size of the nano crystallite size as shown in Figure 1.4. Beck et al.[38] systematically studied the size effect on the thermal conductivity of Al nanoparticles. Nanoparticles of 30 to 120 nm sizes

were used in the study. They observed that thermal conductivity enhancement increases with decreasing particle size. Minsta et al.[39] also study the size effect of the nanoparticle by preparing two different sizes of Al_2O_3 nanoparticles (36 nm and 47 nm) and dispersing them into water. Their study revealed that particles of small size enhance the thermal conductivity of the nanofluids to a greater extent.

The shape of the nanoparticles also plays a vital role in the thermal conductivity of the nanofluids. In the nanofluid, researchers mainly focused on the two types of shapes spherical and cylindrical. Xie et al.[31] were the first researchers to report the effect of the shape of the nanoparticles on the thermal conductivity of the nanofluid. They prepared SiC-26 (spherical) and SiC-600 (cylindrical) nanoparticles and synthesized water and ethylene glycol-based nanofluid using a two-step method. They revealed that the morphology (size and shape) of the solid particles affects predominantly the enhancement ratio of thermal conductivity (see Figure 1.5).

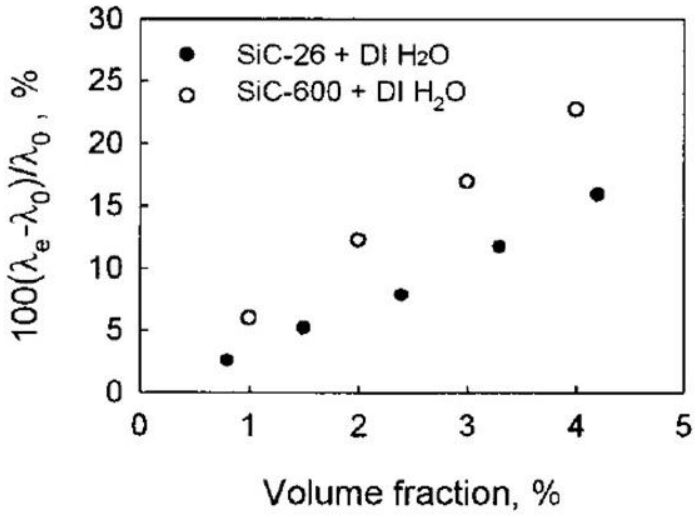

Figure 1.5: The effect of the nanoparticle's shape on the thermal conductivity of SiC-26 (spherical)/water and SiC-600 (cylindrical)/water nanoparticle suspension [28].

Furthermore, Murshed et al.[40] prepared spherical (15 nm) and rod-shaped (10 nm-40nm) TiO_2 nanoparticles to study the shape effect of nanoparticles on the effective thermal conductivity. They investigated the higher thermal conductivity of rod-shaped nanoparticles. In addition to these experiments, carbon nanotubes nanofluids generally show higher effective thermal conductivity relative to spherical nanoparticles. This indicated that the enhancement in the thermal conductivity will be more in cylindrically shaped nanoparticles than spherical

nanoparticles. But the viscosity of the nanofluids with cylindrical nanoparticles more which further increases the pumping power and reduces the feasibility of nanofluids with cylindrical nanoparticles.[41] Another report on the shape effect by Liu et al.[42] in which they prepared water-based Cu nanofluids with sizes from 50nm to 250 nm having a needle and square-shaped. They studied the morphological effect on the thermal conductivity behavior of nanofluids.

1.3.4 Temperature and Clustering

The thermal conductivity of the fluid and nanoparticle changes with the temperature so nanofluid effective thermal conductivity is highly dependent on the temperature of the

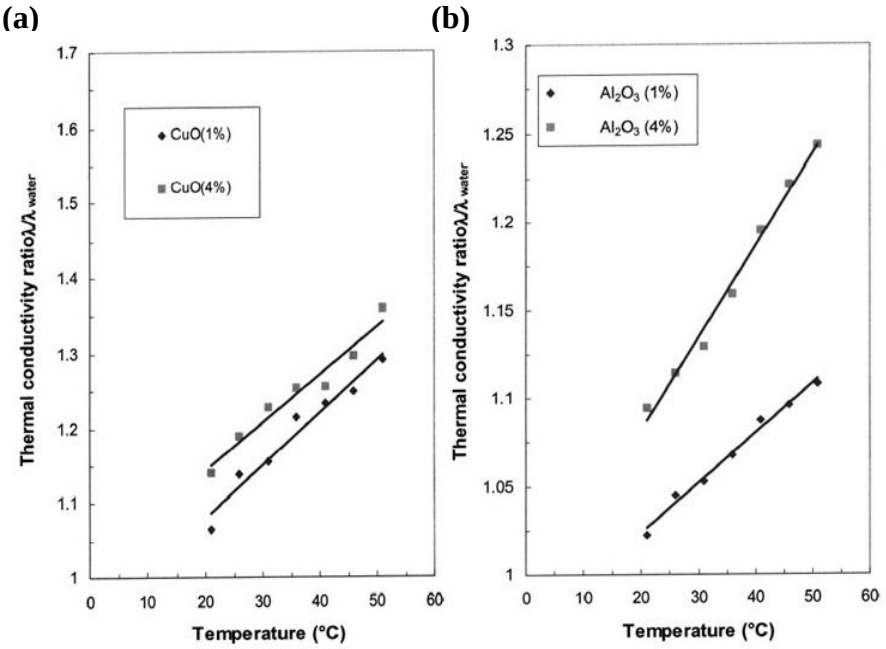

Figure 1.6: The effect of the temperature on the effective thermal conductivity of (a) CuO/water nanoparticle suspension. (b) Al_2O_3/water nanofluids [40]

nanofluids. There are other phenomena like the Brownian motion of the nanoparticles and clustering effects due to changes in the temperature which further affect the thermal conductivity of the nanofluids.[43] Masuda et al.[16] investigated the thermal conductivity of the water-based Al_2O_3, SiO_2, and TiO_2 nanofluid and found a deterioration in the effective thermal conductivity with an increase in temperature. On the other hand, Das et al.[44] performed their experiment on the water-based Al_2O_3 and CuO nanofluids in the temperature range of 20 to 50 ^oC. They found a 2 to 4-fold enhancement in the effective thermal conductivity of the nanofluids. In the case of 1% and 4%, a linear relationship between

temperature and thermal conductivity has been observed. volume fraction and these results make nanofluids more attractive to work as a cooling fluid at a higher temperature than room temperature. But these results contradict the Masua et al.[16] results. There is another report on the temperature-dependent thermal conductivity study of the water-based Al_2O_3 (36 nm) and CuO (29 nm) nanofluids by Li et al.[34]. They found an enhancement in the effective thermal conductivity of both nanofluids with temperature while other parameters were kept constant. With increasing temperature, Al_2O_3/Water nanofluid's thermal conductivity showed more conspicuous on the volume fraction of the nanoparticles. Turget et al.[45] also investigated temperature-dependent thermal conductivity of the ionized water-based TiO_2 nanofluids. They prepared nanofluids by two-step methods and use the 3-omega method for thermal conductivity measurement at different temperatures (13-55 ^{0}C). They found a minor enhancement in thermal conductivity with an increase in temperature which contradicts previous studies on nanofluids. Furthermore, Ding et al.[46] experimented with temperature-dependent thermal conductivity of the Multiwalled Carbon Nanotubes (MWCNTs) suspended nanofluids. They prepared nanofluids by suspending sonicated CNT samples into distilled water containing Gum Arabic (0.25 wt%) as dispersant and investigate effective thermal conductivity using the THW method at 20,25 and 30 ^{0}C and shows that at 20 and 25 ^{0}C the effective thermal conductivity becomes independent of the concentration above 0.5 wt% as compared to at 30 ^{o}C.

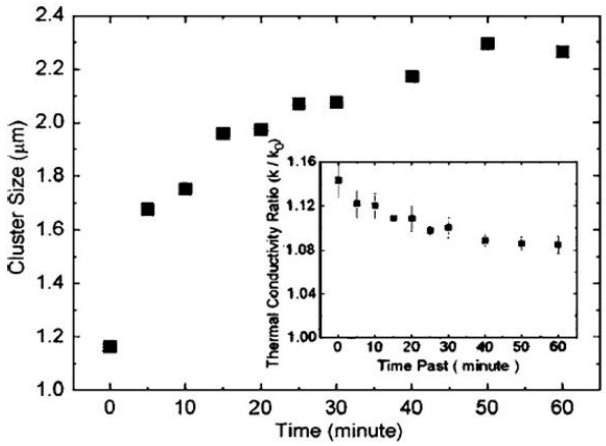

Figure 1.7: (a) The nonlinear variation of average nanocluster size as function of time after switched off the sonication process. The agglomeration of nanoparticles starts immediately after the sonication stopped. The inset shows the variation of effective thermal conductivity as a function of time of 0.2 vol% nanofluids after the sonication process stopped [46]

Nanoparticles in the nanofluids usually form clusters which further affects the thermal conductivity of the nanofluids. In literature, clustering of the nanoparticles considers a major parameter of the thermal conductivity in nanofluids. Keblenski et al.[47] considered nanoparticle clustering as one of the four effective parameters on the thermal conductivity of the nanofluids. Zhu et al.[48] investigated the thermal conductivity of Fe_3O_4 Water nanofluids and found higher effective thermal conductivity compared to Al_2O_3 and TiO_2 although bulk Fe_3O_4 has lower thermal conductivity. This anomalous thermal conductivity was observed because of the clustering of the Fe_3O_4 nanoparticles in the nanofluids.

Further, Hong et al.[49] investigate the effect of the clustering of Fe(10 nm) nanoparticles on the thermal conductivity of nanofluids. They used ultrasonication for breaking the nanoclusters into smaller clusters and observed that the clustering of nanoparticles is closely related to the thermal conductivity of the nanofluids. They found non-linear variation in effective thermal conductivity as the concentration of the nanoparticles increased. Clustering of the nanoparticles increases rapidly with the concentration which deviates the enhancement from linearity as shown in Figure 1.7. Evans et al.[50] also analyzed the role of the aggregation of the nanoparticle on thermal conductivity and found significant enhancement by the aggregation of nanoparticles to clusters. From the results of various investigators, it was concluded that nanoparticle cluster size affects thermal conductivity significantly.

1.4 Contraries in thermal conductivity of Nanofluids

There are significant contradictions in the experimental thermal conductivity results of the nanofluids. This discrepancy is mainly due to ignorance of some specific parameters in most of the reports which significantly affects the thermal conductivity of nanofluids. These parameters are mainly the nanoparticle clusters, type and amount of surfactant, intensity, and duration of the ultrasonication, measurement method, and pH of nanofluids.

The clustering of nanoparticles in the nanofluids is one of the main reasons for the contradictory experimental results. The clustering of the nanoparticles depends on several parameters like surfactants and pH vales of the nanofluids. Adding suitable surfactant and adjusting the pH value of the nanofluids provide a better dispersion of nanoparticles in the fluids.[51] This is found that the difference in pH and surfactant leads to different thermal conductivity results

despite all the other parameters of nanofluid being the same.[2] Researchers commonly used ultrasonic vibrations to break the clusters and obtain good dispersion of nanoparticles in the fluid. In this case, the intensity and duration are two factors that affect the dispersion characteristics. The cluster size starts to increase with time [49] just after the turn of the ultrasonication process. Therefore, the intensity and duration of vibration as well as the time between application of vibration and measurement of k also affect the thermal conductivity values which further creates contradictory results in the literature.[2]

The different measurement techniques become an important issue regarding the discrepancy in the experiment results of different nanofluids. Ya Hua et al.[52] gives the comparison of the transient hot wire method and steady-state cut-bar method results at room temperature and conclude that results from both measurement techniques are approximately the same. Although, other authors reported significant inconsistency in the results at the higher temperature. Authors claimed that this discrepancy is due to the natural convection effect that arises in the transient hot wire method at a high temperature which deviates the results at higher values. Another report by Ju et al.[53] also suggested that the transient hot wire method gives inaccurate results if the measurement is executed just after the sonication. Sonication increases the temperature of the fluid so temperature affected the results at room temperature. In their report, this effect of temperature lasted for 50 min. They also mentioned in their report that the interval between heating pulse should be more that 5 s to eliminate errors in result. Ya Hua et al.[52] and literature results matched might be due to the abovementioned factors discussed by Ju et al.[53]

Many thermal conductivity experiments observed the anomalous enhancement in k of nanofluids. This anomalous enhancement of thermal conductivity becomes a matter of intense discussion within the scientific community. Many investigators[17]–[19], [37] reported the k enhancement with volume fraction of nanoparticles follows a nonlinear relationship. However, Buongiorno et al.[54] and Antoniadis et al.[55] pointed out the anomalous enhancement of k in nanofluids and claimed that the enhancement of k was due to unappropriated practice followed during the experiments.

1.5 Technique for effective thermal conductivity measurement of Nanofluid

Thermal conductivity measurement of the nano fluid is quite a challenging task. Not only the convection effect in the fluids but also the indefinite shape, size, and cross-section area make it more difficult to measure thermal conductivity efficiently. In the case of nanofluids, the suspension of nanoparticles should be homogenous otherwise it causes a major problem for the thermal conductivity measurement. This convection problem in the fluids can be suppressed by reducing the thermal conductivity measurement time. Several measurement techniques have been developed over the past few years to measure the effective thermal conductivity of different types of fluids efficiently. These measurement techniques can be divided into two categories (1) Steady-state techniques and (2) Transient techniques. We have discussed the important features, basic principles, advantages, and limitations of these different measurement techniques in this section.

1.5.1 Transient techniques

1.5.1.1 Transient hot wire (THW) method

In 1931, Stalhane and Pyk [56] suggested the Transient Hot Wire method for the thermal conductivity measurement of powder materials for the first time. After that, many researchers modified this method to make it accurate as well as suitable for different types of fluids. This method has been extensively used by researchers as shown in the Figure 1.8(a) [50] because of its several advantages over the other methods. This technique is not only fast as compared to the other methods but also the short time of measurement of this method for fluids eliminates the errors due to the natural convection. The design of other techniques is quite complex as compared to the hot-wire apparatus and this can be easily constructed in the lab. THW method can achieve uncertainty in the measurement below 2% for the nanofluids.[58] The schematic design of the hot-wire method shown in Figure 1.8(b) was manufactured by Lee et al.[59] for the effective thermal conductivity measurement of Al_2O_3/H_2O nanofluids. In the Wheatstone

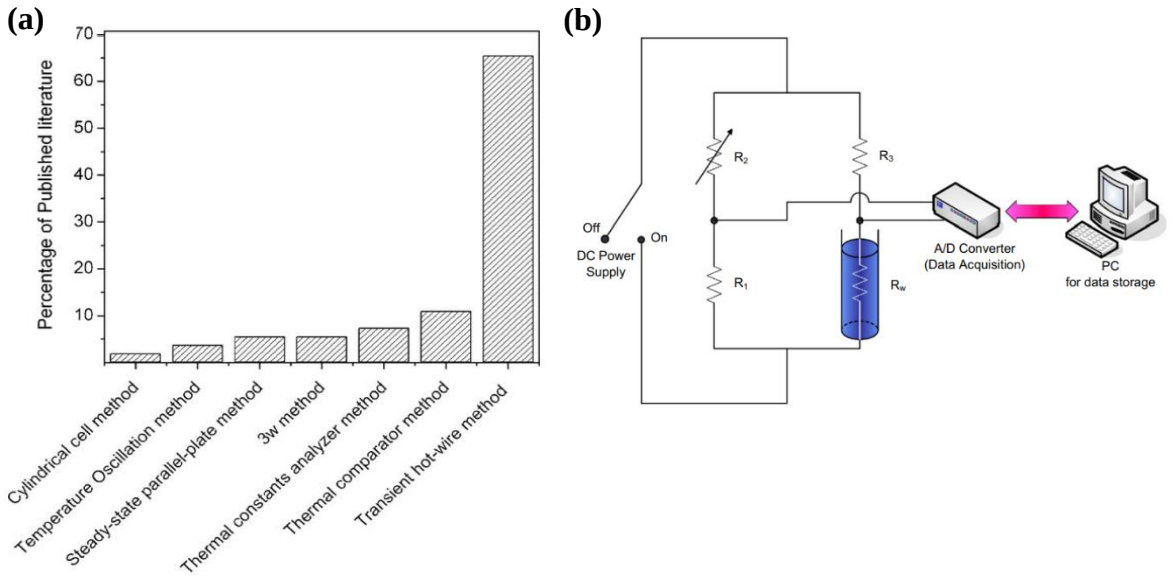

Figure 1.8: (a)The comparison of published literature on different thermal conductivity measurement techniques used for nanofluids [50] (b) The schematic of electrical circuit used in transient hot wire experiment set-up [51].

bridge, R_w is the resistance of the platinum wire which acts as a sensor as well as a thermometer. The length to diameter ratio of the wire was used at around 4100 to minimize error due to conduction at the end of the wire. A constant temperature chamber eliminates error due to variation in the room temperature during the measurement. The formula used to calculate the effective thermal conductivity of nanofluids can be expressed as

$$k_e = \left[\frac{q}{4\pi(\Delta T_2 - \Delta T_1)}\right] \ln\left(t_2/t_1\right) \tag{1.5}$$

When a constant current passes through the wire then the heat dissipated by the wire due to the Joule heating effect increasing the temperature of nanofluid as well as of wire. This temperature rise depends on the thermal conductivity of fluids placed around the platinum wire. The transient hot wire measurement technique was successfully used by many researchers like Zhang et al.[60], Timofeeva et al.[23], Merckx et al.[61], and Guo et al.[62], etc for the thermal conductivity measurement of various nanofluids.

1.5.1.2 Thermal Comparator (TC) method

The thermal comparator method is based on the principle that when two materials present at different temperatures are brought in contact over a very small area then heat flows from high-temperature material to low-temperature material which depends on the thermal conductivity of the materials. The thermal conductivity of these two materials in contact decides the temperature of the contact. The relation between the contact temperature and thermal conductivity of the materials can be expressed as [63]

$$T_c = \frac{k_1}{k_1 + k_2} T_0 \tag{1.6}$$

Where the test material is at 0 ^{0}C, k_1 and k_2 are the thermal conductivity of the probe and the test material, respectively, T_0 is the temperature of the probe.

On basis of this principle, Powell et al.[20] first time developed a thermal comparator method for thermal conductivity measurement of solid materials. Further, this method was developed to measure the thermal conductivity of fluids. Mukherjee et al.[63] proposed thermal conductivity measurement techniques and used them to measure the thermal conductivity of 28 different organic liquids at room temperature. Further, Paul et al.[57] developed in-house measurement techniques to measure the thermal conductivity of water and ethylene glycol-based zirconia (ZrO_2) and titania (TiO_2) nanofluids. The experimental setup is schematically

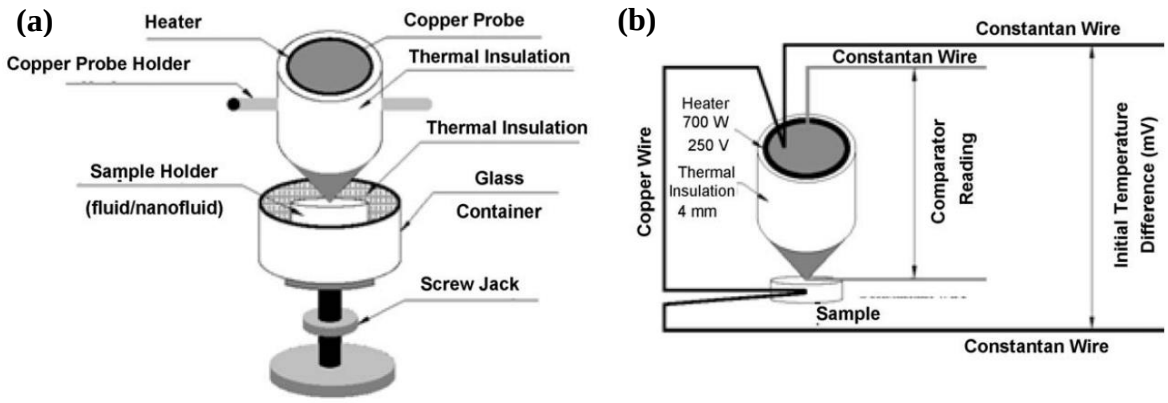

Figure 1.9: (a) Thermal comparator measurement setup for nanofluid's thermal conductivity (b) differential thermo-emf recording during measurement.[54]

shown in the Figure 1.9. The probe is made of copper and plays the most important role in the efficient thermal conductivity measurement as the heat flow from the probe to the fluid through a small area of contact. The heater in the setup maintains the uniform temperature around the copper probe. T-type copper-constantan thermocouple measured the initial temperature difference and it remains constant throughout the experiment as shown in Figure 1.9(b). The screw jack adjusts the sample height to ensure the point contact between probe and fluid. The temperature attained at point contact is the function of the thermal conductivity of the probe and fluid as given in Eq. 1.6. The proportional comparator measured the temperature of the point contact in the form of voltages and the thermal conductivity of the test fluid extract after converting the comparator reading using the calibration curve.

As this technique instantly measures the thermal conductivity so the convection effect is eliminated from the measurement results which further improves the precision of the device. This advantage motivates different researchers to measure thermal conductivity using thermal comparator [37], [64]. The main limitation of this technique is required large data sets with different known fluids to make a calibration curve for the comparator. The calibration process of this device is long as compared to other techniques.

1.5.1.3 3-Omega method

3-Omega (3ω) technique was first time made by Corbino et al.[65] in 1912 for the purpose to investigate the thermal diffusivity of the metal filament of an incandescent bulb. Later this technique was applied to nanofluids or fluids to evaluate the thermal conductivity by many investigators. In this method, a fine metal wire works as a heater as well as a thermometer for k measurement which is quite similar to the transient hot-wire method. This method also involves a radial flow of heat from the wire as in the THW method. The 3ω method utilizes temperature oscillations but THW used a time-dependent response to measure the thermal conductivity of the fluid. A fine metal wire was suspended inside the fluid and a sinusoidal electric current passed through the wire at frequency ω. This current at frequency ω in the wire further generates the heat at the frequency 2ω which results in a rise in the temperature. This temperature rise at the frequency 2ω can be extracted with the measurement of the 3ω component of the voltages. Cahill et al.[66] suggested the exact solution for the temperature

oscillations at a distance r = $(x^2+y^2)^{1/2}$ from the infinitely narrow line source of heat on the surface of an infinite half-volume is expressed as

$$\Delta T = \frac{P}{l\pi k} K_0(qr) \tag{1.7}$$

The thermal conductivity of the liquid k can be calculated by evaluating the value of the slope of temperature rise in the wire at frequency 2ω versus the applied frequency ω. The formula for the thermal conductivity can be written as

$$k = \frac{P}{4\pi l}\left(\frac{\partial T_{2\omega}}{\partial\, ln\omega}\right)^{-1} \tag{1.8}$$

Where the $T_{2\omega}$ is the amplitude of the temperature rise in the wire, ω is the applied frequency of the sinusoidal current, l is the length of the metal wire, and P is the applied power. The schematic of the 3ω thermal conductivity measurement apparatus used by Karthik et al.[67] to measure the thermal conductivity of CuO/DI nanofluids is shown in Figure 1.10. The thin platinum wire serves the purpose of a heater as well as a thermometer and Lock-in amplifier (SR830) used as a highly accurate phase-sensitive detector to extract the 3ω component of the voltage. The real part of the 3ω voltage oscillations is directly related to the temperature oscillations which contains the information regarding the thermal conductivity of the test fluids. 3ω technique has one advantage over the THW method is that temperature oscillation can be kept small in the fluid up to 1K which is about 5 K in the THW method.

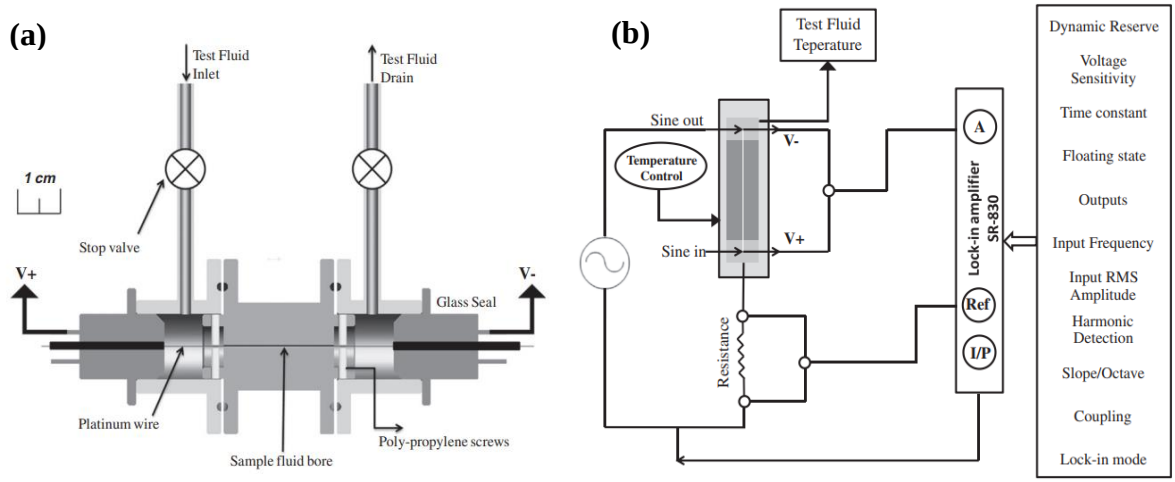

Figure 1.10: (a) Schematic representation and (b) Overall layout of 3ω measurement apparatus [64]

1.5.1.4 Laser flash method

In 1961, Parker et al.[68] proposed and designed the laser flash (LF) method mainly to measure the heat capacity, thermal diffusivity, and thermal conductivity of solid materials. Schrimpf et al.[69] applied this technique to metallic liquids that possess high thermal conductivity like mercury. Further, Tada et al.[70] used this technique for liquids of low thermal conductivity and achieve results with 2.6% uncertainty.

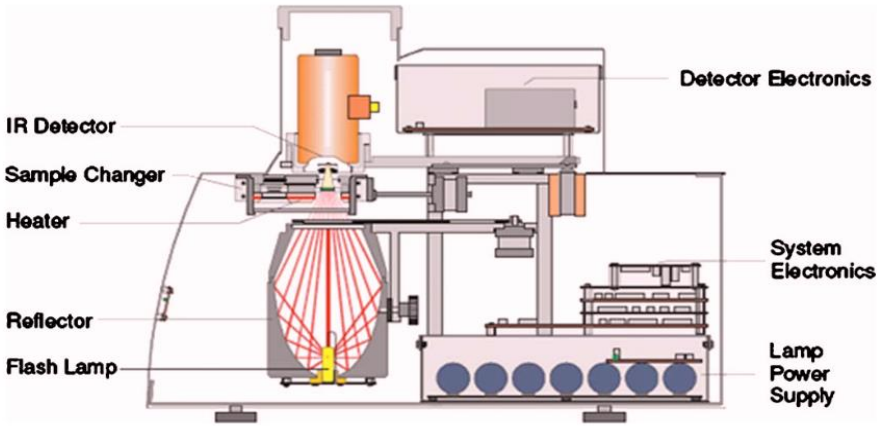

Figure 1.11: The diagram of the modern laser flash apparatus (LFA 447) [68]

Shaikh et al.[71] used the modern laser flash apparatus (LFA 447) as shown in the Figure 1.11 to measure the k of three different types of nanofluids with different loading of nanoparticles. The xenon flash lamp was used to produce the light pulse in the apparatus. The sample holder for liquid is different than solid materials. The bottom surface of the container and the lower surface of the lid are coated with thin graphene. The weighed test fluid was put in the container through a syringe. NANO FLASH software with recommended setting used to take readings. Accurate values of density and the specific heat are required for the thermal conductivity calculation of nanofluids.

In LF measurement technique, the thermal contact resistance is eliminated by using a laser pulse. The laser pulse can heat the sample directly where as, in other methods electrical current is used as a heat source. This method is perfectly suitable for the electrical conducting fluids as there is no electrical current leakage involved. The measurement time of this technique is short so this eliminated the error due to the natural convection effect of nanofluids. These superiorities motivate other researchers [72]–[74] to use this technique to measure k of different

types of nanofluids. This technique is not suitable to measure nanofluids that possess low thermal conductivity ask of container approximately same as the test fluids.[75]

1.5.1.5 Transient plane source (TPS) method

The transient plane source technique is also based on the transient principle and it is proposed by Gustafsson et al.[76] in 1990 to cover a large range of transport properties and also be able to apply it to a large number of different materials. Gustafsson proposed two possible designs for the TPS probes one in the shape of a hot disk and the other in the shape of a hot square. This method is also known as a thermal constant analyzer or Gustafsson probe. This method uses the Fourier law of heat conduction like the hot wire method for the measurement of thermal conductivity. In this method, a transient plane source (TPS) serves the purpose of heat source and temperature detection. This TPS probe in the shape of a hot disk consists of spiral metallic thin foil with the insulating layer of Kapton as shown in the Figure 1.12(b).

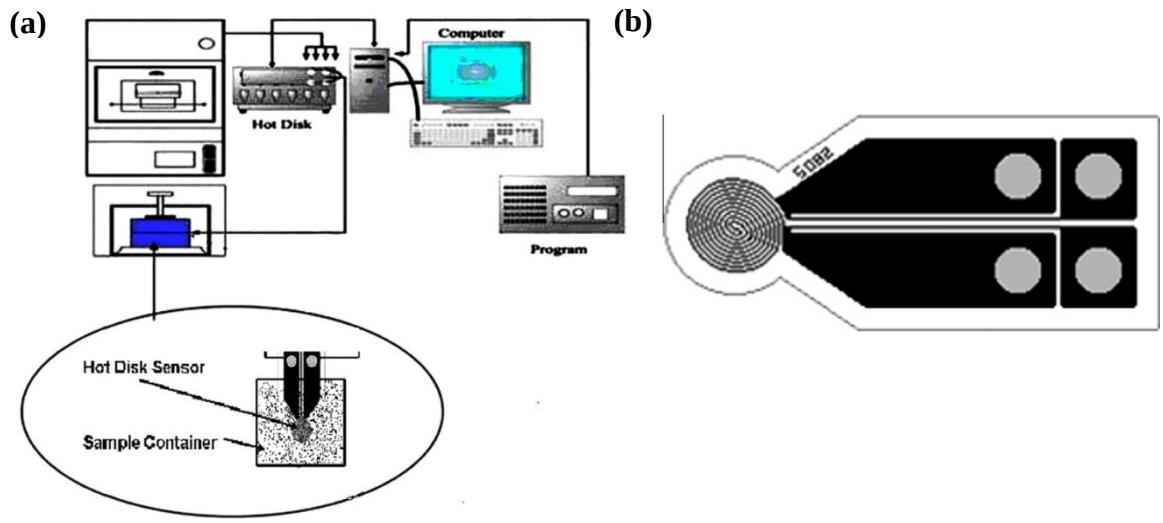

Figure 1.12: (a) The measurement set-up of the Transient plate source method (b) TPS Probe.[74]

The schematic of the transient plate source apparatus shown in Figure 1.12(a) used by Wan et al.[77] for the thermal conductivity and thermal diffusivity measurement of Polyaniline nanofibers/DI water nanofluids over a temperature range of 10-80 ^{0}C. When an electric current passed through the TPS probe then the temperature near the probe can be captured by measuring the change in the TPS probe's resistance using the given relation

$$R_p(\tau) = R_0(1 + \beta\Delta T(\tau)) \tag{1.9}$$

$$\Delta T(\tau) = \frac{1}{\beta}\left[\frac{R_p(\tau)}{R_0} - 1\right] \tag{1.10}$$

Where $\Delta T(\tau)$ is the temperature rise near the surface of the probe, β is the temperature coefficient of resistance, $R_0$is the resistance of the probe before heating and τ can be defined as the time of the electrification and can be written as

$$\tau = \sqrt{\frac{tk}{r_p^2}} \tag{1.11}$$

Where t is the time of measurement, k is the thermal diffusivity of test fluid, and r_p is the radius of the TPS probe.

For the case of disk type TPS probe the exact equation of temperature difference can be expressed as

$$\Delta T(\tau) = P_0(\pi^{3/2}ak)^{-1}D(\tau) \tag{1.12}$$

Where $D(\tau)$ is the geometric function. After fitting the experimental data to the straight line given by Eq. 1.12, the slope of the fitting straight line gives the values of $P_0(\pi^{3/2}ak)$ which is further used to calculate the thermal conductivity of the fluid.

The range of thermal conductivity measurement of this method typically lies between 0.2 W/mK to 200 W/mK and is very much flexible to the sample size[78]. These advantages encourage various inverstigators [77]–[82] to use this technique for the thermal conductivity measurement of different types of nanofluids. The optimal time window for a single transient recording for this method is around between 0.3s to 1.1s for the precise measurement of both thermal conductivity and thermal diffusivity.[83] Li et al.[84] suggested some corrections regarding the TPS probe to improve the accuracy of the measurement using this method. The heat capacity of the TPS probe and variation in the electrical resistance of the spiral foil influenced the measured power which is taken constantly by Gustafsson in the original TPS method. The correction of these two factors improves the accuracy of the measurement method by more than 2%.

1.5.2 Steady-state techniques

1.5.2.1 Steady-state parallel-plate technique

Based on the steady state heat conduction principle, many types of test cells are established to measure the thermal conductivity of the fluids and nanofluids. Out of these, either parallel plate type or concentric cylinder type design is preferred for efficient heat transfer in one direction.

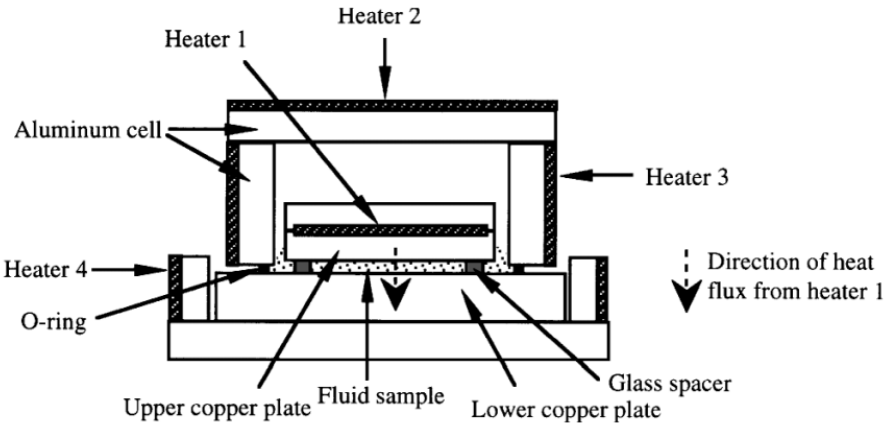

Figure 1.13: The schematic of the parallel plate thermal conductivity measurement apparatus.

The steady-state parallel-plate measurement method was developed based on the design of guarded hot-plate apparatus by Challoner and Powell[20]. The schematic diagram of the parallel plate method apparatus used by Wang et al.[29] to measure the thermal conductivity of Al_2O_3/H_2O and CuO/H_2O nanofluids with uncertainty less than ± 3% is shown in the Figure 1.13. In this apparatus, the small amount of fluid placed between two parallel plates of the copper plates and heater 1 provide the heat flux from the upper plate to the lower plate which flows through the fluid placed between the plates. Heater 2 and heater 3 were used to eliminate the convection and radiation from the upper plate by maintaining the temperature difference between the aluminium cell and the upper plate to less than 0.05 ^{0}C. The thermal conductivity is affected by glass spaced as placed across the two copper plates. So, the one-dimensional heat conduction equation is used to calculate the thermal conductivity after achieving the temperature equilibrium and this equation can be written as

$$k = \frac{\dot{q} * L_g}{S * \Delta T} \tag{1.13}$$

Where $\dot{q}$ is the heat flux per unit time from the heater1, L_g is the length of the glass spacer and S is the cross-sectional area of the copper plates used in the apparatus. ΔT is the temperature difference between the upper and lower plate. The effective thermal conductivity of the test fluid can be calculated after eliminating the effect of the glass spacer so it can be written as

$$k_e = \frac{k * S - k_g * S_g}{S - S_g} \tag{1.14}$$

Where k_g and S_g are thermal conductivity and cross-sectional area of glass spacer respectively. Basically, in this technique temperature does not change with time so the natural convection effect that occurs in the fluids is unavoidable at high temperatures and also it takes a longer time to estimate the thermal conductivity of the fluids. But still, investigators [85], [86] choose this measurement technique because of its simple design and reliable working equation.

1.6 Discussion on thermal conductivity measurement techniques

From the literature survey, it is observed that the THW method is mostly used by researchers to investigate the thermal properties of the nanofluids because of their well-known reputation in the scientific community. The design of the Steady-state parallel plate method is simple and easy to use but still, this method is least preferred to measure the thermal conductivity of nanofluids. Because the steady-state method not only takes a long time for the measurement but also, there is a large probability to produce erroneous results due to the natural convection of fluids.

The accuracy of the measurement technique depends on two important aspects which have been concerned during the measurement of the nanofluids. One aspect is the required time range of the measurement because the longer time range for the measurement can induce natural convection and eventually affect the accuracy of the measurement results. LF method is the fastest technique as compared to the other mentioned techniques. The measurement time range for the LF is in microseconds whereas the measurement time range for the THW is in 2-8 s.[75] The measurement time range of the TPS and THW methods is longer compared to the

LF but the measurement time is fast enough to avoid the natural convection from the measurement results. After selecting the specific time range for these methods, the significant deviation from the linearity in the graph can be avoided. TC is another technique with fast response as this measurement technique utilizes a probe for instant measurement after contacting the surface of the test nanofluid. On the other hand, the steady-state parallel technique required a large sample for the measurement so relatively it takes a longer time to heat the sample and measurement. The second aspect is the degree of disturbance of the measurement methods because the intense disturbance of the measurement techniques can agglomerate the nanoparticles in the nanofluids which can further affect the effective thermal conductivity results of the nanofluids. For example, when the hot wire probe is immersed in the nanofluids for the measurement then it may cause the agglomeration of nanoparticles in nanofluids. The same kind of effect can be observed in the TPS and 3ω technique. The design of the measurement techniques can reduce the disturbance in the measurement. However, TC and LF have done excellent work to minimize the disturbance on the measurement results of nanofluids. TC has minimized the disturbance with probe point contact measurement configuration and LF has the least disturbance since there is a laser beam heating the nanofluids without any contact and a detector placed outside to observe the changes.

In short, thermal conductivity measurement of nanofluids is a challenging task because of the unknown mechanism of thermal conductivity enhancement. In the literature, the validity of the measurement technique other than the THW has been questioned because lack of reported results measured by the same measuring technique to support their measurement data validity.[87] Due to wide recognition of its validity, the THW method is more commonly utilized by investigators to study the thermal properties of nanofluids.

1.7 Electrical Resistivity

Electrical resistivity or conductivity is one of the most fundamental physical properties of the material which can be derived from the accurately measured resistance through any standard technique like the four-point probe technique. Electrical conductivity is used to determine how well a material can conduct an electrical current. Electrical resistivity works as an indicator of changes in the chemical binding of the material. As electrical resistivity depends on the two parameters inversely: one is carrier density (n) and the other is carrier mobility (μ). The change

in the nature of the binding affects the carrier density and structural changes affect the carrier mobility of the system. Early investigations on the metals manifest that resistivity increases with temperature white it decreases in Si and Ge because semiconductors transform to conducting state with temperature. Electrical resistivity is used for the classification of the metal, semiconductor, and insulators ranging from 10^{-8} to 10^{16} Ohm cm [88].

The knowledge of the electrical transport properties becomes valuable since these properties are used for fundamental and technical application-driven research. Over time, these electrical transport properties play important role in characterizing different types of the materials such as anisotropic single crystals [89], [90], Anisotropic electrical resistance of mesoscopic $LaAlO_3/SrTiO_3$ devices [91], 2D superconductivity [92], metal single crystals [93], Organic thin films of semiconductors [94], [95], Anisotropic and thickness dependence conductivity of thin films [95], [96], electrical conductivity in two-dimensional (2D) samples like graphene and MoS_2 [97]–[99], different types of conventional and non-conventional superconductors [95], [100]–[102], Si nanowire and Si-based electronic devices [103], [104], even for energy storage devices such as electrolyte membrane fuel cells[105], batteries [106], multijunction solar cells [107] and also for biological specimen such as large scale brain dynamics[108], the conductivity of seizing and non-seizing mouse brain [109]. In the present scenario, the study of structural properties [110], [111]and phase transition [90], [112] have been very necessary for material science and engineering applications. When comes to the physical properties of the materials then the electrical conductivity of the materials becomes important for the understanding of the other physical phenomenon like topological materials [101], [106] quantum hall effect [99], quantum phase transitions [112], etc.

1.7.1 Electrical resistivity measurements methods

Many models and methods have been suggested depending on the contact resistance, shape, and nature of the sample to achieve better precision in electrical resistance measurement. Samples can be in the form of thin film, single crystal, small crystallite, or powder pellet. Electrical resistivity measurement techniques are mainly divided into three categories to be discussed here. First one is the two-probe resistivity measurement method which is mainly used to measure the resistivity of high resistive materials, second is the four-probe measurement

method or potential probe measurements which are best for the low resistive and single crystals. The third category includes Montgomery, van der Pauw and Smith techniques suitable for the pellets and bulk samples.

1.7.1.1 Two probes resistivity measurement

This is the simplest and easiest method to measure the resistivity of the materials. This method depends on the values of voltage (V) and current (I) measured across the material as shown in

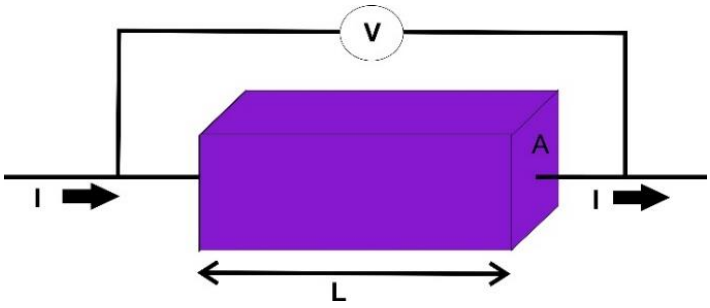

Figure 1.14: Resistivity measurement connections for two probe methods

the Figure 1.14. The value of resistivity ρ_R of the material is derived from the V and I through the given formula as

$$\rho_R = \frac{VA}{IL} \tag{1.15}$$

Where L is the length of the sample, A is the cross-sectional area of the sample, V is the potential difference measured through the voltmeter and I is the current measured through the ammeter. This method is preferred to measure the resistivity of the high resistive material like polymers films/sheets.

1.7.1.2 Four probe measurement

Four probe or potential probe has been widely used for the resistivity measurement of low resistive materials. In 1915, Frank Wenner [113] proposed an in-line four-point geometry to

exclude the contact resistance at the position of the probes to measure the resistivity of the earth. Contact and lead resistance are cancelled out through the four-probe technique; however, the contact resistance still emerges if it produces enough heat. In the two-probe method, this contact resistance is in series with the resistance of the sample leading to an incorrect resistance value for low resistive materials. In 1954, Leopoldo Valdes [114] used this measurement technique to measure the resistivity of semiconductor (Ge) for transistors. Figure 1.15 (a) and (b) shows the model and measurement circuit used for resistivity measurement of semi-infinite material.

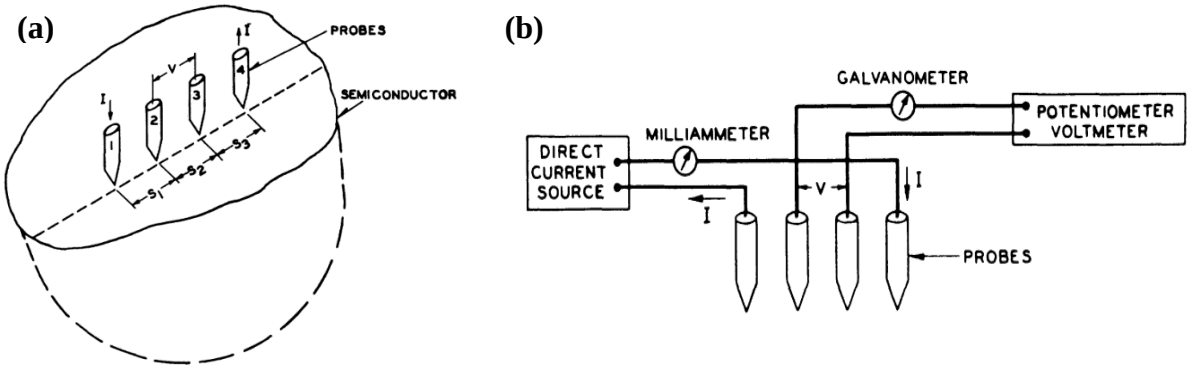

Figure 1.15: (a) Model for four-probe resistivity measurement (b) Electric circuit used for resistivity measurement [111]

In this method, all four probes are placed equidistant on the surface of semi-infinite samples in a straight line. The size of contact must be smaller than the distance between the probes and the sample surface should be flat with no leakage. The resistivity of the material can be calculated using the formula given in the Table 1.1.

Table 1.1: Linear four probe formulas for bulk resistivity or sheet resistance for semi-infinite 3D material, infinite 2D sheet, and 1D wire.

Sample Shape	4P in-line geometry
3D Bulk	$\rho_{R,3D}^{line} = 2\pi s \frac{V}{I}$
2D Sheet	$\rho_{R,2D}^{line} = \frac{\pi t}{\ln(2)} \frac{V}{I}$
1D Wire	$\rho_{R,1D} = \frac{\Sigma V}{s I}$

When these four sharp probes are placed on the flat surface of the material and the current I is passed through the outer probes using the source meter, then the voltmeter is used to measure the floating potential V across the inner electrodes, where s is the distance between the electrodes or probes. The ratio of the potential (V) over current (I) gives the resistance (R) of the Sample only. In the specific case when the distance between the probes (s) is very large as compared to the thickness (t) of the working sample (s >> t) then the resistivity can be calculated by the formula given in the Table 1. All the relations derived for the infinite 3D and 2D systems are summarized in Table 1. These equations indicate that the resistance is independent of probe spacing for the 2D case, but it decreases as 1/s with increasing the probe spacing for the 3D case and is experimentally confirmed in a report by Shiraki et al.[115]. Resistance increases linearly with the probe spacing for the 1D [116].

1.7.1.3 Van der Pauw method

Van der Pauw's method has great importance for resistivity and Hall coefficient measurement[117]. This method allows the use of arbitrary shapes as well as freedom for the placement of the contact leads. This method was discussed by Van der Pauw to measure the resistivity of the flat disc or pellet of arbitrary shape without knowing the current pattern. Van der Pauw [118] extends the formula for evaluating the correction factor corresponding to the finite lateral width of the sample for the special case of circular/square to any arbitrary shape. But the condition is that the four probes should be on the periphery of the samples and contacts should be point-like in size and smaller than the sample size. Moreover, for the applicability of this method the sample should be homogenous, isotropic, and singly connected. The sample

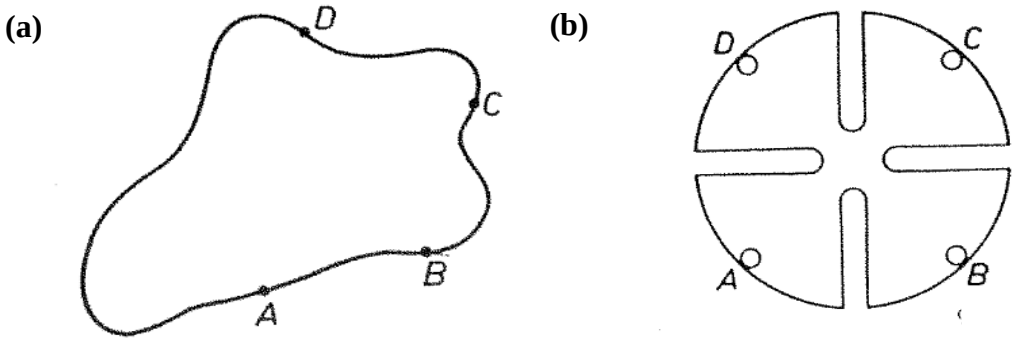

Figure 1.16: Van der Pauw samples with four contacts used for the resistivity measurement (a) An arbitrary shaped (b) Clover shaped [114]

should be sufficiently thin (i.e. t/s < 1/5). They considered an arbitrary-shaped flat sample as shown in the Figure 1.16. It has four contacts A, B, C, and D at different places along the circumference of the sample. The $R_{AB,\,CD}$ is the resistance of the sample which is defined as the ratio of the potential difference developed across the contacts C and D when the current passes through the contact A to B ($R_{AB,\,CD} = V_{CD}/I_{AB}$). $R_{BC,\,DA}$ can be defined similarly. Van der Pashowsown that these resistances satisfy the given condition:

$$e^{-\pi\left(\frac{t}{\rho_R}\right)R_{AB,CD}} + e^{-\pi\left(\frac{t}{\rho_R}\right)R_{BC,DA}} = 1 \tag{1.16}$$

where t is the thickness of the sample and ρ is the resistivity of the sample. For non-symmetric rib samples, as shown in Figure 1.16 (a), the resistivity equation generally demonstrates [118]

$$\rho_R = \frac{\pi t}{ln\,2}\left(\frac{R_{AB,CD} + R_{BC,DA}}{q}\right) f\left(\frac{R_{AB,CD}}{R_{BC,DA}}\right) \tag{1.17}$$

Where f is the function of the ratio $R_{AB,\,CD}$ / $R_{BC,\,DA}$. This equation allows the calculation of the resistivity values of any arbitrarily shaped sample after the measurement of two simple resistances values $R_{AB,\,CD}$ and $R_{BC,\,DA}$. Further, the function f satisfies the relation given below as

$$cosh\left\{\frac{ln\,2}{f}\frac{\frac{R_{AB,CD}}{R_{BC,DA}} - 1}{\frac{R_{AB,CD}}{R_{BC,DA}} + 1}\right\} = \frac{1}{2}e^{\frac{ln2}{f}} \tag{1.18}$$

$$f \approx 1 - \left(\frac{R_{AB,CD} - R_{BC,DA}}{R_{AB,CD} - R_{BC,DA}}\right)^2 \frac{ln2}{2} - \left(\frac{R_{AB,CD} - R_{BC,DA}}{R_{AB,CD} - R_{BC,DA}}\right)^4 \left\{\frac{(ln2)^2}{4} - \frac{(ln2)^3}{12}\right\} \tag{1.19}$$

In Figure 1.17 they plotted the f as a function of resistance ratio $R_{AB,\,CD}$ / $R_{BC,\,DA}$ The Eq. 1.19 further helps in the evaluation of f for symmetric samples shown in Fig. 1.17b, $R_{AB,\,CD}$ = $R_{BC,\,DA}$ = R so using the reciprocity theorem the first equation gives the formula of resistivity as shown below

$$\rho_R = \frac{\pi t}{ln\,2}\left(\frac{V}{I}\right) \tag{1.20}$$

In this case, a single resistance measurement is sufficient to calculate the resistivity of the sample. This is also valid for circular-shaped and square-shaped symmetric samples.

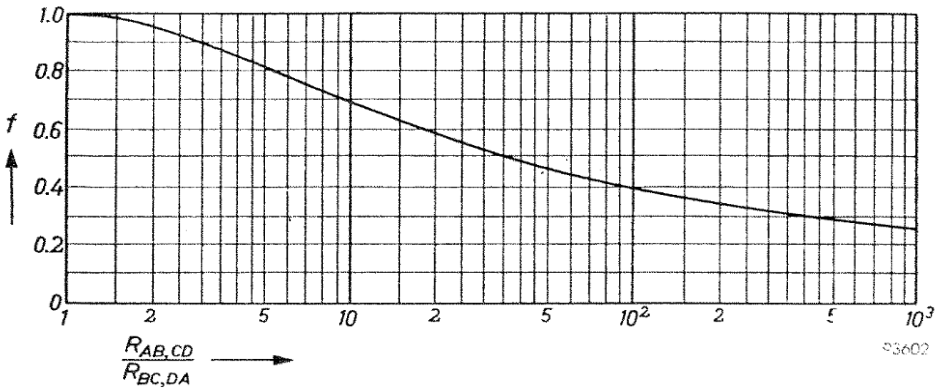

Figure 1.17: The geometrical factor f used to calculate the electrical resistivity of the material, plotted as a function of ratio of resistances in two different configuration $R_{AB,CD}$ / $R_{BC,DA}$.

This method was further modified and corrected by other researchers. Ronald Chwang et al. [119] reported in their study that the size of contact appreciable of the sample is a good approximation to the van der Pauw infinitesimal contact. The advantage of simplicity and the finite size of ohmic contact can be utilized for the measurement of normal semiconductor materials and still it was possible to obtain the precise measurement data using the correction factors determined in the report.

Van der Pauw calculated the errors due to the contact placement and size of the circular-shaped samples. In other reports, Daniel W. Koon [120] suggested that the use of cloverleaf or square samples can reduce the errors arising due to the size or displacement of the contact from the edge of the sample. The sharpness of the corners and the contact placement near the corners of the square samples help in reducing the measurement errors. The inhomogeneities in the resistivity further introduce the error proportional to the electric field in that region. The cloverleaf and the square shape may highlight the regions of inhomogeneity more than the circular shape. The square shape gave contact placement errors 10-100 times smaller than the circular shapes and all cloverleafs gave fewer errors than nonclovered shapes.[121]

Kasl and Hoch [122] studied the effect of the thickness on these measurement techniques. The accuracy of the technique deteriorates with the thickness of the sample and this method can be used for those samples where the thickness is comparable to the surface dimensions. Their investigation also suggested that the resistivity of an irregular thick sample with low resistance

electrodes on the entire edge, perpendicular to the surface can be measured through this technique as shown in Figure 1.18. The low resistance electrodes maintain an effective 2D current distribution.

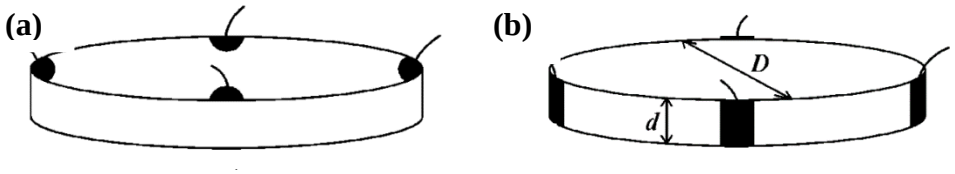

Figure 1.18: Two contact geometries on the pellets of diameter D (a) electrodes placed on the edge of circumference (b) electrodes are located across the edge. [118]

Jonathan D. Weiss et al.[123] derived the same formula from classical 3D electrodynamics for a conducting rectangular sample having thickness approaching non-zero to zero. They also studied the validity of van der Pauw's results using the formulation and semiconductor devise code for the finite thickness and finite contact area of four probes. Further Jonathan D. Weiss generalizes this work involving a square sample and a square array of electrodes that are not confined to the corners since this measurement configuration could be a more convenient one.[124]

1.7.1.4 Montgomery resistivity measurement method

The Montgomery method is one of the most conveniently used techniques to determine the electrical resistivity in different directions of the anisotropic materials.[125] In 1970 Montgomery [126] suggested a graphical method for identifying the resistivity of anisotropic materials in the form of a parallelepiped with three orthogonal l_1, l_2, and l_3 edges collinear to the three resistivity directions $\rho_{R,i = x,y,z}$ as shown in the Figure 1.19. In 2011 this method was further modified by dos Santos et al.[127] to solve the problem analytically. This method can be used for a rectangular prism of finite thickness with two distinct resistivity components ρ_1, $\rho_2 = \rho_3$.[126], [127] This modified method of Montgomery is derived based on Wasscher transformations.[128] Logan et al.[129] defined resistance $R_1 = V_1/I_1$ for the isotropic

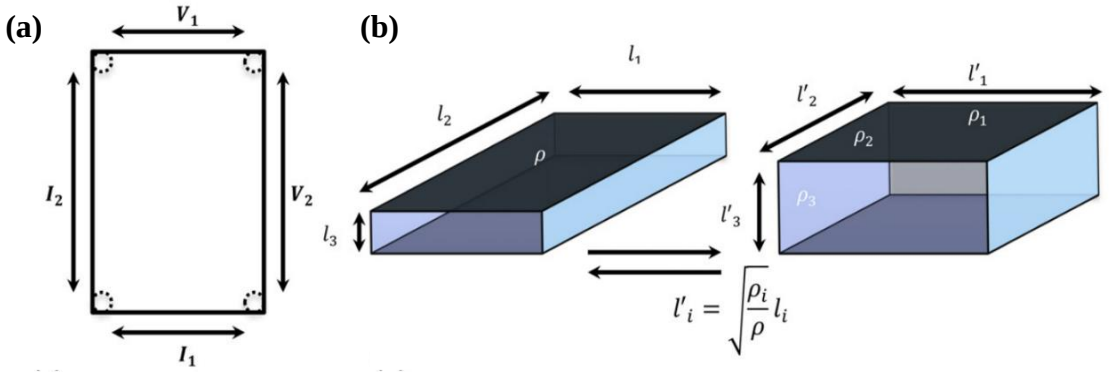

Figure 1.19: (a) The schematic of contacts on rectangular surface used for the Montgomery method (b) Wasscher method for mapping of an anisotropic parallelepiped on an isotropic parallelepiped and vice versa.[121,123]

rectangular prism having dimensions l_1,l_2, and l_3 as shown in figures (a) and (b). Where I_1 is the current applied through two contacts placed on the edge of the surface l_1l_2 and the voltage V_1 is the potential drop measured through a voltmeter across the two opposite edges of the same surface l_1l_2 as shown in the Figure 1.19 (a) and (b). They manifest that the resistivity ρ of the rectangular prism depends on R_1 through two correction factors E and H_1 as given below

$$\rho_{R1} = EH_1R_1 \tag{1.21}$$

Where E is the correction factor that accounts for the finite thickness of the isotropic sample and H_1 corresponds to the correction factors related to the finite lateral dimensions. Now when the probes of current and voltages exchange with each other then the relationship can be written as

$$\rho_{R2} = EH_2R_2 \tag{1.22}$$

Logan et al.[129] used the method of images for the evaluation of the correction factor H_1 expressed as

$$\frac{1}{H_1} = \frac{4}{\pi}\sum_{n=0}^{\infty} \frac{2}{\left[[2n+1]\,sinh[\,\pi\left((2n+1)\frac{l_2}{l_1}\right)\right]} \tag{1.23}$$

And similarly, the correction factor E can be expressed as

$$\frac{E}{l_3} = \frac{l_1 \sum_{l=0}^{\infty} \left[(2l+1)\, sinh[\,\pi\left((2n+1)\frac{l_2}{l_1}\right)\right]^{-1}}{\sum_{l=0}^{\infty} \sum_{n=0}^{\infty} \left[\frac{\epsilon_n}{[s \sinh(\pi s l_2)]}\right]^{-1}} \tag{1.24}$$

Where s = $[(2h+1)/l_1)^2 + (n/l_3)^2]^{\frac{1}{2}}$, $\epsilon_0 = 0$ and $\epsilon_n = 2$ for n > 0. Montgomery determined these correction factors using the interpolation method but in the revision of the Montegomery method, dos Santos et al.[127] simplified these series through an analytical equation then the correction factor H_1 can be expressed as

$$H_1 \approx \frac{\pi}{8} sinh\left(\pi \frac{l_2}{l_1}\right) \tag{1.25}$$

After applying the approximation of $0.2 < l_3/(l_1\, l_2)^{1/2} < 2^{1/2}$ for the two cases corresponding to the thick and thin films, the equation for E can be expressed as

$$\frac{E}{l_3} \approx \frac{1}{\left(1 + e^{-\pi\left[\frac{(l_1 l_2)^{\frac{1}{2}}}{l_3} - \frac{2^{\frac{1}{2}}}{2}\right]}\right)} \tag{1.26}$$

Further, Wasscher equation was used for mapping the thin anisotropic parallelopiped with dimensions l_1', l_2', l_3' with three resistivity components in three different directions $\rho_{R1,}\rho_{R2,}$ and ρ_{R3} onto an isotropic rectangle. The equation used for the mapping expressed as

$$\rho_R = \sqrt[3]{\rho_{R_1}\rho_{R_2}\rho_{R_3}} \tag{1.27}$$

$$l_{i=1,2,3} = l_i' \sqrt[2]{\frac{\rho_{R_i}}{\rho_R}} \tag{1.28}$$

For the case $E \approx l_3$, the Logan relation can be written in terms of other resistivity components as given below

$$\rho_R = l_3'^{\,2}\sqrt{\frac{\rho_{R_3}}{\rho_R}}\,H_1R_1 \tag{1.29}$$

$$\rho_{R_1} \approx \frac{\pi}{8}\left(\frac{l_3'l_2'}{l_1'}\right)\frac{l_1}{l_2}R_1\sinh\left(\frac{\pi l_2}{l_1}\right) \tag{1.30}$$

Similarly, the second component ρ_2 can be obtained by simply replacing the $l_1(l_1')$ with $l_2(l_2')$. The ratio l_1/l_2 can be expressed in terms of the resistance R_1 and R_2 measured on the face of $l_1'l_2'$. So the ratio l_2/l_1 can be written as

$$\frac{l_2}{l_1} \approx \frac{1}{2}\left[\frac{1}{\pi}ln\frac{R_2}{R_1} + \sqrt{\left(\frac{1}{\pi}ln\frac{R_2}{R_1}\right)^2 + 4}\right] \tag{1.31}$$

So two simple resistance measurements and revised Montgomery equations allow for to calculation of the resistivity components of the thin anisotropic rectangular samples after assuming directions known and well defined.

1.8 Photoconductivity

Photoconductivity refers to the phenomenon of enhancement or diminution of the electrical conductivity upon illumination of the light. This photoconductivity phenomenon is generally observed in covalently bonded semiconductors and insulators, where the conductivity is low in the dark, and significant enhancement can be investigated. The thermal equilibrium density of the free carriers in the material leads to the conductivity in the dark which is known as dark current. This dark current or dark conductivity has to be subtracted from the measured current in the presence of the light to acquire the actual amount of the photocurrent. The magnitude of the photocurrent during the illumination depends on three separate processes, first is the generation of free electrons and holes through absorption of the photons, the second is the transport of carriers in the material under the influence of the electric field and the third is the recombination process of electrons and holes. The study of these processes offers insights into the structure and electronic properties of the material under investigation. Photoconductivity of the material depends on various factors such as the frequency and the intensity of the

illuminating light, and the temperature of the material. The photoconductive behavior of the material can reveal significant information regarding the distribution of electronic states in the material, carrier generation, and recombination processes. The knowledge about the absorption coefficient and distribution of the defects present in the material can be investigated from the information on the three processes involved in the photoconductivity phenomenon. The low absorption coefficient can be responsible for the low photoconductivity of the material at the given frequency of light illumination but at the same time, this low photoconductivity may be due to the binary recombination of the photo-induced electron-hole or the formation of the excitons. Therefore, to differentiate between the alternative interpretations sufficiently, comprehensive experimental data will be required in terms of the system parameter for the analysis. The use of different types of photoconductivity experiments is recommended such as photoluminescence or charge collection. Bube et al. and Rose et al. discuss the general principle of photoconductivity in their monographs.[130]–[132]

1.9 Photoconductivity measurement techniques

A large variety of experimental techniques have been developed and used over the years depending on the photoconductivity phenomenon. The experimental techniques are mainly divided into two categories, first is steady-state photoconductivity (SSPC) and the second is transient photoconductivity (TPC). The steady-state photoconductivity (SSPC) mainly focuses on the stationary photocurrent under constant illumination but the transient photoconductivity (TPC) experiments deal with time evolution photocurrent under pulsed excitation. Both measurement techniques can be used to study the recombination and electronic density of states of material under illumination.

1.9.1 Steady-state photoconductivity (SSPC) method

Steady-state photoconductivity is the simplest measurement technique that utilizes a constant monochromatic light source to produce the excess number of electrons or holes in the material under illumination. The excess density of electrons and holes enhances the conductivity of the material which can be expressed as

$$\sigma_{ph} = e(\mu_n \Delta n + \mu_p \Delta p) \tag{1.32}$$

Where e is the charge of an electron, μ_n and μ_p are electron and hole mobility, Δn and Δp are the enhancement of electrons and hole density, respectively. The diagram of the steady-state

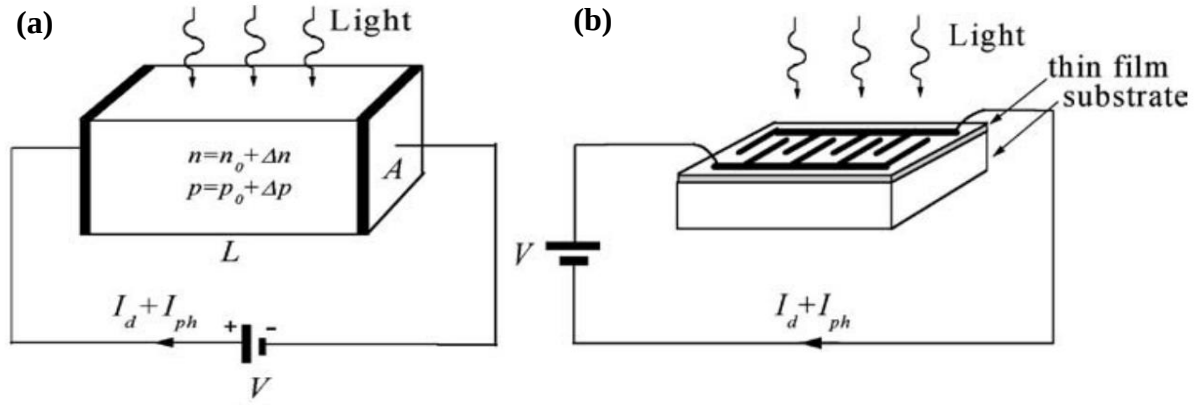

Figure 1.20:(a) Basic electrical circuit for the photoconductivity measurement of Bulk material, V is applied voltage, L is the length of sample, A is cross-sectional area of sample, n_o, p_0 and I_d are carrier density and the current in the dark, I_{ph}, is the current produced during light illumination, Δn and Δp are the carrier density increment under light illumination (b) The type of electrode configuration is adopted for the thin film sample.

photoconductivity experiment is schematically shown in Figure 1.20. Where V and L are the voltage applied across the terminal, and A is the cross-sectional area of the bulk rectangular sample.

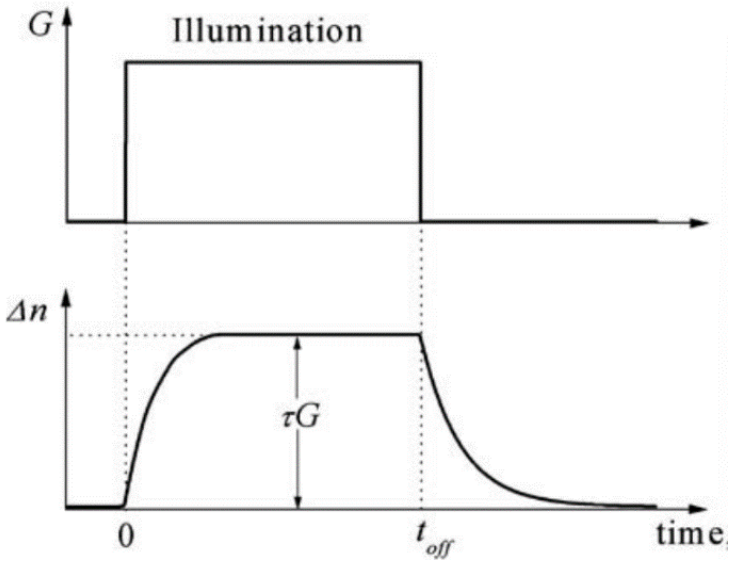

Figure 1.21: Schematic of generation of excess charges carries density Δn under the illumination of light as a function of time.

The applied electric field across the block is $E = V/L$, and the photocurrent I_{ph} will be equal to $\sigma_{ph}AE$. Both end surfaces of the rectangular block are made metallic to work as an electrode in the circuit. In the present scenario, most investigators are interested in thin films rather than bulk, so an electrical circuit with interdigitated electrodes is shown in Figure 1.20 (b). This configuration of electrodes is frequently used for photoconductivity measurement. The whole part of Δn and Δp does not contribute to photoconductivity because a fraction of photo-induced carriers is trapped in the various defects present in the materials. The information of this trapping is reflected in the values of the mobilities μ_n and μ_p that is lower than the theoretical free-carriers mobility μ_0. In most of the materials either $\mu_n\Delta n$ or $\mu_p\Delta p$ part turns out to be much larger than the other part due to the presence of strongly unequal charge carrier mobilities. In those cases, Eq. 1.32 reduces to one type of carrier equation.

Mobility in the product $\mu_n\Delta n$ or $\mu_p\Delta p$ is the material parameter that depends on the temperature and sample characteristics. The photoinduced carrier density can be expressed in terms of the generation rate of free electrons and holes (G) and the average lifetime (τ_i) of the excess carriers. Eq. 1.32 can be expressed as

$$\sigma_{ph} = eG(\mu_n\tau_n + \mu_p\tau_p) \tag{1.33}$$

The generation rate G can be defined as

$$G = \eta\left(\frac{I_0}{hv}\right)(1-R)\frac{(1-e^{-\alpha d})}{d} \tag{1.34}$$

Where η is the quantum efficiency of the generation process, hv is the photon energy, R is the reflection coefficient of the sample, α is the optical absorption coefficient of the material, I_0 is the intensity of the light illumination and d is the sample thickness. Three parameters η, R and α depend on the wavelength of the light used in the experiment. The monochromatic light reveals the energy-resolved information about the sample but the white light will give only a global average. The relation between the steady state values of Δn and G is schematically shown in Figure 1.21**.** The build-up and decay of excess charge carrier (Δn) upon the turn on and off the light illumination.

SSPC measurement offers the possibility of determining the absorption coefficient as a function of incoming photon energy that explores the electronic density of the states around the band gap of the material.[133] SSPC measurement can also determine the recombination levels of the defects of the governing sample.[134], [135]

1.9.2 Transient photoconductivity (TPC) method

The study of the transient characteristic of photoconductivity relates to either the response or relaxation of steady-state photocurrent. In traditional transient photoconductivity (TPC) measurement, a short light pulse excited the charge carriers into the transport band at time t = 0 s. All the carriers are in thermal equilibrium before the start of the experiment. The trapping sites for electrons above the Fermi energy and holes below the Fermi energy level are empty. The photoinduced carriers move under the influence of the electric field of the circuit. Before recombination, these carriers immobilize due to several defect traps present in the material. The carriers are released from the trap through the thermally activated process with activation energy equal to trap depth. The immobilization time of the carriers depends on the depth of the trap, the more the depth lower will be the transient current. As the shallower trap release the carriers sooner, retrapping of those carriers will lead to an increasing occupation of the deeper traps and further reduces the current level. So traditionally the experiments are carried out in the secondary photocurrent mode where the sample is supplied with ohmic electrical contacts and carrier loss by the recombination only. Electrodes in the Co-planar geometry are preferred in this technique. Rudenko et al.[136] give an expression to link the transient current with the distribution of localized states. As long as recombination is neglected, the following expression can be used as a first-order estimation

$$g(E) \propto [I(t) \cdot t]^{-1} \tag{1.35}$$

Where *g(E)* is the density of states (DOS), $I(t)$ is transient current and t is time. The solution for the special case of an exponential electronic density of states is

$$g(E) \propto exp(-E/E_0), \qquad E = k_B T \, ln(v_0 t) \tag{1.36}$$

The distribution of trapping levels leads to a power law for the transient current as given below

$$I(t) \propto t^{-(1-\alpha)} \tag{1.37}$$

Where $\alpha = k_B T/E_0$, $k_B T$ is Boltzmann energy, v_0 is the attempt-to-escape frequency, E_0 is the width of the exponential distribution that can be deduced from the slope of the power law

decay of the current. The difficulties posed in time domain analysis of the transient current can be avoided by transposing the current decay into the frequency domain through Fourier transform.[137] Not only Fourier transform but also Laplace transforms techniques have been applied to convert the TPC signals into DOS information.[138]

1.10 Tunning of 2DEG conductivity using visible light illumination

The discovery of two-dimensional electron gas (2DEG) at the LAO/STO interface has evoked enthusiasm for interactive research and attracted much attention in the past decade. This 2DEG becomes an attractive platform for nanoelectronics. 2DEG not only possesses high charge carrier density and mobility but also exhibits a wide range of properties like the coexistence of ferromagnetism and superconductivity, magnetism, planar hall effect, anomalous hall effect, Rashba spin-orbit interaction, etc. The 2DEG conductivity can be easily tuned using different external stimuli like the electric field, light illumination, mechanical pressure, stress, strain, etc.[139], [140] for fundamental and technological applications. Light and electric fields have been extensively used as external stimuli to tune the electronic properties of the 2DEG lying at the interface of oxide heterostructures. We will study the effect of light illumination on the 2DEG.

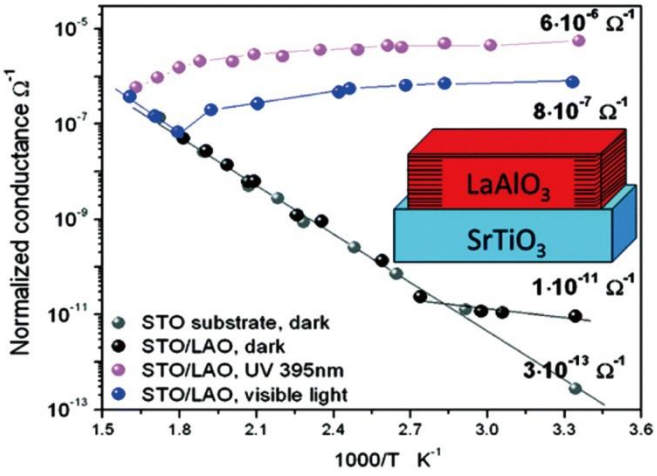

Figure 1.22: Temperature dependence normalized conductance plot for bare STO in dark and LAO/ STO interface in dark, UV light (395 nm) and visible light illumination. Inset shows the schematic of the LAO/ STO heterostructure.[135]

Electronic properties of 2DEG at the oxide interface can be tuned using visible light as external stimuli that lead to the understanding of its fundamental physics and also opened new pathways for the oxide-optoelectronics devices.[141] Several years ago in 2012, Tebano et al. [142] reported the sensitivity of the $LaAlO_3/SrTiO_3$ (LAO/STO) interface under light illumination. It was observed that the electrons present at the valence band of STO are excited to the conduction band of STO under light illumination. These photoinduced charge carriers are responsible for the enhancement in the conductivity of the oxide interface. The sudden increase of conductivity under light is termed Transient photoconductivity (TPC). If this high conductivity state persists for a long period with a high relaxation time of the charge carriers, then it is defined as Persistent photoconductivity (PPC).[142], [143] The oxygen vacancies and band bending could be the reason for the high relaxation time of the charge carriers.[144] The small magnitude of PPC has been observed at room temperature in many semiconductors such as silicon nanowire [145], GaN nanowires [146], GaAs/AlGaAs [147], etc. Tebano et al.[142] have observed giant PPC at a fully oxidized LAO/STO oxide interface under the illumination of UV light having a wavelength of 395 nm or blue light as shown in the Figure 1.23. The photoconductivity is increased by 5 orders of magnitude in the presence of UV light which is much larger than the present semiconductors. The reason for the origin of PPC is the separation of the trapped photoexcited electrons due to strong interfacial barrier potential and holes lying in the valence band. The residual oxygen vacancies located inside the energy gap of STO behaves as electrons trap centre [148] are also responsible for the significant PPC at the LAO/STO interface.

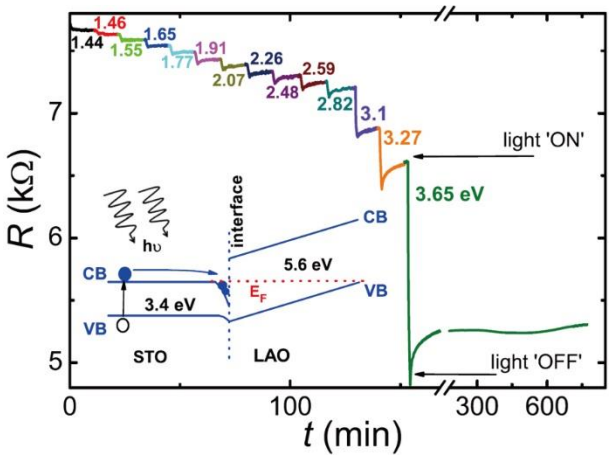

Figure 1.23: Sheet resistance under the light illumination as a function of time having energy from 1.44 to 3.65 eV at temperature 4.2K. Inset shows the schematic of the LAO/STO band diagram.[142]

Guduru et al.[149] performed the experiment at the conducting LAO/STO interface using light illumination of energy lying between 1.44 eV to 3.65 eV at 4.2 K as shown in the Figure 1.23**.** The change in the magnitude of resistance was small for the photon energy values less than the band gap of STO but this change enhanced to 50% for the photon energy values equal to 3.5 eV or above. Hall measurements have been performed to reveal the origin of the photo response. The transition from linear to the nonlinear hall has been observed under light illumination and this suggests the creation of an additional conducting channel under light illumination. There is a report by Lu et al.[150] also demonstrated an insulator to metal transition in the presence of light for the LAO/STO oxide interface.

Further, Aswin et al.[151] conducted a photoconductivity experiment after substituting Al with Cr ion in $LaAl_{0.6}Cr_{0.4}O_3$/STO. The enhancement of electron correlation due to the 3d character of the Cr ion leads to a large photo response. Chan et al.[152] observed a giant optical switching effect at the LAO/STO interface after surface modification by Pd nanoparticles. The photoconductivity on/off ratio of around 750% was observed under the UV light illumination as shown in Figure 1.24 (b)**.** In this case, the catalytic effect of Pd nanoparticles and interface/surface coupling has been considered the origin of the giant photo response. Similarly, Rastogi et al.[153] have studied the photo response after inserting an insulating layer of the $LaMnO_3$ at the interface of LAO/STO. The enhanced photo response has been observed for δ-doped LAO/STO compared to bare LAO/STO under the same photon energy

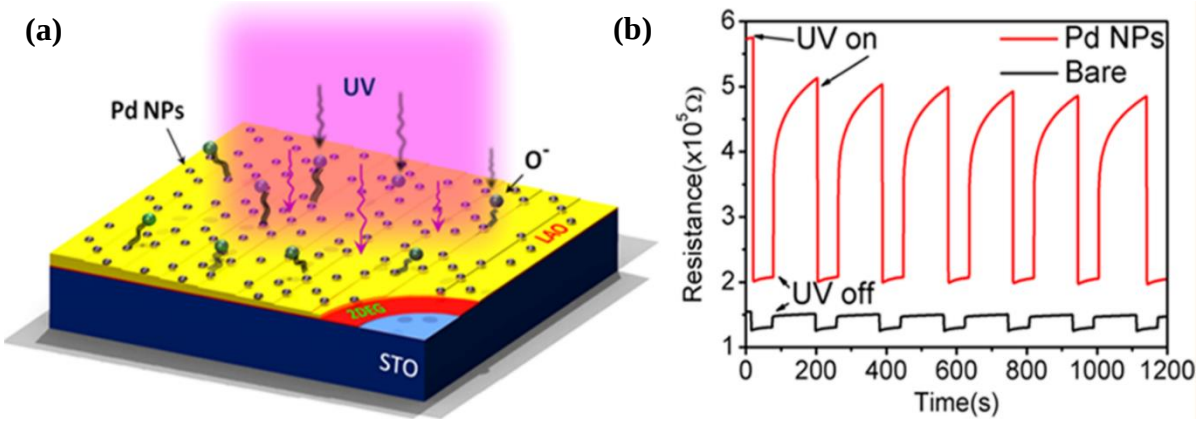

Figure 1.24: (a) Diagram of the Pd nanoparticle modulated $LaAlO_3$/ $SrTiO_3$ oxide heterostructure. (b) Resistance behavior with time under the illumination of UV light [145]

In addition, Liu et al.[154] reported negative photoconductivity (NPC) at the LAO/STO heterojunction grown at low oxygen partial pressure, as shown in Figure 1.25. Light-assisted Hall measurement revealed that the electron mobility was reduced under light illumination. The PPC effect at the oxide interface offers potential for the photoelectronic application like solar cells, photodetectors, optical switches, holographic memory, etc. [140], [150], [155].

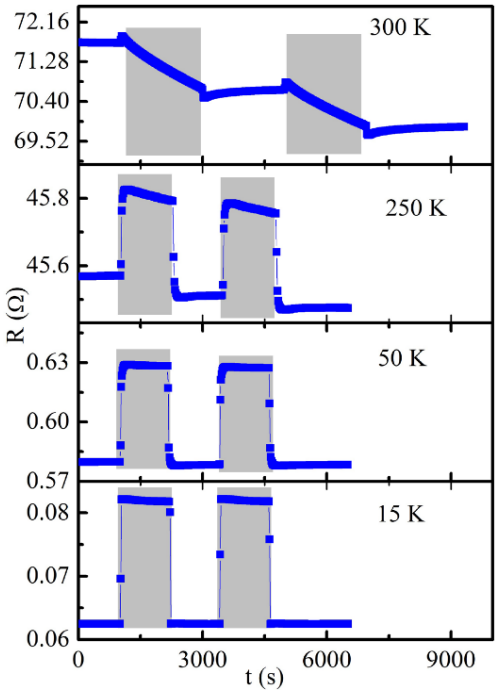

Figure 1.25: The variation of resistance under the light illumination for the low oxygen pressure sample at different fixed temperatures

1.11 Outlook of thesis

The main objective of this thesis is to understand the electron and phonon transport mechanism at the surface and the interface of heterostructure nanomaterials using three different experimental measurement approaches, which are thermal, electrical, and photoconductivity. We made transient hot wire measurement setup in our lab to investigate the thermal conductivity of iron oxide nanofluids and iron oxide based cellulose hybrids for better understanding of the surface contribution to the heat transfer mechanism which has not been explored earlier. On the other hand, the Van der Pauw resistivity measurement technique was used to investigate the electrical properties of polyaniline nanocomposites. Next, we study the

effect of light on the 2DEG at the new interface of LAO/STO and EuO/KTO, which were not explored till now. The whole work of the thesis is divided into six chapters as follows:

The **first chapter** of the thesis discusses the importance of nanofluids, major factors affecting the thermal properties of nanofluids and different conventional methods used to measure the thermal conductivity. Different types of electrical and photoconductivity measurement approaches are also discussed in brief. This gives us an idea of choosing an efficient measurement technique to investigate the specific properties of any material. The **second chapter** includes the description of various characterization and measurement techniques used to carry out the research work of this thesis. Characterization techniques such as X-ray diffraction (XRD), Transmission electron microscopy (TEM), Infrared spectroscopy (IR), thermogravimetric analysis (TGA), UV-VIS-NIR spectroscopy have been discussed, which are used to identify the crystal structure, morphology, compound identification, amount of different components, and band gap of the test material. The measurement techniques included the detailed description of the transient hot wire method, Van der Pauw and four point probe methods to investigate the thermal, electrical and photoconductivity of nanomaterials. In the **third chapter**, the thermal conductivity of the water and toluene-based iron oxide nanofluids has been measured using the homemade transient hot wire measurement setup and discuss the effect of the different type of surfactants on the heat transfer properties of polar and nonpolar iron oxide nanofluids. This method also investigated the thermal properties of iron oxide-based cellulose hybrids for thermal insulation applications. The **fourth chapter** describes the effect of different types of dopants and morphology on the electrical properties of the polyaniline using the Van der Pauw measurement method. The impact of acid dopants such as HCl, CSA, CA on the electrical conductivity of polyaniline nanofibers is demonstrated in detail. Different synthesis methods lead to varying morphologies of polyaniline nanofibers, which further affects the electrical conductivity has been also discussed. In **the fifth chapter**, the optical tuning of the 2DEG at the two new oxide heterostructure interfaces, i.e., LVO/STO and EuO/KTO, is discussed in detail. The effect of temperature, carrier density, wavelength, and power of the light illumination on the photoconductivity and persistent photoconductivity of these two different interfaces is described in detail. The **sixth chapter** summarizes the whole research work done in this thesis and discusses the future possibilities or applications of this research work.

References:

[1] H. Younes, M. Mao, S. S. Murshed, D. Lou, H. Hong, and G. Peterson, "Nanofluids: Key parameters to enhance thermal conductivity and its applications," *Appl. Therm. Eng.*, p. 118202, 2022.

[2] S. Özerinç, S. Kakaç, and A. G. Yazıcıoğlu, "Enhanced thermal conductivity of nanofluids: a state-of-the-art review," *Microfluid. Nanofluidics*, vol. 8, no. 2, pp. 145–170, 2010.

[3] R. Lenin, P. A. Joy, and C. Bera, "A review of the recent progress on thermal conductivity of nanofluid," *J. Mol. Liq.*, vol. 338, p. 116929, 2021.

[4] B.-X. Wang, L.-P. Zhou, and X.-F. Peng, "A fractal model for predicting the effective thermal conductivity of liquid with suspension of nanoparticles," *Int. J. Heat Mass Transf.*, vol. 46, no. 14, pp. 2665–2672, 2003.

[5] B. Mehta and D. Subhedar, "Review on mechanism and parameters affecting thermal conductivity of nanofluid," *Mater. Today Proc.*, vol. 56, pp. 2031–2037, 2022.

[6] S. U. Choi and J. A. Eastman, "Enhancing thermal conductivity of fluids with nanoparticles," Argonne National Lab.(ANL), Argonne, IL (United States), 1995.

[7] N. P. Cheremisinoff, "Encyclopedia of fluid mechanics. Vol. I: Flow phenomena and measurement," 1986.

[8] B. C. Pak and Y. I. Cho, "Hydrodynamic and heat transfer study of dispersed fluids with submicron metallic oxide particles," *Exp. Heat Transf. Int. J.*, vol. 11, no. 2, pp. 151–170, 1998.

[9] Y. Xuan and W. Roetzel, "Conceptions for heat transfer correlation of nanofluids," *Int. J. Heat Mass Transf.*, vol. 43, no. 19, pp. 3701–3707, 2000.

[10] M. Kole and T. Dey, "Viscosity of alumina nanoparticles dispersed in car engine coolant," *Exp. Therm. Fluid Sci.*, vol. 34, no. 6, pp. 677–683, 2010.

[11] C. Nguyen *et al.*, "Temperature and particle-size dependent viscosity data for water-based nanofluids–hysteresis phenomenon," *Int. J. Heat Fluid Flow*, vol. 28, no. 6, pp. 1492–1506, 2007.

[12] S. Murshed, K. Leong, and C. Yang, "Investigations of thermal conductivity and viscosity of nanofluids," *Int. J. Therm. Sci.*, vol. 47, no. 5, pp. 560–568, 2008.

[13] D. P. Kulkarni, D. K. Das, and G. A. Chukwu, “Temperature dependent rheological property of copper oxide nanoparticles suspension (nanofluid),” *J. Nanosci. Nanotechnol.*, vol. 6, no. 4, pp. 1150–1154, 2006.

[14] J. Lee and I. Mudawar, “Assessment of the effectiveness of nanofluids for single-phase and two-phase heat transfer in micro-channels,” *Int. J. Heat Mass Transf.*, vol. 50, no. 3–4, pp. 452–463, 2007.

[15] R. Chein and J. Chuang, “Experimental microchannel heat sink performance studies using nanofluids,” *Int. J. Therm. Sci.*, vol. 46, no. 1, pp. 57–66, 2007.

[16] H. Masuda, A. Ebata, and K. Teramae, “Alteration of thermal conductivity and viscosity of liquid by dispersing ultra-fine particles. Dispersion of Al2O3, SiO2 and TiO2 ultra-fine particles,” 1993.

[17] S. Lee, S.-S. Choi, S. Li and, and J. Eastman, “Measuring thermal conductivity of fluids containing oxide nanoparticles,” 1999.

[18] S. Choi, Z. G. Zhang, Wl. Yu, F. Lockwood, and E. Grulke, “Anomalous thermal conductivity enhancement in nanotube suspensions,” *Appl. Phys. Lett.*, vol. 79, no. 14, pp. 2252–2254, 2001.

[19] J. A. Eastman, S. Choi, S. Li, W. Yu, and L. Thompson, “Anomalously increased effective thermal conductivities of ethylene glycol-based nanofluids containing copper nanoparticles,” *Appl. Phys. Lett.*, vol. 78, no. 6, pp. 718–720, 2001.

[20] A. Challoner and R. Powell, “Thermal conductivities of liquids: new determinations for seven liquids and appraisal of existing values,” *Proc. R. Soc. Lond. Ser. Math. Phys. Sci.*, vol. 238, no. 1212, pp. 90–106, 1956.

[21] W. Yu, H. Xie, L. Chen, and Y. Li, “Investigation of thermal conductivity and viscosity of ethylene glycol based ZnO nanofluid,” *Thermochim. Acta*, vol. 491, no. 1–2, pp. 92–96, 2009.

[22] W. Duangthongsuk and S. Wongwises, “Measurement of temperature-dependent thermal conductivity and viscosity of TiO2-water nanofluids,” *Exp. Therm. Fluid Sci.*, vol. 33, no. 4, pp. 706–714, 2009.

[23] E. V. Timofeeva *et al.*, “Thermal conductivity and particle agglomeration in alumina nanofluids: experiment and theory,” *Phys. Rev. E*, vol. 76, no. 6, p. 061203, 2007.

[24] R. L. Hamilton and O. Crosser, “Thermal conductivity of heterogeneous two-component systems,” *Ind. Eng. Chem. Fundam.*, vol. 1, no. 3, pp. 187–191, 1962.

[25] D. Bruggeman, “The calculation of various physical constants of heterogeneous substances. I. The dielectric constants and conductivities of mixtures composed of isotropic substances,” *Ann. Phys.*, vol. 416, pp. 636–791, 1935.

[26] W. Yu and S. Choi, “The role of interfacial layers in the enhanced thermal conductivity of nanofluids: a renovated Maxwell model,” *J. Nanoparticle Res.*, vol. 5, no. 1, pp. 167–171, 2003.

[27] J. C. Maxwell, *A treatise on electricity and magnetism*, vol. 1. Clarendon press, 1873.

[28] Y. Xuan, Q. Li, and W. Hu, “Aggregation structure and thermal conductivity of nanofluids,” *AIChE J.*, vol. 49, no. 4, pp. 1038–1043, 2003.

[29] X. Wang, X. Xu, and S. U. Choi, “Thermal conductivity of nanoparticle-fluid mixture,” *J. Thermophys. Heat Transf.*, vol. 13, no. 4, pp. 474–480, 1999.

[30] D. Lee, “Thermophysical properties of interfacial layer in nanofluids,” *Langmuir*, vol. 23, no. 11, pp. 6011–6018, 2007.

[31] H. Xie, J. Wang, T. Xi, Y. Liu, and F. Ai, “Dependence of the thermal conductivity of nanoparticle-fluid mixture on the base fluid,” *J. Mater. Sci. Lett.*, vol. 21, no. 19, pp. 1469–1471, 2002.

[32] D. Hasselman and L. F. Johnson, “Effective thermal conductivity of composites with interfacial thermal barrier resistance,” *J. Compos. Mater.*, vol. 21, no. 6, pp. 508–515, 1987.

[33] M.-S. Liu, M. C.-C. Lin, I.-T. Huang, and C.-C. Wang, “Enhancement of thermal conductivity with carbon nanotube for nanofluids,” *Int. Commun. Heat Mass Transf.*, vol. 32, no. 9, pp. 1202–1210, 2005.

[34] C. H. Li and G. Peterson, “Experimental investigation of temperature and volume fraction variations on the effective thermal conductivity of nanoparticle suspensions (nanofluids),” *J. Appl. Phys.*, vol. 99, no. 8, p. 084314, 2006.

[35] M. Chopkar, S. Sudarshan, P. Das, and I. Manna, “Effect of particle size on thermal conductivity of nanofluid,” *Metall. Mater. Trans. A*, vol. 39, no. 7, pp. 1535–1542, 2008.

[36] C. H. Chon, K. D. Kihm, S. P. Lee, and S. U. Choi, “Empirical correlation finding the role of temperature and particle size for nanofluid (Al 2 O 3) thermal conductivity enhancement,” *Appl. Phys. Lett.*, vol. 87, no. 15, p. 153107, 2005.

[37] M. Chopkar, P. K. Das, and I. Manna, “Synthesis and characterization of nanofluid for advanced heat transfer applications,” *Scr. Mater.*, vol. 55, no. 6, pp. 549–552, 2006.

[38] M. P. Beck, Y. Yuan, P. Warrier, and A. S. Teja, "The effect of particle size on the thermal conductivity of alumina nanofluids," *J. Nanoparticle Res.*, vol. 11, no. 5, pp. 1129–1136, 2009.

[39] H. A. Mintsa, G. Roy, C. T. Nguyen, and D. Doucet, "New temperature dependent thermal conductivity data for water-based nanofluids," *Int. J. Therm. Sci.*, vol. 48, no. 2, pp. 363–371, 2009.

[40] S. Murshed, K. Leong, and C. Yang, "Enhanced thermal conductivity of TiO2—water based nanofluids," *Int. J. Therm. Sci.*, vol. 44, no. 4, pp. 367–373, 2005.

[41] E. V. Timofeeva, J. L. Routbort, and D. Singh, "Particle shape effects on thermophysical properties of alumina nanofluids," *J. Appl. Phys.*, vol. 106, no. 1, p. 014304, 2009.

[42] M.-S. Liu, M. C.-C. Lin, C. Tsai, and C.-C. Wang, "Enhancement of thermal conductivity with Cu for nanofluids using chemical reduction method," *Int. J. Heat Mass Transf.*, vol. 49, no. 17–18, pp. 3028–3033, 2006.

[43] C. H. Li, W. Williams, J. Buongiorno, L.-W. Hu, and G. Peterson, "Transient and steady-state experimental comparison study of effective thermal conductivity of Al2O3/ water nanofluids," *J. Heat Transf.*, vol. 130, no. 4, 2008.

[44] S. K. Das, N. Putra, P. Thiesen, and W. Roetzel, "Temperature dependence of thermal conductivity enhancement for nanofluids," *J Heat Transf.*, vol. 125, no. 4, pp. 567–574, 2003.

[45] A. Turgut, I. Tavman, M. Chirtoc, H. Schuchmann, C. Sauter, and Sjij. Tavman, "Thermal conductivity and viscosity measurements of water-based TiO2 nanofluids," *Int. J. Thermophys.*, vol. 30, no. 4, pp. 1213–1226, 2009.

[46] Y. Ding, H. Alias, D. Wen, and R. A. Williams, "Heat transfer of aqueous suspensions of carbon nanotubes (CNT nanofluids)," *Int. J. Heat Mass Transf.*, vol. 49, no. 1–2, pp. 240–250, 2006.

[47] P. Keblinski, S. Phillpot, S. Choi, and J. Eastman, "Mechanisms of heat flow in suspensions of nano-sized particles (nanofluids)," *Int. J. Heat Mass Transf.*, vol. 45, no. 4, pp. 855–863, 2002.

[48] H. Zhu, C. Zhang, S. Liu, Y. Tang, and Y. Yin, "Effects of nanoparticle clustering and alignment on thermal conductivities of Fe 3 O 4 aqueous nanofluids," *Appl. Phys. Lett.*, vol. 89, no. 2, p. 023123, 2006.

[49] K. Hong, T.-K. Hong, and H.-S. Yang, "Thermal conductivity of Fe nanofluids depending on the cluster size of nanoparticles," *Appl. Phys. Lett.*, vol. 88, no. 3, p. 031901, 2006.

[50] W. Evans, R. Prasher, J. Fish, P. Meakin, P. Phelan, and P. Keblinski, “Effect of aggregation and interfacial thermal resistance on thermal conductivity of nanocomposites and colloidal nanofluids,” *Int. J. Heat Mass Transf.*, vol. 51, no. 5–6, pp. 1431–1438, 2008.

[51] X. Wang and D. Zhu, “Investigation of pH and SDBS on enhancement of thermal conductivity in nanofluids,” *Chem. Phys. Lett.*, vol. 470, no. 1–3, pp. 107–111, 2009.

[52] L. Yu-Hua, Q. Wei, and F. Jian-Chao, “Temperature dependence of thermal conductivity of nanofluids,” *Chin. Phys. Lett.*, vol. 25, no. 9, p. 3319, 2008.

[53] Y. S. Ju, J. Kim, and M.-T. Hung, “Experimental study of heat conduction in aqueous suspensions of aluminum oxide nanoparticles,” *J. Heat Transf.*, vol. 130, no. 9, 2008.

[54] J. Buongiorno *et al.*, “A benchmark study on the thermal conductivity of nanofluids,” *J. Appl. Phys.*, vol. 106, no. 9, p. 094312, 2009.

[55] K. D. Antoniadis, G. J. Tertsinidou, M. J. Assael, and W. A. Wakeham, “Necessary conditions for accurate, transient hot-wire measurements of the apparent thermal conductivity of nanofluids are seldom satisfied,” *Int. J. Thermophys.*, vol. 37, no. 8, pp. 1–22, 2016.

[56] B. Stalhane and S. Pyk, “New method for determining the coefficients of thermal conductivity,” *Tek Tidskr*, vol. 61, no. 28, pp. 389–393, 1931.

[57] G. Paul, M. Chopkar, I. Manna, and P. Das, “Techniques for measuring the thermal conductivity of nanofluids: a review,” *Renew. Sustain. Energy Rev.*, vol. 14, no. 7, pp. 1913–1924, 2010.

[58] M. J. Assael, A. R. Goodwin, V. Vesovic, and W. A. Wakeham, *Experimental thermodynamics volume IX: advances in transport properties of fluids*. Royal society of Chemistry, 2014.

[59] J.-H. Lee *et al.*, “Effective viscosities and thermal conductivities of aqueous nanofluids containing low volume concentrations of Al2O3 nanoparticles,” *Int. J. Heat Mass Transf.*, vol. 51, no. 11–12, pp. 2651–2656, 2008.

[60] X. Zhang, H. Gu, and M. Fujii, “Effective thermal conductivity and thermal diffusivity of nanofluids containing spherical and cylindrical nanoparticles,” *Exp. Therm. Fluid Sci.*, vol. 31, no. 6, pp. 593–599, 2007.

[61] B. Merckx, P. Dudoignon, J. Garnier, and D. Marchand, “Simplified transient hot-wire method for effective thermal conductivity measurement in geo materials: microstructure and saturation effect,” *Adv. Civ. Eng.*, vol. 2012, 2012.

[62] W. Guo, G. Li, Y. Zheng, and C. Dong, “Measurement of the thermal conductivity of SiO2 nanofluids with an optimized transient hot wire method,” *Thermochim. Acta*, vol. 661, pp. 84–97, 2018.

[63] A. Mukherjee and T. Das, “Determination of thermal conductivity of organic liquids and liquid mixtures by thermal comparator method,” *J. Indian Inst. Sci.*, vol. 67, no. 3 & 4, p. 75, 1987.

[64] R. Nottenburg, K. Rajeshwar, R. Rosenvold, and J. DuBow, “Measurement of thermal conductivity of Green River oil shales by a thermal comparator technique,” *Fuel*, vol. 57, no. 12, pp. 789–795, 1978.

[65] O. Corbino, “Measurement of specific heats of metals at high temperatures,” *Atti Della R. Accad. Naz. Dei Lincei*, vol. 21, pp. 181–188, 1912.

[66] D. G. Cahill, “Thermal conductivity measurement from 30 to 750 K: the 3ω method,” *Rev. Sci. Instrum.*, vol. 61, no. 2, pp. 802–808, 1990.

[67] R. Karthik, R. H. Nagarajan, B. Raja, and P. Damodharan, “Thermal conductivity of CuO–DI water nanofluids using 3-ω measurement technique in a suspended micro-wire,” *Exp. Therm. Fluid Sci.*, vol. 40, pp. 1–9, 2012.

[68] W. Parker, R. Jenkins, C. Butler, and G. Abbott, “Flash method of determining thermal diffusivity, heat capacity, and thermal conductivity,” *J. Appl. Phys.*, vol. 32, no. 9, pp. 1679–1684, 1961.

[69] J. Schriempf, “A laser flash technique for determining thermal diffusivity of liquid metals at elevated temperatures,” *Rev. Sci. Instrum.*, vol. 43, no. 5, pp. 781–786, 1972.

[70] Y. Tada, M. Harada, M. Tanigaki, and W. Eguchi, “Laser flash method for measuring thermal conductivity of liquids—application to low thermal conductivity liquids,” *Rev. Sci. Instrum.*, vol. 49, no. 9, pp. 1305–1314, 1978.

[71] S. Shaikh, K. Lafdi, and R. Ponnappan, “Thermal conductivity improvement in carbon nanoparticle doped PAO oil: An experimental study,” *J. Appl. Phys.*, vol. 101, no. 6, p. 064302, 2007.

[72] J. A. Narvaez, “Thermal conductivity of poly-alpha-olefin (pao)-based nanofluids,” 2010.

[73] N. Li, Y.-X. Zeng, Z.-Q. Liu, X.-W. Zhong, and S. Chen, “Nanofluids containing stearic acid-modified CuO nanorods and their thermal conductivity enhancements,” *Nanosci. Nanotechnol. Lett.*, vol. 7, no. 4, pp. 314–317, 2015.

[74] T. Wang, Z. Luo, and S. Guo, “Preparation of controllable nanofluids and research on thermal conductivity,” *J.-ZHEJIANG Univ. Eng. Sci.*, vol. 41, no. 3, p. 514, 2007.

[75] C. Kleinstreuer and Y. Feng, “Experimental and theoretical studies of nanofluid thermal conductivity enhancement: a review,” *Nanoscale Res. Lett.*, vol. 6, no. 1, pp. 1–13, 2011.

[76] S. E. Gustafsson, “Transient plane source techniques for thermal conductivity and thermal diffusivity measurements of solid materials,” *Rev. Sci. Instrum.*, vol. 62, no. 3, pp. 797–804, 1991.

[77] M. Wan, R. Yadav, K. Yadav, and S. Yadaw, “Synthesis and experimental investigation on thermal conductivity of nanofluids containing functionalized Polyaniline nanofibers,” *Exp. Therm. Fluid Sci.*, vol. 41, pp. 158–164, 2012.

[78] D. Zhu, X. Li, N. Wang, X. Wang, J. Gao, and H. Li, “Dispersion behavior and thermal conductivity characteristics of Al2O3–H2O nanofluids,” *Curr. Appl. Phys.*, vol. 9, no. 1, pp. 131–139, 2009.

[79] W. Jiang, G. Ding, and H. Peng, “Measurement and model on thermal conductivities of carbon nanotube nanorefrigerants,” *Int. J. Therm. Sci.*, vol. 48, no. 6, pp. 1108–1115, 2009.

[80] X. Li, D. Zhu, X. Wang, N. Wang, J. Gao, and H. Li, “Thermal conductivity enhancement dependent pH and chemical surfactant for Cu-H2O nanofluids,” *Thermochim. Acta*, vol. 469, no. 1–2, pp. 98–103, 2008.

[81] N. Nikkam *et al.*, “Novel nanofluids based on mesoporous silica for enhanced heat transfer,” *J. Nanoparticle Res.*, vol. 13, no. 11, pp. 6201–6206, 2011.

[82] X. Wang, X. Li, and S. Yang, “Influence of pH and SDBS on the stability and thermal conductivity of nanofluids,” *Energy Fuels*, vol. 23, no. 5, pp. 2684–2689, 2009.

[83] V. Bohac, M. K. Gustavsson, L. Kubicar, and S. E. Gustafsson, “Parameter estimations for measurements of thermal transport properties with the hot disk thermal constants analyzer,” *Rev. Sci. Instrum.*, vol. 71, no. 6, pp. 2452–2455, 2000.

[84] Y. Li *et al.*, “Improving the accuracy of the transient plane source method by correcting probe heat capacity and resistance influences,” *Meas. Sci. Technol.*, vol. 25, no. 1, p. 015006, 2013.

[85] C. H. Li and G. Peterson, “The effect of particle size on the effective thermal conductivity of Al 2 O 3-water nanofluids,” *J. Appl. Phys.*, vol. 101, no. 4, p. 044312, 2007.

[86] M. M. Kostic and C. J. Walleck, “Design of a steady-state, parallel-plate thermal conductivity apparatus for nanofluids and comparative measurements with transient HWTC apparatus,” presented at the ASME International Mechanical Engineering Congress and Exposition, 2010, vol. 44298, pp. 1457–1464.

[87] S. Aberoumand, A. Jafarimoghaddam, M. Moravej, H. Aberoumand, and K. Javaherdeh, "Experimental study on the rheological behavior of silver-heat transfer oil nanofluid and suggesting two empirical based correlations for thermal conductivity and viscosity of oil based nanofluids," *Appl. Therm. Eng.*, vol. 101, pp. 362–372, 2016.

[88] R. A. Serway and J. W. Jewett, *Principles of physics*, vol. 1. Saunders College Pub. Fort Worth, TX, 1998.

[89] K. A. Borup, K. F. Fischer, D. R. Brown, G. J. Snyder, and B. B. Iversen, "Measuring anisotropic resistivity of single crystals using the van der Pauw technique," *Phys. Rev. B*, vol. 92, no. 4, p. 045210, 2015.

[90] S. Hsieh *et al.*, "Anisotropy in the thermal hysteresis of resistivity and charge density wave nature of single crystal SrFeO3-δ: X-ray absorption and photoemission studies," *Sci. Rep.*, vol. 7, no. 1, pp. 1–11, 2017.

[91] N. J. Goble *et al.*, "Anisotropic electrical resistance in mesoscopic LaAlO3/SrTiO3 devices with individual domain walls," *Sci. Rep.*, vol. 7, no. 1, pp. 1–9, 2017.

[92] S. Ichinokura *et al.*, "Vortex-induced quantum metallicity in the mono-unit-layer superconductor NbS e 2," *Phys. Rev. B*, vol. 99, no. 22, p. 220501, 2019.

[93] J. Y. Kim *et al.*, "Abnormal drop in electrical resistivity with impurity doping of single-crystal Ag," *Sci. Rep.*, vol. 4, no. 1, pp. 1–5, 2014.

[94] C. Rolin, E. Kang, J.-H. Lee, G. Borghs, P. Heremans, and J. Genoe, "Charge carrier mobility in thin films of organic semiconductors by the gated van der Pauw method," *Nat. Commun.*, vol. 8, no. 1, pp. 1–9, 2017.

[95] S. Dutta *et al.*, "Thickness dependence of the resistivity of platinum-group metal thin films," *J. Appl. Phys.*, vol. 122, no. 2, p. 025107, 2017.

[96] T. Flatten *et al.*, "Direct measurement of anisotropic conductivity in a nanolaminated (Mn0. 5Cr0. 5) 2GaC thin film," *Appl. Phys. Lett.*, vol. 115, no. 9, p. 094101, 2019.

[97] G.-H. Lee, G.-H. Park, and H.-J. Lee, "Observation of negative refraction of Dirac fermions in graphene," *Nat. Phys.*, vol. 11, no. 11, pp. 925–929, 2015.

[98] F. Qing *et al.*, "A general and simple method for evaluating the electrical transport performance of graphene by the van der Pauw–Hall measurement," *Sci. Bull.*, vol. 63, no. 22, pp. 1521–1526, 2018.

[99] J. Yin *et al.*, "Dimensional reduction, quantum Hall effect and layer parity in graphite films," *Nat. Phys.*, vol. 15, no. 5, pp. 437–442, 2019.

[100] H.-H. Kuo, J.-H. Chu, J. C. Palmstrom, S. A. Kivelson, and I. R. Fisher, "Ubiquitous signatures of nematic quantum criticality in optimally doped Fe-based superconductors," *Science*, vol. 352, no. 6288, pp. 958–962, 2016.

[101] G. Balakrishnan, L. Bawden, S. Cavendish, and M. Lees, "Superconducting properties of the In-substituted topological crystalline insulator SnTe," *Phys. Rev. B*, vol. 87, no. 14, p. 140507, 2013.

[102] S.-G. Jung *et al.*, "Enhanced critical current density in the pressure-induced magnetic state of the high-temperature superconductor FeSe," *Sci. Rep.*, vol. 5, no. 1, pp. 1–7, 2015.

[103] S. Rollo, D. Rani, W. Olthuis, and C. Pascual García, "Single step fabrication of Silicon resistors on SOI substrate used as Thermistors," *Sci. Rep.*, vol. 9, no. 1, pp. 1–7, 2019.

[104] A. I. Hochbaum *et al.*, "Enhanced thermoelectric performance of rough silicon nanowires," *Nature*, vol. 451, no. 7175, pp. 163–167, 2008.

[105] Y. Chen, C. Jiang, and C. Cho, "Characterization of effective in-plane electrical resistivity of a gas diffusion layer in polymer electrolyte membrane fuel cells through freeze–thaw thermal cycles," *Energies*, vol. 13, no. 1, p. 145, 2019.

[106] Z. P. Cano *et al.*, "Batteries and fuel cells for emerging electric vehicle markets," *Nat. Energy*, vol. 3, no. 4, pp. 279–289, 2018.

[107] J. Zeitouny, E. A. Katz, A. Dollet, and A. Vossier, "Band gap engineering of multi-junction solar cells: Effects of series resistances and solar concentration," *Sci. Rep.*, vol. 7, no. 1, pp. 1–9, 2017.

[108] B. Pesaran *et al.*, "Investigating large-scale brain dynamics using field potential recordings: analysis and interpretation," *Nat. Neurosci.*, vol. 21, no. 7, pp. 903–919, 2018.

[109] M. Elbohouty, M. T. Wilson, L. J. Voss, D. A. Steyn-Ross, and L. A. Hunt, "In vitro electrical conductivity of seizing and non-seizing mouse brain slices at 10 kHz," *Phys. Med. Biol.*, vol. 58, no. 11, p. 3599, 2013.

[110] L. Peng, S. A. Wells, C. R. Ryder, M. C. Hersam, and M. Grayson, "All-electrical determination of crystal orientation in anisotropic two-dimensional materials," *Phys. Rev. Lett.*, vol. 120, no. 8, p. 086801, 2018.

[111] T. Pardoen *et al.*, "A versatile lab-on-chip test platform to characterize elementary deformation mechanisms and electromechanical couplings in nanoscopic objects," *Comptes Rendus Phys.*, vol. 17, no. 3–4, pp. 485–495, 2016.

[112] Q. Tao *et al.*, "Nonmonotonic anisotropy in charge conduction induced by antiferrodistortive transition in metallic SrTiO 3," *Phys. Rev. B*, vol. 94, no. 3, p. 035111, 2016.

[113] F. Wenner, *A method of measuring earth resistivity*, no. 258. US Government Printing Office, 1916.

[114] L. B. Valdes, "Resistivity measurements on germanium for transistors," *Proc. IRE*, vol. 42, no. 2, pp. 420–427, 1954.

[115] I. Shiraki, F. Tanabe, R. Hobara, T. Nagao, and S. Hasegawa, "Independently driven four-tip probes for conductivity measurements in ultrahigh vacuum," *Surf. Sci.*, vol. 493, no. 1–3, pp. 633–643, 2001.

[116] P. Paiano, P. Prete, N. Lovergine, and A. Mancini, "Size and shape control of GaAs nanowires grown by metalorganic vapor phase epitaxy using tertiarybutylarsine," *J. Appl. Phys.*, vol. 100, no. 9, p. 094305, 2006.

[117] F. S. Oliveira, L. G. Guimaraes, C. A. M. dos Santos, B. S. de Lima, and M. S. da Luz, "Electrical and thermodynamic study of SrTiO3 reduction using the van der Pauw method," *Mater. Chem. Phys.*, vol. 263, p. 124428, 2021.

[118] O. Philips'Gloeilampenfabrieken, "A method of measuring specific resistivity and Hall effect of discs of arbitrary shape," *Philips Res Rep*, vol. 13, no. 1, pp. 1–9, 1958.

[119] R. Chwang, B. Smith, and C. Crowell, "Contact size effects on the van der Pauw method for resistivity and Hall coefficient measurement," *Solid-State Electron.*, vol. 17, no. 12, pp. 1217–1227, 1974.

[120] D. W. Koon, "Effect of contact size and placement, and of resistive inhomogeneities on van der Pauw measurements," *Rev. Sci. Instrum.*, vol. 60, no. 2, pp. 271–274, 1989.

[121] D. W. Koon, A. A. Bahl, and E. O. Duncan, "Measurement of contact placement errors in the van der Pauw technique," *Rev. Sci. Instrum.*, vol. 60, no. 2, pp. 275–276, 1989.

[122] C. Kasl and M. Hoch, "Effects of sample thickness on the van der Pauw technique for resistivity measurements," *Rev. Sci. Instrum.*, vol. 76, no. 3, p. 033907, 2005.

[123] J. D. Weiss, R. J. Kaplar, and K. E. Kambour, "A derivation of the van der Pauw formula from electrostatics," *Solid-State Electron.*, vol. 52, no. 1, pp. 91–98, 2008.

[124] J. D. Weiss, "Generalization of the van der Pauw relationship derived from electrostatics," *Solid-State Electron.*, vol. 62, no. 1, pp. 123–127, 2011.

[125] I. Khalid, “A Brief Review on the Electrical Resistivity Of Aluminium Alloy and its Nanoparticles at Low Temperature,” *Comput. Exp. Res. Mater. Renew. Energy*, vol. 5, no. 2, pp. 133–141, 2022.

[126] H. Montgomery, “Method for measuring electrical resistivity of anisotropic materials,” *J. Appl. Phys.*, vol. 42, no. 7, pp. 2971–2975, 1971.

[127] C. Dos Santos *et al.*, “Procedure for measuring electrical resistivity of anisotropic materials: A revision of the Montgomery method,” *J. Appl. Phys.*, vol. 110, no. 8, p. 083703, 2011.

[128] J. Wasscher, “Note on four-point resistivity measurements on anisotropic conductors,” *Philips Res Repts*, vol. 16, pp. 301–306, 1961.

[129] B. Logan, S. Rice, and R. Wick, “Series for computing current flow in a rectangular block,” *J. Appl. Phys.*, vol. 42, no. 7, pp. 2975–2980, 1971.

[130] R. H. Bube, *Photoconductivity of solids*. RE Krieger Pub. Co., 1978.

[131] R. H. Bube, *Photoelectronic properties of semiconductors*. Cambridge University Press, 1992.

[132] A. Rose, *Concepts in photoconductivity and allied problems*, no. 19. Interscience publishers, 1963.

[133] S. You *et al.*, “Band gap energy and valence band splitting of p-CdIn 2 Te 4 crystal by photocurrent spectroscopy,” *J. Appl. Phys.*, vol. 95, no. 8, pp. 4042–4045, 2004.

[134] G. Adriaenssens and N. Qamhieh, “The Gueorgi Nadjakov Lecture Negative-U defects in chalcogenide glasses: elusive or non-existent?,” *J. Mater. Sci. Mater. Electron.*, vol. 14, no. 10, pp. 605–609, 2003.

[135] N. Qamhieh, M. Benkhedir, M. Brinza, J. Willekens, and G. Adriaenssens, “Steady-state photoconductivity in amorphous selenium glasses,” *J. Phys. Condens. Matter*, vol. 16, no. 23, p. 3827, 2004.

[136] A. Rudenko and V. Arkhipov, “Drift and diffusion in materials with traps: III. Analysis of transient current and transit time characteristics,” *Philos. Mag. B*, vol. 45, no. 2, pp. 209–226, 1982.

[137] C. Main, R. Brüggemann, D. Webb, and S. Reynolds, “Determination of gap-state distributions in amorphous semiconductors from transient photocurrents using a fourier transform technique,” *Solid State Commun.*, vol. 83, no. 6, pp. 401–405, 1992.

[138] C. Main, “Interpretation of photocurrent transients in amorphous semiconductors,” *J. Non-Cryst. Solids*, vol. 299, pp. 525–530, 2002.

[139] M. K. Butt, H. M. Zeeshan, Y. Zhao, S. Wang, and K. Jin, "Controlling transport properties at LaFeO3/SrTiO3 interfaces by defect engineering," *J. Phys. Condens. Matter*, vol. 33, no. 24, p. 245001, 2021.

[140] D. V. Christensen *et al.*, "Stimulating Oxide Heterostructures: A Review on Controlling SrTiO3-Based Heterointerfaces with External Stimuli," *Adv. Mater. Interfaces*, vol. 6, no. 21, p. 1900772, 2019.

[141] P. Irvin *et al.*, "Rewritable nanoscale oxide photodetector," *Nat. Photonics*, vol. 4, no. 12, pp. 849–852, 2010.

[142] A. Tebano, E. Fabbri, D. Pergolesi, G. Balestrino, and E. Traversa, "Room-temperature giant persistent photoconductivity in SrTiO3/LaAlO3 heterostructures," *Acs Nano*, vol. 6, no. 2, pp. 1278–1283, 2012.

[143] M. Huijben, A. Brinkman, G. Koster, G. Rijnders, H. Hilgenkamp, and D. H. Blank, "Structure–property relation of SrTiO3/LaAlO3 interfaces," *Adv. Mater.*, vol. 21, no. 17, pp. 1665–1677, 2009.

[144] H. Yan, S. Wang, Z. Zhang, H. Zhang, C. Chen, and K. Jin, "Dynamic evolution of photogenerated carriers at complex oxide heterointerfaces," *J. Appl. Phys.*, vol. 124, no. 3, p. 035302, 2018.

[145] M. Ahmad, K. Rasool, M. A. Rafiq, and M. M. Hasan, "Enhanced and persistent photoconductivity in vertical silicon nanowires and ZnS nanoparticles hybrid devices," *Appl. Phys. Lett.*, vol. 101, no. 22, p. 223103, 2012.

[146] Y.-H. Ji *et al.*, "GaO x@ GaN Nanowire Arrays on Flexible Graphite Paper with Tunable Persistent Photoconductivity," *ACS Appl. Mater. Interfaces*, vol. 13, no. 35, pp. 41916–41925, 2021.

[147] M. I. Nathan, "Persistent photoconductivity in AlGaAs/GaAs modulation doped layers and field effect transistors: a review," *Solid-State Electron.*, vol. 29, no. 2, pp. 167–172, 1986.

[148] J. Carrasco *et al.*, "First-principles calculations of the atomic and electronic structure of F centers in the bulk and on the (001) surface of Sr Ti O 3," *Phys. Rev. B*, vol. 73, no. 6, p. 064106, 2006.

[149] V. Guduru *et al.*, "Optically excited multi-band conduction in LaAlO3/SrTiO3 heterostructures," *Appl. Phys. Lett.*, vol. 102, no. 5, p. 051604, 2013.

[150] H.-L. Lu *et al.*, "Photoelectrical properties of insulating LaAlO 3–SrTiO 3 interfaces," *Nanoscale*, vol. 6, no. 2, pp. 736–740, 2014.

[151] V. Aswin, P. Kumar, P. Pal, and A. Dogra, "Photo-resistive properties of LaAl 0.6 Cr 0.4 O 3/SrTiO 3 heterostructures: a comparative study with LaAlO 3/SrTiO 3," *Opt. Lett.*, vol. 41, no. 6, pp. 1134–1137, 2016.

[152] N. Y. Chan *et al.*, "Palladium nanoparticle enhanced giant photoresponse at LaAlO3/SrTiO3 two-dimensional electron gas heterostructures," *ACS Nano*, vol. 7, no. 10, pp. 8673–8679, 2013.

[153] A. Rastogi, J. Pulikkotil, and R. Budhani, "Enhanced persistent photoconductivity in δ-doped LaAlO 3/SrTiO 3 heterostructures," *Phys. Rev. B*, vol. 89, no. 12, p. 125127, 2014.

[154] G. Liu, R. Zhao, J. Qiu, Y. Jiang, and J. Gao, "Negative photoconductivity under visible light illumination in LaAlO3/SrTiO3 heterostructures," *J. Phys. Appl. Phys.*, vol. 52, no. 9, p. 095302, 2019.

[155] A. Rastogi and R. Budhani, "Solar blind photoconductivity in three-terminal devices of LaAlO 3/SrTiO 3 heterostructures," *Opt. Lett.*, vol. 37, no. 3, pp. 317–319, 2012.

Chapter 2

Experimental methods

2.1 Introduction

We have divided this chapter into two sections characterization techniques and measurement methods. In the first section, we have discussed different techniques such as Transmission Electron Microscopy (TEM), Infrared spectroscopy (IR), powder X-ray diffraction (XRD), Thermogravimetric analysis (TGA), UV-VIS-NIR spectroscopy used for the characterization of nanoparticles and nanofluids. In the second section, we explain the principle, fabrication, calibration, source of errors, and method of homemade transient hot wire thermal conductivity measurement setup based on the principle of resistance thermometer detection (RTD) to measure the thermal conductivity of the nanofluids. The details of the Van der Pauw and four-point probe measurement setup for electrical and photoconductivity measurement of PANI composites and oxide interfaces are given in this chapter, respectively.

2.2 Characterization methods

2.2.1 Powder X-ray diffraction (XRD)

The diffraction pattern of any crystalline material is like a fingerprint of that material. The X-ray diffraction pattern gives the information regarding crystal structure and phase purity of the material. The width of the peaks in the powder XRD pattern gives information about the average crystallite size of the nanomaterials.[1] The Scherrer equation is used to determine the average crystallite size of the nanomaterial from the broadening of the XRD peaks. The equation is

$$t = \frac{K\lambda}{\beta_F \, Cos\,(\theta)} \tag{2.1}$$

Where K is the shape parameter and it is 0.9 for the spherical-shaped particles[2], λ is the wavelength of X-rays, β_F is the full width at half maximum of the peak and θ is the Bragg's angle.

The XRD analysis of the synthesized samples were carried out using a Bruker D8 Advance X-ray diffractometer, Cu metal target K-α radiation having wavelength 1.5418 Å used as source. The XRD pattern of the sample were recorded with the scan rate of 2 degree/minute in the 2θ range 10-80 degrees. The XRD pattern of the sample were compared with the Joint Committee on Powder Diffraction Standards (JCPDS) data.

2.2.2 Transmission electron microscopy (TEM)

Transmission electron microscopy is a useful technique to determine the size, shape, distribution and the arrangement of the particle in the testing sample.[3] A beam of electrons produces enlarged image on a fluorescent screen or photographic film or CCD camera in this imaging technique. In our work a transmission electron microscope (JOEL JEM-2100) with a working accelerating voltage at 200 kV in the bright field mode is used to determine the microstructure, particle size and size distribution. The nanofluid samples for the TEM analysis were prepared in water (S1 and S3) and toluene (S4) by sonication and drop cast on a carbon-coated copper grid (200 mesh). In case of PANI composites, samples prepared in isopropanol for TEM analysis. The digital micrograph software supplied with the instrument was used to analyze the average particle size and distribution.

2.2.3 Infrared (IR) spectroscopy

Infrared spectroscopy (IR) is an analytical technique to determine the different functional groups and nature of bonding in the molecules under study.[4] The information about site and nature of attachment of surfactant molecules on to the surface of the magnetite nanoparticles is obtained using the IR spectroscopy technique. In our work, IR spectra of PANI samples,

oleic acid and citric acid coated magnetite nanoparticle were recorded using the using BrukerCary 600 series spectrometer from Agilent Technologies in the frequency range from 4000 cm^{-1} to 400 cm^{-1}. Background spectra was recorded using pure KBr cylindrical pellet. After that the test sample was mixed with the KBr and made a thin cylindrical pellet using pelletizer to perform the IR spectroscopy.

2.2.4 Thermogravimetric analysis (TGA)

Thermogravimetric analysis is a thermal analysis technique which track down the change in weight of the sample with increase in the temperature. The sample undergoes decomposition, vaporization, oxidation, sublimation, reduction etc. upon heating.[5] In this technique, a sample is heated in a required environment and the change in the weight of the sample measured efficiently as a function of the temperature. The variation in weight of the sample is plotted against the temperature and is called the thermogravimetric (TGA) curve. Further, the rate of change in the weight of the working sample can be plotted as a function of temperature and it is called thermogravimetric (DTG) curve. In the thesis work, Thermogravimetric analysis (TGA) of the surfactant coated iron oxide nanoparticles and PANI powder samples was carried out on the METTLER TOLLEDO thermogravimetric analyzer (model TGA/DSC-I) under the N_2 atmosphere. The weight loss was measured from room temperature to 800 ^{0}C with a heating rate of 10 ^{0}C per minute.

2.2.5 Optical study

The band gap of the samples was measured from optical spectroscopy (Agilent technologies) in the UV-VIS-NIR region using deuterium and halogen light source. The original spectra were measured in the transmission mode and further converted into absorption spectra. The tauc plot was used to calculate the band gap using the equation

$$\alpha(hv) = A(hv - E_g)^n \quad (2.1)$$

Where A, hv, E_g and α are the constant, photon energy, band gap, and absorption coefficient, respectively. The value of n indicated about nature of transition, n=1/2 corresponds to direct allowed transition and n = 2 corresponds to indirect allowed transition.

2.3 Measurement methods

2.3.1 Transient Hot Wire (THW) method

At present, various measurement methods have been developed and used for the thermal conductivity measurement of fluids. These measurement methods are mainly divided into steady state techniques and transient state techniques as discussed in the previous chapter. Transient measurement techniques included the 3-Omega technique, Transient hot-wire technique (THW), Thermal comparator technique, Transient plane source, etc. The design and the construction of the transient techniques are quite complex but still transient state techniques gaining a lot of importance because these methods used unsteady state solutions to measure the thermal properties. Among all the transient techniques, the transient hot wire technique is well established and is widely used for the thermal conductivity measurement of gases, liquids, nanofluids, and solids. The popularity of this technique is because of its simple construction, variety in applications, and low uncertainty as well as high measurement accuracy. The uncertainty of this measurement technique for gases, liquid and solid is below 1% but for nanofluids and melts it is below 2%. This technique can be successfully applied to a long range of temperatures and pressure to measure thermal properties.

At first, Stâlhane and Pyk [6] used this technique to measure the thermal conductivity of the powder samples and solids. In literature, both are considered the pioneer of this measurement technique. Harman et al.[7] further modify the theoretical model used in the thermal conductivity measurement of the gases. Stâlhane [6] and Haarman's [7] work is of great importance in the development of the transient hot wire method. At that time, it was not possible to measure the thermal conductivity of the electrically conducting fluid because a thin bare metallic wire was used as a heater as well as a temperature sensor in the technique. It was only possible to measure the thermal conductivity of the non-conducting fluids.

Nagasaka and Nagashima [8] modified this technique to measure the thermal conductivity of the electrical conducting samples with the coating of insulating material (polyester) on the bare metal wire. After that, they successfully used this measurement technique for thermal conductivity measurement of an aqueous NaCl solution in the temperature range of 0-45 ^{0}C at atmospheric pressure with an accuracy of 0.5%. Alloush et al.[9] also suggested that tantalum wire can be used to measure the thermal conductivity of the electric conducting fluids because after oxidation it forms a thin insulation layer of tantalum pentaoxide. Sung Wook Hong et al.[10] used the same measurement technique to measure the thermal conductivity of ethylene glycol based ZnO nanofluids with 1.06 vol%. They found enhancement in the effective thermal conductivity with 0.53 precision error. They also investigated the proper measurement time range (1.2 to 3.2s) for the fluids. J. P. Garnier et al.[11] proposed a transient short hot wire method for highly corrosive and conducting concentrated nitric acid samples. They used 15mm long anodized thin tantalum wire for measurement. The estimated uncertainty in this measurement was less than 5%.

Yu and Choi [12] reported that the insulation on the metallic wire would not affect the thermal conductivity measurement result even if the coating thickness same as the thickness of the wire. They also investigated that there is no correction term corresponding to the insulation in the formulation and the thermal conductivity of the insulated coating is less than the working fluid. They also included that the error due to the insulation coating compared to the ideal continuous line source results is 0.8% for the measurement time of 0.5s. Lee et al.[13] made the suspension of Al_2O_3 and CuO nanoparticles in water and ethylene glycol and measured the thermal conductivity of four oxide nanofluids using this technique. After that researchers start using this technique successfully to measure the thermal conductivity of different types of nanofluids [14], [15], nanocomposite[16], and aqueous solution.[17]

2.3.1.1 Theory

The THW method was modeled based on an infinitely long and thin continuous line source suspended vertically in the infinite homogeneous medium. When current passes through this infinite line source at time t >0, a constant heat flux q per unit length per unit time is produced in the wire. This heat in the line source is lost to the surrounding fluid and the temperature of the fluid rises with time. The line source loses the heat according to the thermal conductivity

of the surrounding fluid. The thermal conductivity and thermal diffusivity of the fluid are denoted as k and α_D respectively. As in this model, the line source has been taken infinite and zero radius, so the line source should have infinite thermal conductivity and zero heat dissipation. The mathematical model of the THW method has been fully developed by various researchers such as Carslaw et al.[18], Healy et al.[19], and Harman et al.[7], by a successive correction in this model. The conduction in the infinite continuous line source is considered one-dimensional heat conduction which can be expressed as given below:

$$\frac{1}{\mathrm{r}}\frac{\partial}{\partial \mathrm{r}}\left(\mathrm{r}\frac{\partial \mathrm{T}}{\partial \mathrm{r}}\right) = \frac{1}{\alpha_D}\left(\frac{\partial \mathrm{T}}{\partial \mathrm{t}}\right) \tag{2.2}$$

There are two boundary conditions to solve the above equation. Boundary conditions are given as

$$t = 0, r = 0 \qquad \lim_{r\to 0} r\frac{\partial T}{\partial r} = \frac{-q}{2\pi k} \tag{2.3}$$

$$t \geq 0, r = \infty \qquad \lim_{r\to \infty}\{\Delta T(r,t)\} = 0 \tag{2.4}$$

Where q is the heat flux, $\Delta T = T - T_0$, T is the temperature of the wire at any time during the heating process an T_0 is temperature at the initial time before the start of measurement. [20].

The analytical solution of the first equation using the given boundary conditions

$$\Delta T(r,t) = T(r,t) - T_0 = \frac{-q}{2\pi k} E_f\left\{\frac{-r^2}{4\alpha_D t}\right\} \tag{2.5}$$

Where E_f is the exponential integral function which is given as

$$E_f\left\{\frac{r^2}{4\alpha_D t}\right\} = \int_{\frac{r^2}{4\alpha_D t}}^{\infty} \frac{e^{-x}}{x} dx \tag{2.6}$$

Now the solution of the equation can be expressed as

$$\Delta T(r,t) = \frac{q}{4\pi k}\left\{-\beta + ln\left(\frac{4\alpha_D t}{r^2}\right)\right\} \quad (2.7)$$

Where β is the Euler's constant. The value of Euler's constant is 0.5772.

The initial and final time equation can be written as

$$\Delta T_1(r,t_1) = \frac{q}{4\pi k}\left\{-\beta + ln\left(\frac{4\alpha_D t_1}{r^2}\right)\right\} \quad (2.8)$$

$$\Delta T_2(r,t_2) = \frac{q}{4\pi k}\left\{-\beta + ln\left(\frac{4\alpha_D t_2}{r^2}\right)\right\} \quad (2.9)$$

Then the difference between the two-time equation is given as the change in the Temperature. Thus, the differential equation becomes as

$$\Delta T_2(r,t) - \Delta T_1(r,t) = \frac{q}{4\pi k}\left(\frac{t_2}{t_1}\right) \quad (2.10)$$

From this equation plot the temperature difference versus the logarithm time. After that the slope of the line taken which almost straight on the selected valid region between time t_1 (t_{min})and t_2 (t_{max}). From this, the thermal conductivity of the fluid can be calculated as

$$k = \frac{q}{4\pi}\frac{d(lnt)}{d(\Delta T)} \quad (2.11)$$

Babu et al.[20] re-expanding the above equation and obtained the thermal diffusivity from the same equation. The above equation can be written as follow after expanding

$$\Delta T = \frac{q}{4\pi k} ln\left(\frac{4\alpha_D}{r^2}\right) e^{-\gamma} + \frac{q}{4\pi k} ln(t) \quad (2.12)$$

From this equation, the slope and intercept used to determine the thermal conductivity and thermal diffusivity of the testing fluid, respectively. This equation is considered in our work for the thermal conductivity measurement of the nanofluids.

2.3.1.2 Experimental setup and their details

The principle of the Transient hot wire method depends on resistance temperature detection (RTD). This means that the resistance of the metallic wire changes with the temperature .[21], [22] The change in the resistance can be used to calculate the change in the temperature using the equation

$$R = R_0(1 + \beta \Delta T) \tag{2.13}$$

Where R and R_0 are the resistance of the conductive thin metallic wire at any temperature T and 0 ^{0}C respectively.

A transient hot wire system simply involves a thin metallic wire suspended symmetrically in the working fluid in the cylindrical vertical container. This thin metallic wire not only acts as a line source but at the same time acts as a temperature resistance thermometer. As a line source, it creates uniform heat flux per unit length in the working medium that is constant in time. From the joule heating effect, the temperature of thin metallic wire increases with the time after applying a constant current to the wire. This further increases the temperature field throughout the working fluid or substance. The thermal conductivity of the medium is acquired from the time evolution of the voltage or temperature of the wire. To neglect the end effect from the measurement results, researchers used two identical wires in all aspects except their length. Both wires at the same time were used to extract the time evolution of the temperature of the wire in the medium. At present, a huge advancement in the field of electronics makes it possible to take up to 1000 measurements of the transient voltage or temperature rise at a constant current supply in less than 1 second. This decreases the measurement time which further reduced the error in the measurement by the convection especially in the liquids and nanofluids as working medium. The convection effect in the measurement of thermal conductivity can be easily identified by plotting ΔT vs ln(t). The deviation of the plot from linearity is the indication of the convection effect in the measurement data (Hammerschmidt and Sabuga 2000).[23] The success of this technique rests upon the fact that by the proper choice of the design parameters it is possible to minimize departures from the infinite line source model.

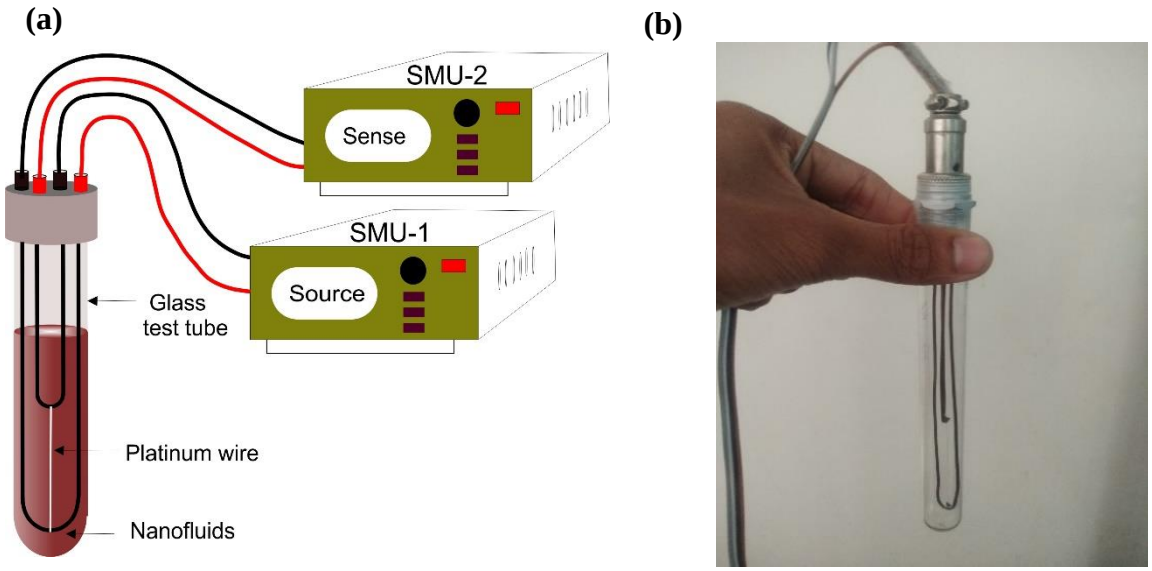

Figure 2.1: (a) Schematic figure, and (b) real image of the THW measurement setup in our lab

We made a thermal conductivity measurement setup in our lab based on the RTD principle as shown in the Figure 2.1. We have used a thin platinum wire with a length of 5 cm and a diameter of 50 μm. We have chosen platinum wire because it has a high-temperature coefficient of resistance and also showed a linear variation of resistance over a wide range of temperatures. These properties of the platinum wire make it an ideal material for thermal conductivity measurement. Next, we used copper wire to make four connections with the platinum wire. The diameter of this copper wire is 1 mm. We choose thick copper wire to make the connection because it makes it easy to withstand 50 μm platinum wire in the setup. All the connections were made by convention soldering technique using tin/lead (60/40) soldering wire. We choose a 15 ml glass test tube for containing the working fluid or nanofluid to measure the thermal conductivity. Here, we used the four-wire method resistance measurement method which is the most precise method to measure the resistance. As shown in the Figure 2.1 (a), two wires are used to source the current through the wire and the other two for measuring the resistance or voltage across the wire with time. We have used Keithley Source Measurement Unit (SMU) 2450 for the source as well as sense the signal. We can easily measure the change in temperature of the wire with the application of the source without any convection effect. Therefore, we choose measurement time 12s for the thermal conductivity measurement of various fluids and nanofluids.

2.3.1.3 Calibration of the measurement setup

The calibration of the transient hot wire method had been done using distilled water and Toluene as test fluid. All the measurement had been done at room temperature. Each experiment was repeated 5 to 6 times to reduce the measurement error in the thermal conductivity value. This also gave the reproducibility of the measurement instrument. First, we conducted the measurement for the distilled water at room temperature. For we took 12 ml of water in the test tube and put the hot wire sensor immersed fully inside the water.

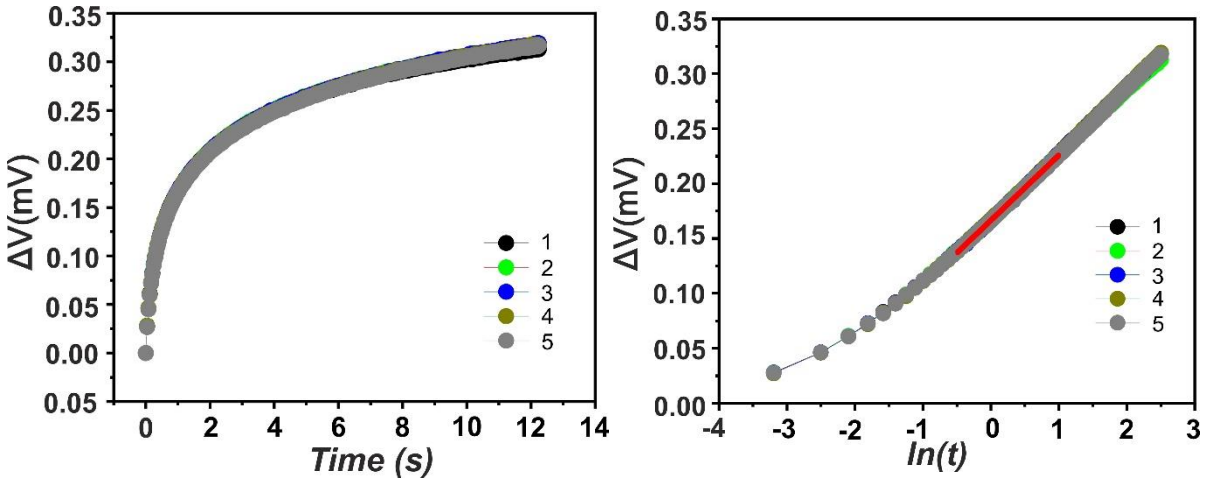

Figure 2.2: (a) The variation of the voltage across the platinum wire inside the water with the change in time (b) The plot of voltage vs ln(t) for at room temperature for distilled water.

After that, we waited for 15 minutes so that convection caused due to disturbance becomes negligible. Because this convection is the major source of error in the measurement so it is necessary to keep the system undisturbed for at least 15 minutes. During this time, the wire comes into equilibrium with the surrounding water. We have connected all four wires to the SMU 2450 for the current source and voltage measurement. Here, we used SMU 2450 because it has a precision of 0.1 % in the current source for the current range of 0-100mA. In the case of voltage measurement, this SMU has a resolution of 1 μV and the precision was 25 ppm for the measurement in the range of 0-10 V. The high precision and resolution of the SMU allow accurate measurement of the change in resistance without the need for a Wheatstone bridge circuit.

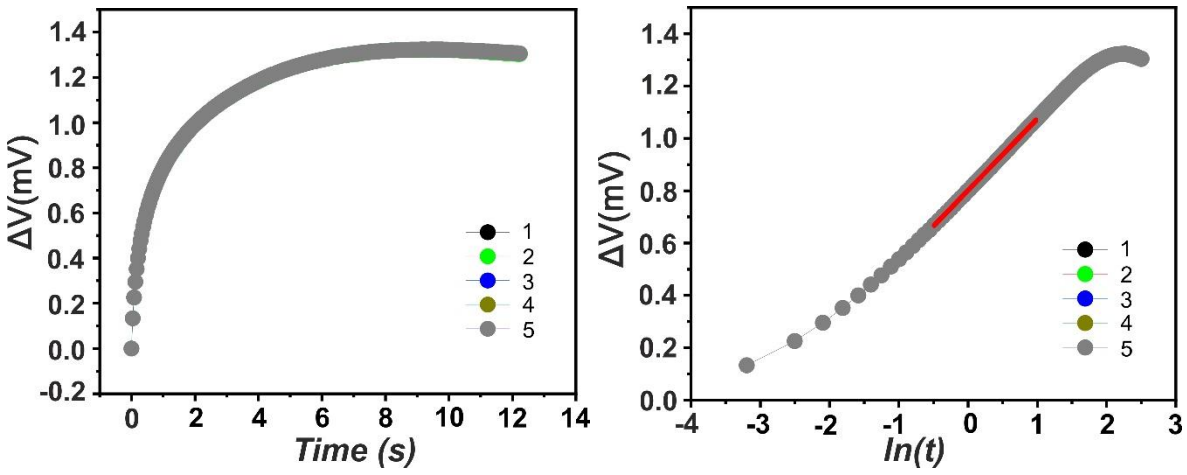

Figure 2.3: (a) The variation of the voltage across the platinum wire inside the water with the change in the time for toluene (b) The plot of voltage vs ln(t) for toluene at room temperature

After that, we applied a constant 100 mA current to the hot wire sensor using Keithley SMU 2450 and simultaneously we measured the change in the voltage across the metallic wire. The measurement time, in this case, was 12 s. Figure 2.2(a) shows the variation of the voltage across the wire with the time at room temperature. After that, we plotted the graph between voltage difference versus logarithmic time (see Figure 2.2(b)). The graph showed some non-linearity in starting time of the measurement and after 3s, non-linearity in the starting time because the heat flux on the surface of the wire takes some time to reach a steady state. The non-linearity after 5s in the graph indicates that the convection effect comes in the fluid. So, the data taken after this time was not included in the measurement. The choice of the proper data range in the graph becomes important. After selecting the proper time range, the slope of the voltage difference vs logarithmic time was obtained by a linear curve fitting as shown in the Figure 2.2(b). The slope of the graph was further used for the thermal conductivity measurement of the water. We used the modified formula for the thermal conductivity of the test fluids which is given as

$$k = \frac{q\beta V_0}{4\pi}\frac{d(lnt)}{d(\Delta V)} \tag{2.14}$$

Where

$$slope = \frac{d(lnt)}{d(\Delta V)} \tag{2.15}$$

$$q = \frac{(V_0)^2}{L_w R_w} \tag{2.16}$$

and

$$\Delta V = V - V_0 \tag{2.17}$$

where q is the heat flux from the hot wire surface, V is the voltage across the wire at time t and V_0 is the potential at time t = 0, L_w is the length of the wire used in the instrument. R_w is the resistance of the wire and β (0.00392 C^{-1}) is the temperature coefficient of resistance of the platinum wire. We found the thermal conductivity value of the water 0.601 W/mK which is in quite close agreement with the reported value of the thermal conductivity of distilled water . The uncertainty in the measurement was 1.8 % and the accuracy was 99.7 %. Similarly, we measured the thermal conductivity of the non-polar solvent toluene. The measurement time, in this case, is 12 seconds. We can observe from non-linearity that the convection in the fluids in the system comes earlier as compared to the water case (see Figure 2.3 (b)). We found thermal conductivity value of toluene was 0.130 W/mK at room temperature. The accuracy and uncertainty in the measurement were 99.65 % and 1.0% respectively. The thermal conductivity values measured by this instrument were quite accurate so this instrument can be used to measure the thermal conductivity of other unknown fluids and nanofluids.

2.3.1.4 Source of error and its correction

De Groot et al.[24] listed the possible source of errors in the transient hot wire method. They found that the finite parameters of the hot wire measurement instruments are the major source of errors. In the mathematical model, all these parameters are either zero or infinite, so this leads to the error in the measurement results. The possible source of deviation of the assumed 1D-line source mathematical model and the actual instrument should be taken into the account. These errors are mainly due to the finite heat capacity of the metal wire, finite wire thickness, and finite outer diameter of the container. We have discussed the source of error and their corrections in the next section.

In the mathematical model the wire has been taken as a 1D- infinite line source, having zero thickness, infinite thermal conductivity, and zero heat capacity. But in a real situation, it is not possible to use a material having zero heat capacity. Healy et al.[19] considered finite radius a, finite thermal conductivity k_w, and finite heat capacity $(\rho c_p)_w$ per unit volume. These finite conditions produce two Fourier equations one for the wire and the other one for the fluid. The condition is that the temperature and heat flux must be continuous between two regions at r = a. For metallic wire, they solved the equation

$$(\rho c_p)_w \frac{\partial T_w}{\partial t} = k_w \nabla^2 T_w - \frac{q}{\pi a^2} \; ; \; 0 \leq r \leq a \tag{2.18}$$

The resistance of the wire corresponds to its temperature at any instant of the time. The actual temperature measured would be the integral average of the $\Delta T_w(r,t)$ so that they found the solution of the equation with new boundary conditions they got the solution like

$$\Delta T_w(t) = \frac{q}{4\pi\lambda}\left\{\left[1 - a^2 \frac{((\rho c_p)_w - \rho c_p)}{2\lambda t}\right] ln\left(\frac{4kt}{a^2 C}\right) + \frac{a^2}{2kt} - \frac{a^2}{4k_w\, t} + \frac{\lambda}{2\lambda_w}\right\} \tag{2.19}$$

Here in the above equation, the major correction is due to the finite heat capacity of the wire. So δT_1 can be written as [19]

$$\delta T_1 = \frac{q}{4\pi\lambda}\left[a^2 \frac{((\rho c_p)_w - \rho c_p)}{2\lambda t}\right] ln\left(\frac{4\alpha_D t}{a^2 C}\right) \tag{2.20}$$

where c is a constant value of 1.781, we plotted the variation of this correction factor δT_1 as a function of the time to specify the heat capacity of the wire effect as shown in the Figure 2.4 (a). We found that δT_1 decreased with increasing time and becomes zero at a time above 5s. The value of δT_1 for the water case was the order of 10^{-3} to 10^{-4} K which is very small as compared to the temperature variation in the experiment which was (1-2 K). So, this correction can be ignored in our case.

The second major correction is due to the finite wire thickness, the wires employed for the THW method in literature lie in the range between 20 μm to 500 μm.[25] Tertsinidou et al.[26] mentioned that the thick wire can lead to significant errors in the measurement due to deviation

from the 1-D ideal line source theory. A sufficiently thin wire has been suggested to reduce all corrections to a level where the first-order theory for correction is sufficient and necessary. The truncation error for apply the first order approximation can be expressed as

$$\frac{\delta T_2}{\Delta T} = \frac{a^2}{4\alpha_D t\, ln\left(\frac{4\alpha_D t}{a^2 C}\right)} \tag{2.15}$$

The plot of the truncation error due to the finite thickness of the wire is shown in the Fig. 2.4 (b)**.** The truncation error value ($\delta T_2/\Delta T$) decreases with increasing time and approaches zero at the time of more than 5 seconds as in the case of the finite heat capacity correction. Thus, this correction term is also not considered in the measurement.

Now for the third case of the finite boundary condition of the liquid container, several investigators work on this correction term and got that if the term $\delta T_3 = R^2/(\alpha_D t)$ is equal to or more than 5.78, then the boundary condition correction term can be ignored in the system. Where R is the radius of the test tube used as a container in our study which is equal to 0.01 m, α_D = 1.43*10^{-7} m^2/s is the thermal diffusivity of the water and t is the time. The value of the $R^2/(\alpha_D t)$ for the water for the time 5 s is 140 which is very large as compared to 5.78 so the correction due to finite boundary conditions can be ignored in our case.

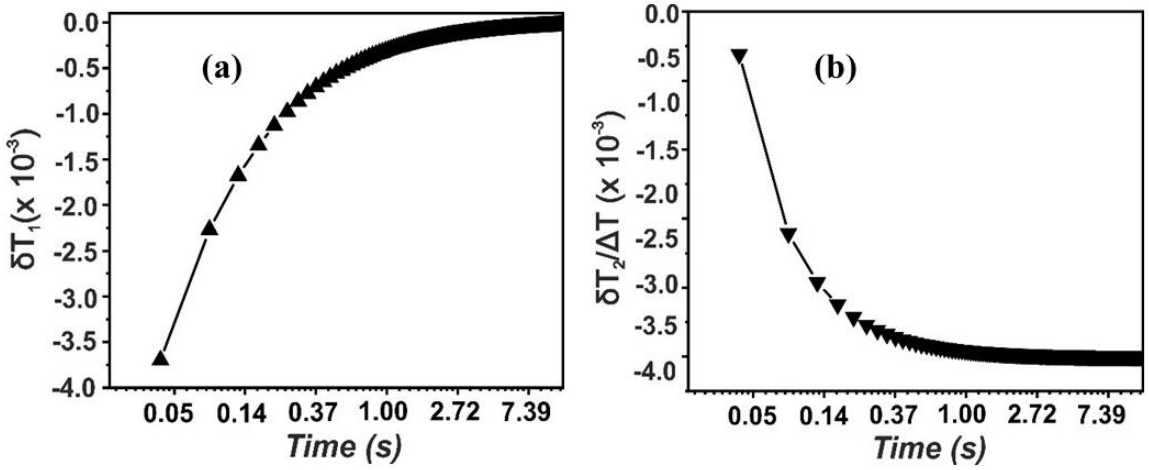

Figure 2.4: (a) The correction term (δT_1) due to finite heat capacity of the platinum wire as a function of time (b) The correction term ($\delta T_1/\Delta T$) due to finite thickness of wire as a function of time for distilled water as test fluid.

2.3.2 Van der Pauw (VdP) method

2.3.2.1 Electrical conductivity measurement setup and details

Electrical conductivity measurements are carried out inside the cryogenic four-probe station. The micro-manipulated probe station being used here is JANIS Research (VPF-800 Cryostat), equipped with 4 micro-manipulated probes with three degrees of freedom, a temperature controller (Lakeshore model 335), and a turbo pump (Edwards T-station75). The schematic and the real picture of the probe station are shown in the Figure 2.5 and Figure 2.6 respectively. This probe station is a temperature variable system that enables the temperature to be accurately controlled at any point between 78 K and 800K. The temperature is monitored by the temperature controller equipped with two E-type thermocouple temperature sensors; one is mounted on the sample mount and the other is located on the sample holder. The temperature controller provides an equilibrium between the liquid nitrogen and the input heater power to achieve a stable set point of temperature adjusted by the user. The thermal impedance displacer (TID) at the bottom of the steel rod plays an important role to regulate the flow of liquid nitrogen to the sample mount. TID acts as an insulating barrier between the liquid nitrogen and

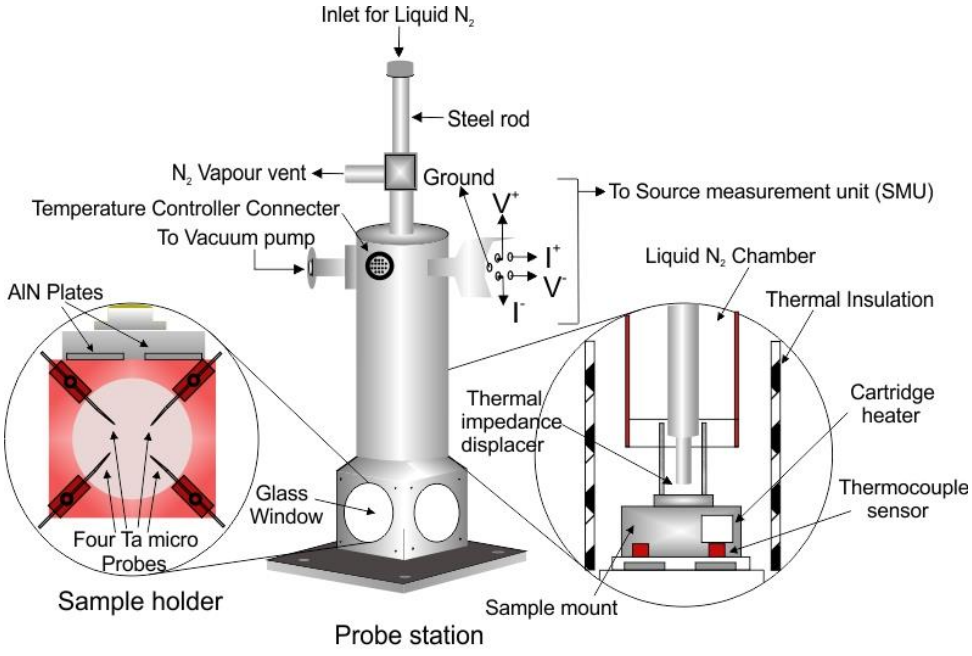

Figure 2.5: Schematic diagram of JANIS cryogenic probe station.

the sample mount. All four probes are electrically isolated from the sample mount using AIN plates. These AIN plates have excellent thermal properties while isolating the probes from the sample mount. The cartridge heater and E-type thermocouple sensors are placed on the sample providing the temperature control of samples during measurement. Liquid nitrogen is used to achieve low temperatures during the measurement. The liquid nitrogen chamber was filled through the inlet at the top of the steel rod using a funnel that came with the system. The pumping system creates a vacuum level of $2*10^{-2}$ Torr to evacuate all the water vapours present around the sample before bringing it below room temperature.

The sample obtained in the powder form was used to make the cylindrical pellet of diameter 10 mm by pressing the powder in a hydraulic press. The prepared cylindrical pellet was used to investigate the electrical conductivity of the sample. Four Cr/Au (15 nm/100nm) circular contacts of diameter 1 mm were made on the circumference of the pellet using the EXCEL e-beam deposition process. These four contacts on the pellets were made according to the Van der Pauw configuration as shown in Figure 2.7(a). The diameter of the pellet and gold (Au) electrode was 10 mm and 1 mm respectively. The experimental setup consisted of Keithley Source Measurement Unit (SMU)- 2450 for current and voltage measurement in two different

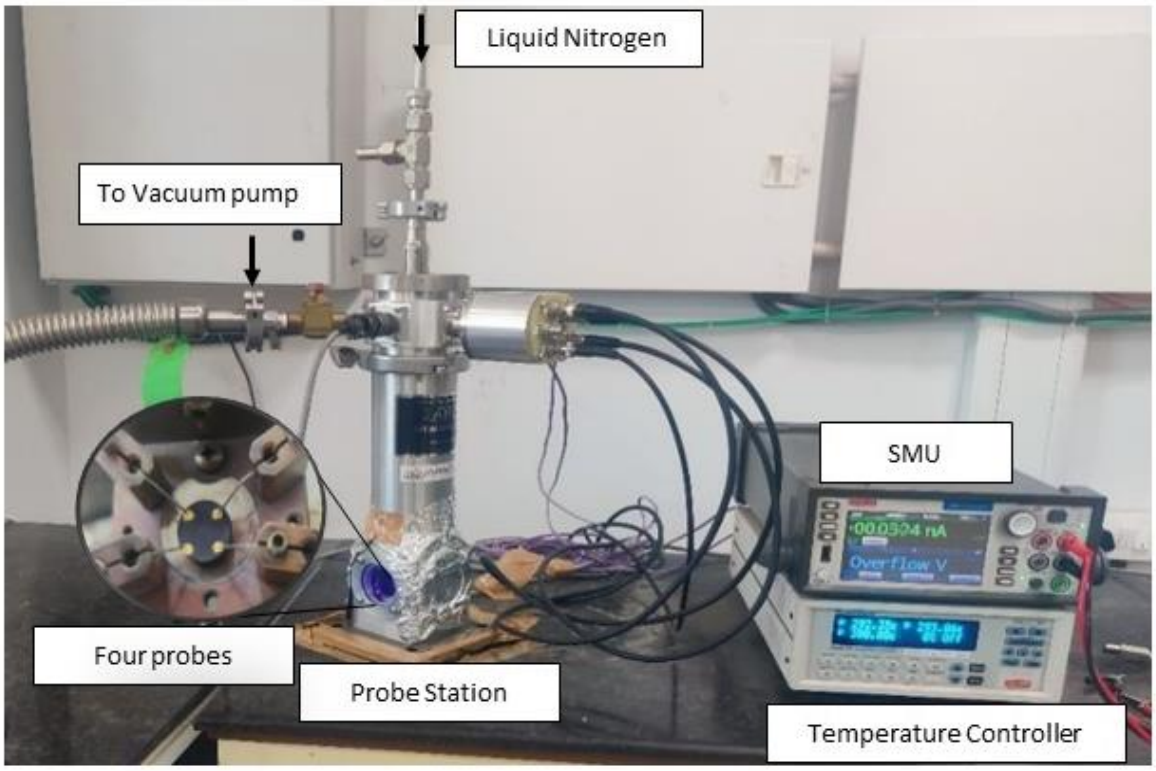

Figure 2.6: The real picture of the electrical conductivity measurement setup in our lab

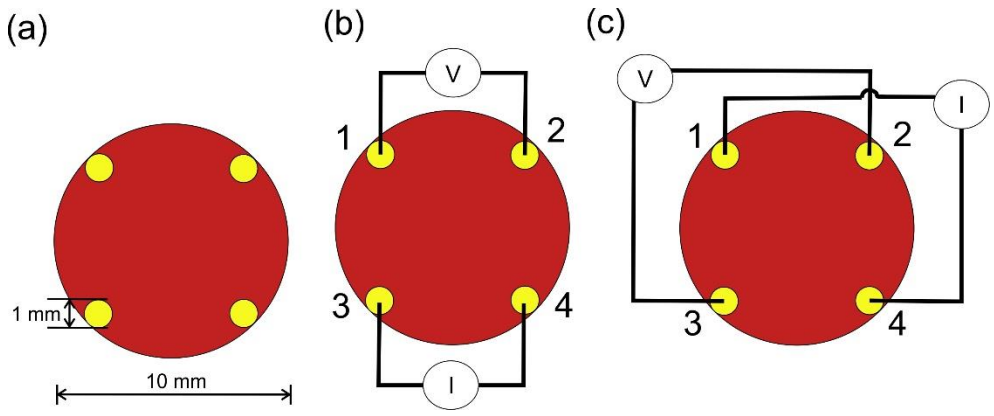

Figure 2.7: (a) The schematic of cylindrical pellet with Au electrodes for resistivity measurement. (b) and (c) Two different configurations were used for the resistivity measurement of the material.

configuration as shown in Figure 2.7 (b and c). All four probes are made of tungsten having an overall length of 35.5 mm and a point radius of 0.5 microns. These probes are connected to the SMU through BNC for four probe IV measurements.

2.3.3 Four-point probe method

2.3.3.1 Photoconductivity measurement setup and details

We have used a similar experimental measurement set up with two DPSS lasers having wavelengths 405 nm (Blue) and 532 nm (Green) with variable intensity to investigate the effect of light illumination on the transport properties of the 2DEG at the interface of oxide heterostructure. A schematic diagram of the photoconductivity measurement setup is shown in Figure 2.8. The VPF-800 cryostat has a window block to allow optical access to the sample. We have used one glass window to shine laser light with a spot radius of 1.34 mm on the different samples at different temperatures from 76K to 300K with varying power from 0 to 80 mW. A real picture of the measurement setup established in our lab is given in Figure 2.9. The working sample was placed at the center of a square-shaped glass slide with four isolated gold pads for the wire bond connection at the interface of the oxide heterostructure as shown in the zoom part of Figure 2.9. All four microprobes were placed on the four isolated gold pads ((2mm x 2mm) for the necessary sheet resistance measurement. These four isolated gold pads (Cr/Au) were made on the glass slide using the hard mask through the e-beam deposition technique. All

the electrical measurement has been done using the Keithley SMU-2450. The ultrasonic wire bonder with Al wire was used to make various electrical connections. The distance of the laser from the sample was 40 cm and it was kept constant during all the measurements. A power meter (Thorlabs) was used to measure the power of the laser light at a distance of 40 cm from the source. Liquid nitrogen and a temperature controller were used to achieve a stable set point of temperature for the measurement.

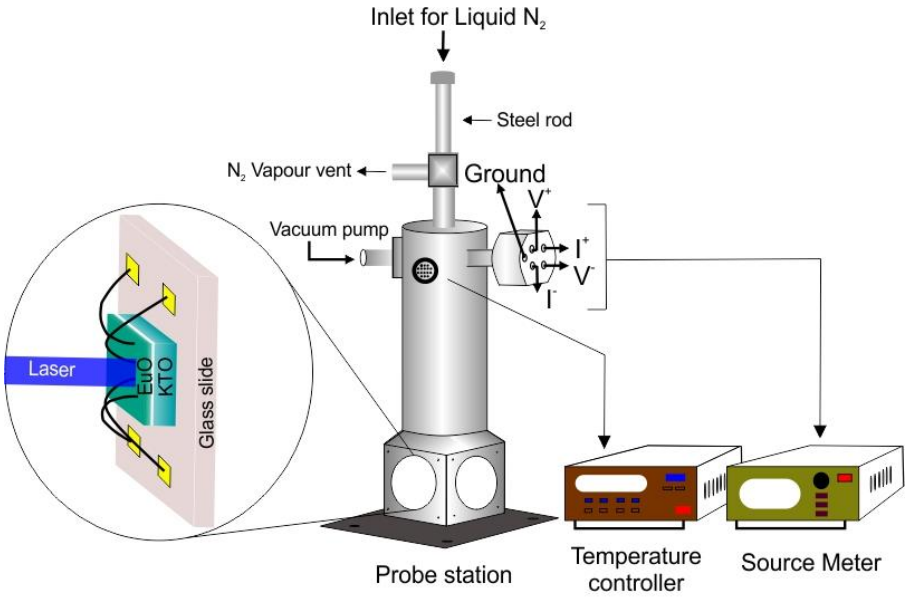

Figure 2.8: The graphical schematic of the apparatus used for the photoconductivity measurement

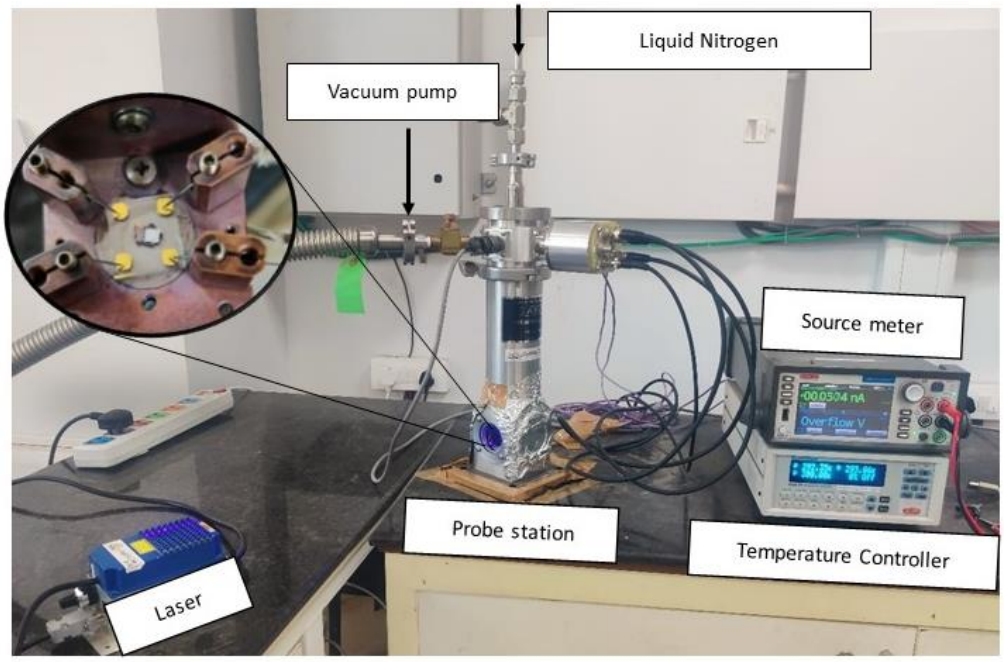

Figure 2.9: A real picture of photoconductivity measurement setup in our lab

References:

[1] B. D. Cullity, *Elements of X-ray Diffraction*. Addison-Wesley Publishing, 1956.

[2] A. Patterson, "The Scherrer formula for X-ray particle size determination," *Phys. Rev.*, vol. 56, no. 10, p. 978, 1939.

[3] D. B. Williams and C. B. Carter, *Transmission Electron Microscopy: Spectrometry David B. Williams and C. Barry Cart. IV*. Plenum, 1996.

[4] R. M. Silverstein and G. C. Bassler, "Spectrometric identification of organic compounds," *J. Chem. Educ.*, vol. 39, no. 11, p. 546, 1962.

[5] D. Skoog, F. J. Holler, and S. Crouch, "Principles of instrumental analysis. thomson brooks," *Cole Can.*, 2007.

[6] B. Stalhane and S. Pyk, "New method for determining the coefficients of thermal conductivity," *Tek Tidskr*, vol. 61, no. 28, pp. 389–393, 1931.

[7] T. C. Harman, J. Cahn, and M. Logan, "Measurement of thermal conductivity by utilization of the Peltier effect," *J. Appl. Phys.*, vol. 30, no. 9, pp. 1351–1359, 1959.

[8] Y. Nagasaka and A. Nagashima, "Absolute measurement of the thermal conductivity of electrically conducting liquids by the transient hot-wire method," *J. Phys. [E]*, vol. 14, no. 12, p. 1435, 1981.

[9] A. Alloush, W. Gosney, and W. Wakeham, "A transient hot-wire instrument for thermal conductivity measurements in electrically conducting liquids at elevated temperatures," *Int. J. Thermophys.*, vol. 3, no. 3, pp. 225–235, 1982.

[10] S. W. Hong, Y.-T. Kang, C. Kleinstreuer, and J. Koo, "Impact analysis of natural convection on thermal conductivity measurements of nanofluids using the transient hot-wire method," *Int. J. Heat Mass Transf.*, vol. 54, no. 15–16, pp. 3448–3456, 2011.

[11] J. P. Garnier, J. Gallier, B. Mercx, P. Dudoignon, and D. Milcent, "Thermal conductivity measurement in clay dominant consolidated material by Transient Hot-Wire method.," 2010, vol. 6, p. 38001.

[12] W. Yu and S. U.-S. Choi, "Influence of insulation coating on thermal conductivity measurement by transient hot-wire method," *Rev. Sci. Instrum.*, vol. 77, no. 7, p. 076102, 2006.

[13] S. Lee, S.-S. Choi, S. Li and, and J. Eastman, "Measuring thermal conductivity of fluids containing oxide nanoparticles," 1999.

[14] D. Cabaleiro, J. Nimo, M. Pastoriza-Gallego, M. Piñeiro, J. Legido, and L. Lugo, "Thermal conductivity of dry anatase and rutile nano-powders and ethylene and propylene glycol-based TiO2 nanofluids," *J. Chem. Thermodyn.*, vol. 83, pp. 67–76, 2015.

[15] B. Gu, B. Hou, Z. Lu, Z. Wang, and S. Chen, "Thermal conductivity of nanofluids containing high aspect ratio fillers," *Int. J. Heat Mass Transf.*, vol. 64, pp. 108–114, 2013.

[16] J. Bouchard, A. Cayla, E. Devaux, and C. Campagne, "Electrical and thermal conductivities of multiwalled carbon nanotubes-reinforced high performance polymer nanocomposites," *Compos. Sci. Technol.*, vol. 86, pp. 177–184, 2013.

[17] K. Fujiura, Y. Nakamoto, Y. Taguchi, R. Ohmura, and Y. Nagasaka, "Thermal conductivity measurements of semiclathrate hydrates and aqueous solutions of tetrabutylammonium bromide (TBAB) and tetrabutylammonium chloride (TBAC) by the transient hot-wire using parylene-coated probe," *Fluid Phase Equilibria*, vol. 413, pp. 129–136, 2016.

[18] H. S. Carslaw and J. C. Jaeger, *Conduction of heat in solids*. 1959.

[19] J. Healy, J. De Groot, and J. Kestin, "The theory of the transient hot-wire method for measuring thermal conductivity," *Phys. B C*, vol. 82, no. 2, pp. 392–408, 1976.

[20] S. K. Babu, K. Praveen, B. Raja, and P. Damodharan, "Measurement of thermal conductivity of fluid using single and dual wire transient techniques," *Measurement*, vol. 46, no. 8, pp. 2746–2752, 2013.

[21] L. Michalski, K. Eckersdorf, J. Kucharski, and J. McGhee, *Temperature measurement*. John Wiley & Sons, 2001.

[22] S. Sen, T. Pan, and P. Ghosal, "An improved lead wire compensation technique for conventional four wire resistance temperature detectors (RTDs)," *Measurement*, vol. 44, no. 5, pp. 842–846, 2011.

[23] U. Hammerschmidt and W. Sabuga, "Transient hot wire (THW) method: uncertainty assessment," *Int. J. Thermophys.*, vol. 21, no. 6, pp. 1255–1278, 2000.

[24] J. De Groot, J. Kestin, and H. Sookiazian, "Instrument to measure the thermal conductivity of gases," *Physica*, vol. 75, no. 3, pp. 454–482, 1974.

[25] A. Kazemi-Beydokhti, S. Z. Heris, N. Moghadam, M. Shariati-Niasar, and A. Hamidi, "Experimental investigation of parameters affecting nanofluid effective thermal conductivity," *Chem. Eng. Commun.*, vol. 201, no. 5, pp. 593–611, 2014.

[26] G. Tertsinidou, M. J. Assael, and W. A. Wakeham, "The apparent thermal conductivity of liquids containing solid particles of nanometer dimensions: a critique," *Int. J. Thermophys.*, vol. 36, no. 7, pp. 1367–1395, 2015.

Chapter 3

Thermal conductivity measurement of iron oxide nanofluids and cellulose nanocomposites

3.1 Introduction

Nanofluids have diverse applications in thermal management, thermal insulation, and thermal exchange. Recently, they have also gained tremendous attention for biological and clinical applications, where heat transfer plays a critical role. In hyperthermia applications of magnetic nanoparticles, understanding the heat exchange mechanism between nanoparticles and tissues is important for clinical applications and the heat transfer mechanism also holds the key for drug delivery applications using nanoparticles. Therefore the understanding of thermal conductivity in nanoparticles will lead to the design of many applications and the development of the technology. The thermal conductivity of Fe_3O_4 nanofluids has been reported by several groups; [1] however, there is a lack of systematic understanding of the heat transfer mechanism of the thermal conductivity of nanofluids. The deterioration of the thermal conductivity can be explained on the basis of the combined effect of interfacial thermal resistance and the presence of a charged surfactant layer on the magnetite nanoparticles (see Figure 3.1(a)– (c)). The schematic shows the surfactant coating configuration for different wt% and types of surfactants. Figure 3.1(a) and (b) show the citric acid coated (polar particle) and Figure 3.1(c) shows the oleic acid coated (apolar particle). The suspension stability of nanofluids is directly affected by the surface charge and surfactant coating. [2], [3] Two types of surface resistance are shown in Figure 3.1(a)–(c), where k_{sf} is the surface resistance between the surfactant and fluid layer, and k_{ps} is the surface resistance between the nanoparticle and surfactant. These two

determine the total surface conductance (G) of the nanoparticle and have a dominant role in deciding the heat transfer rate through the nanofluid.

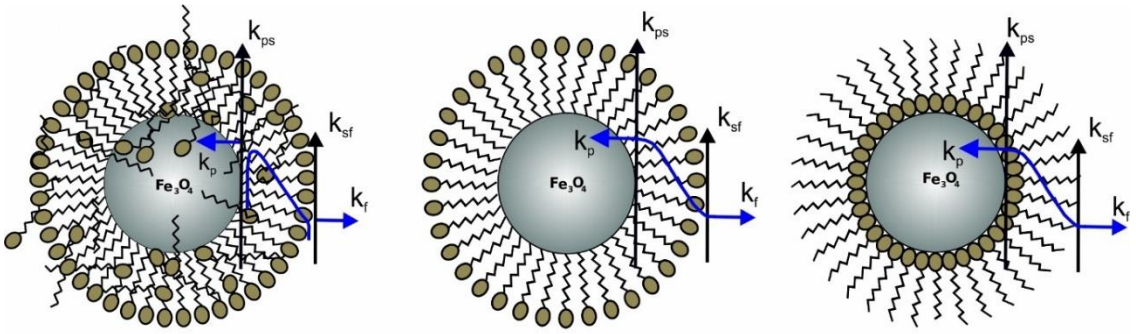

Figure 3.1: The schematic of the behavior of thermal conductivity at the interface of nanoparticles-surfactant and surfactant-fluid in the base fluids: (a) S1 and S2 for citric acid coated unwashed Fe_3O_4 nanoparticles in water, (b) S3 for citric acid coated washed Fe_3O_4 nanoparticles in water and (c) S4 for oleic acid coated Fe_3O_4 nanoparticles in toluene.

It has been observed that almost 10% of the total energy in the world is needed to maintain a pleasant atmosphere inside the building.[4] Hence, thermal insulation has been considered to play a crucial role to reduce the energy consumption of the building sector. Already, different types of insulating materials are commercially available in the market such as polystyrene [5], polyurethane [6], and fiber glass.[7] But, they are not produced from natural resources and hence they are not eco-friendly along with other limitations such as non-biodegradable nature, durability, and thermal stability is limited. Therefore, the use of environment-friendly and renewable insulating materials has attracted considerable attention from academic researchers, industries, and government [8], [9]. Literature survey has revealed that biopolymer-based renewable insulating materials such as cork [10], and wood chip were extensively used for thermal insulation application before the introduction of a cellulose-based smart material, but their insulating performance is lower with the thermal conductivity 0.040-0.050 w/mk as compared to the conventional insulating materials.[5], [6] Therefore, researchers intend to look for another potential biopolymer based insulating material. In this direction, cellulose has generated intense interest in recent years among the research community. Cellulose is the most abundant biomass available on earth. It is one of the next-generation biomaterials which is obtained from natural sources and thus can be utilized to develop cost-effective and environment-friendly insulating material. Within this dominion, efficient utilization of

renewable cellulose resources holds the potential for the development of sustainable products as alternatives to petroleum and mineral-based materials.

The effect of surface charge and surfactant coating on thermal conductivity has not been much explored earlier. Fe_3O_4 nanofluids were prepared in water and toluene with citric acid and oleic acid as surfactants respectively to understand the heat transfer mechanism. In this chapter, we show the role of the surface coating of the nanoparticle on the thermal properties of nanofluids and the thermal insulation potential of iron oxide nanoparticle embedded cellulose nanofibers (CNF). We have used homemade transient hot wire apparatus to investigate the thermal conductivity of these materials.

3.2 Characterization results of Iron Oxide nanofluids

The XRD pattern of the prepared samples shows the formation of a spinel phase with a lattice parameter of 8.37 Å which is close to the lattice parameter of magnetite (8.40 Å, JCPDS #19-0629) as shown in Figure 3.3(a). The average crystallite size calculated from the FWHM of the major peak using the Scherrer equation is 8 ± 1 nm. The added peaks in addition to the spinel peaks are observed in the unwashed sample (S1 and S4). This could be due to the contribution from the excess citric acid and the ammonium hydroxide base, which are denoted by stars in Figure 3.3(a) and these additional peaks are not present in the washed sample (S3).

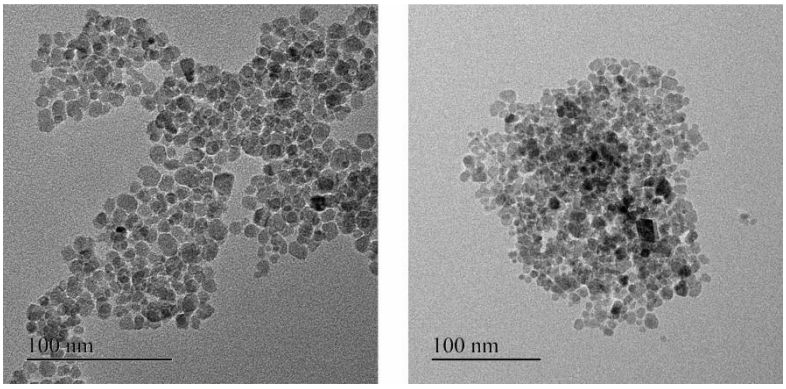

Figure 3.2: (a) TEM image of citric acid coated Fe_3O_4 nanoparticles, (b) TEM image of oleic acid coated Fe_3O_4 nanoparticles

The TEM images of the prepared citric and oleic acid coated samples are shown in Figure 3.2(a) and (b) respectively. The TEM image shows the formation of approximately spherical

particles of a size of around 10 nm. Figure 3.3(b) compares the infrared spectra of the washed, unwashed citric acid-coated sample and oleic acid-coated Fe_3O_4 nanoparticles. The band at around 600 cm^{-1} in all coated samples corresponds to the Fe–O stretching frequency and the band at around 1600 cm^{-1} corresponds to $–COO^-$ stretching frequency, which indicates that the surfactant molecules are directly attached to the Fe_3O_4 nanoparticles through the oxygen atom. Moreover, the band at 1750 cm^{-1} in the sample (S1) corresponds to the free carboxylic acid groups (–COOH), which indicates the presence of free acid molecules on the surface of the nanoparticles in the case of the unwashed sample (S1).[11] Dynamic Light Scattering (DLS) analysis of sample S1 (unwashed) shows an almost 17 nm hydrodynamic size with a narrow distribution and the sample S3 (washed) shows a hydrodynamic size of 28 nm with a wider distribution (Figure 3.3(c)). Although the amount of the surfactant in the sample S1 (unwashed)

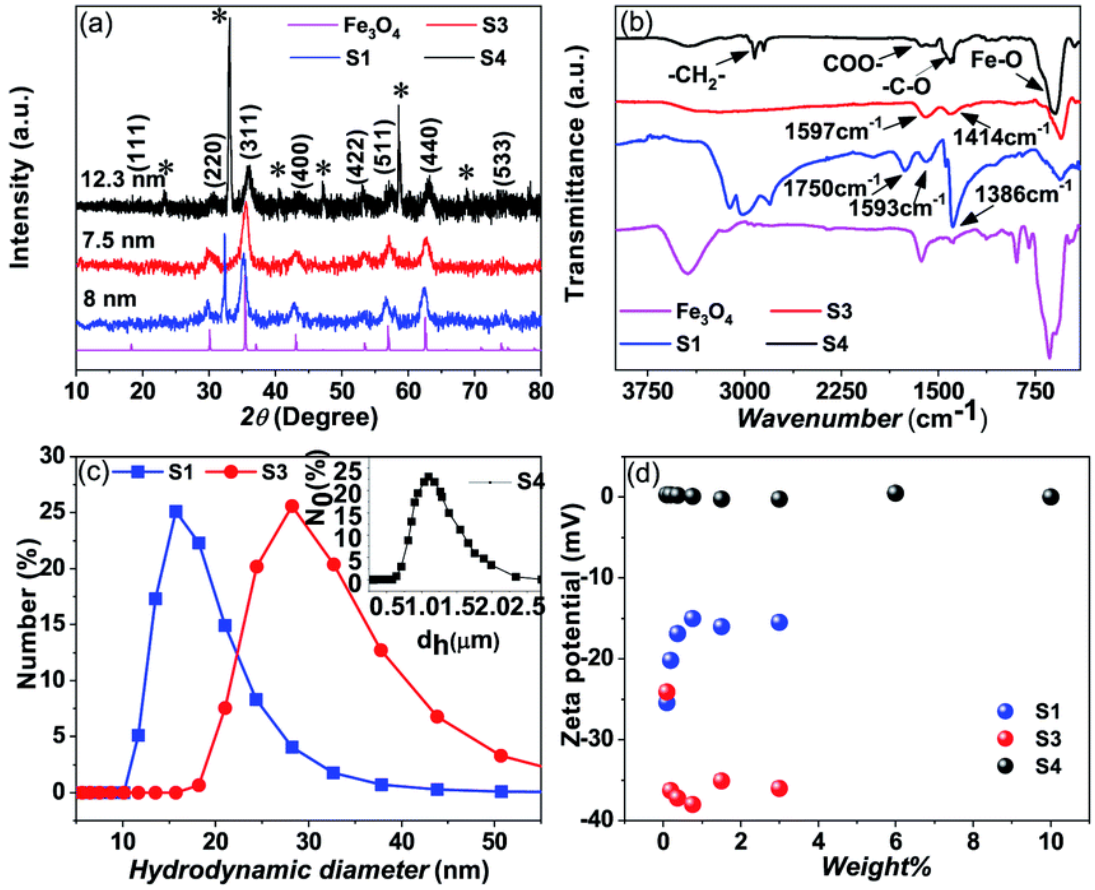

Figure 3.3: (a) XRD pattern of the prepared magnetite samples S1, S3 and S4, (b) FTIR vibration band spectra for samples S1, S3, S4 and Fe_3O_4 (c) DLS of the synthesized samples S1 and S3, and (d) zeta potential measurement for different weight percentages of magnetite nano-particles of samples S1, S3 and S4.

is larger than that in the sample S3 (washed), the observed smaller hydrodynamic diameter for sample S1 could be due to the particles that are well separated, possibly individual particles because a large amount of the non-magnetic surfactant layer on the surface of the nanoparticles suppresses the magnetic interaction between the particles and separates them apart by a repelling force of surface charge. But in the case of sample S3, a larger hydrodynamic diameter could be due to the formation of the small clusters/aggregation of the particles in the fluid due to the strong magnetic interaction between the particles with a small amount of the surfactants/charge on the surface.[11] Similarly for apolar surfactants, there is not much effect of the surfactant on the nanofluid and a large cluster is observed through DLS (see Figure 3.3(c)).

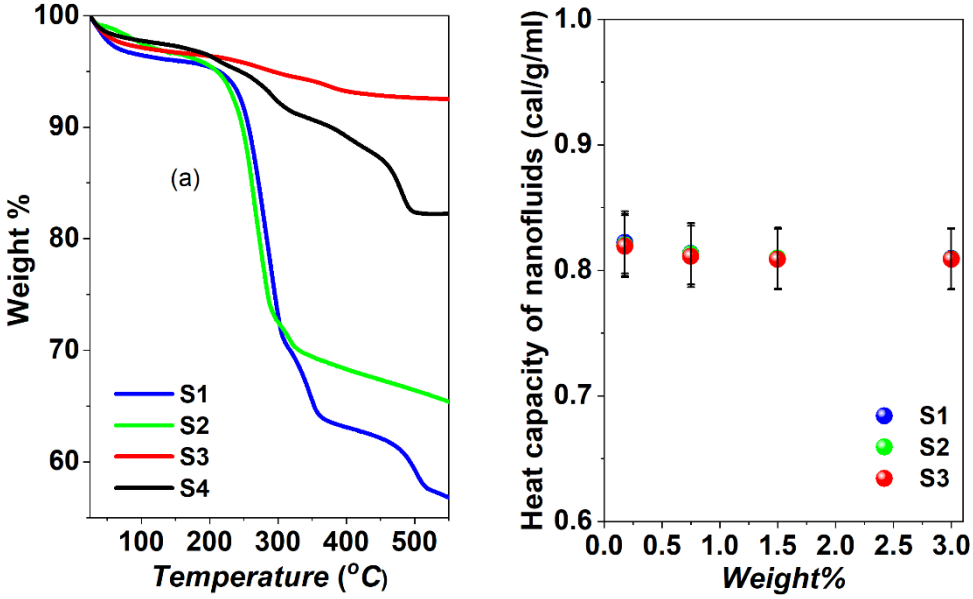

Figure 3.4: (a) Thermogravimetry analysis of samples S1, S2, S3 and S4, (b) heat capacity of samples S1, S2 and S3 with the weight percentages of magnetite nanoparticles

The zeta potential measurements of the citric acid coated (S1 and S3) samples and the oleic acid coated sample (S4) with different weight percentages of the samples are given in Figure 3.3(d). The washed (S3) citric acid-coated sample shows a more negative potential (-35 meV) than the unwashed sample (-14 meV). In the case of the unwashed sample (S1), the zeta potential initially decreases (-24 meV to -14 meV) with increasing concentration and then reaches a constant value with the concentration of the particles in the fluid. Since the sample (S1) is unwashed, increasing the concentration of the particles in the fluid also increases the number of ammonium ions (NH_4^+), which partially neutralizes the particle, leading to a decrease in the surface charge. But the observed high negative surface charge in the washed

sample (S3) could be due to the negative functional groups (3 COO^- groups and one OH^- group) present in the citrate ions. Moreover, the sample is washed properly by a dialysis process which removes the excess ammonium (NH_4^+) ions and excess citric acid molecules, which means that the particle surface contains only citric acid molecules with a high negative charge. The hydrophobic oleic acid-coated sample (S4) shows almost zero zeta potential. Although there are larger surfactants on the particle's surface, these particles are dispersed in a non-polar solvent (toluene) which shows zero zeta potential.

The amount of the surfactants for the washed and unwashed samples is confirmed by thermogravimetry analysis. Figure 3.4(a) shows the thermogravimetry analysis of all the citric acid-coated samples and oleic acid-coated samples. In the case of the citric acid-coated sample, the unwashed sample shows a larger amount of surfactant because the excess surfactants in the reaction medium stick to the surface of the nanoparticles as a secondary layer (physically adsorbed) during the drying process. But in the case of the washed sample, the excess surfactants were washed out by water along with the unreacted iron chlorides and ammonium hydroxides and have only less amount of the surfactant (chemically attached primary layer). The unwashed citric acid coated samples S1 and S2 show 37% and 32% surfactants respectively, whereas the washed sample has only 8% surfactants on its nanoparticle's surface. The oleic acid-coated sample shows 18% surfactants on the nanoparticle's surface. Figure 3.4(b) shows the heat capacity analysis of the different nanofluids samples with a different weight percentage of iron oxide nanoparticles. There is no change in heat capacity at room temperature is observed for these samples as measured by using a VP-DSC MicroCalorimeter (MicroCal, Malvern Instruments) (see Figure 3.4(b)). The thermal conductivity, $k = C_p \alpha_D \rho$, linearly depends on heat capacity, C_p, heat diffusivity, α_D, and density, ρ. It suggests that the thermal diffusivity of the nanofluid system changes drastically in a polar medium.

3.3 Thermal conductivity measurement results of iron oxide nanofluids.

Surfactant-coated nanoparticles are dispersed in appropriate solvents at different weight percentages to measure thermal conductivity; the samples S1, S2, and S3 are dispersed in water and the sample S4 is dispersed in toluene. Thermal conductivity measurement of the samples

was performed using the well-established transient hot-wire measurement technique. We used our homemade hot wire set up for the thermal conductivity measurements of samples. We calibrated the experimental setup using standard fluids such as water and toluene and compared our results with literature reports.[12] We observed almost ±1% uncertainty in our experimental results. In Figure 3.5 thermal conductivity measured by the transient hot-wire method is presented for different nanofluids. For the toluene-based nanofluid thermal conductivity has linear enhancement with wt% of NPs (black circles in Figure 3.5), whereas the water-based nanofluid shows deterioration of thermal conductivity with the wt% of NPs. The measured thermal conductivity of toluene and water is 0.13 $W/m^{-1}K^{-1}$ and 0.59 $W/m^{-1}K^{-1}$ respectively. The formula used to calculate the thermal conductivity of nanofluids is

$$k = \frac{q\beta V_0}{4\pi}\frac{d(lnt)}{d(\Delta V)} \tag{3.1}$$

The thermal conductivity of water-based iron oxide nanofluids deteriorated further with an increasing weight percentage of surfactant on the nanoparticles confirmed by TGA analysis. This shows that Wt% of surfactant on the nanoparticle surface has a dominant role in controlling the thermal transport in the nanofluid system.

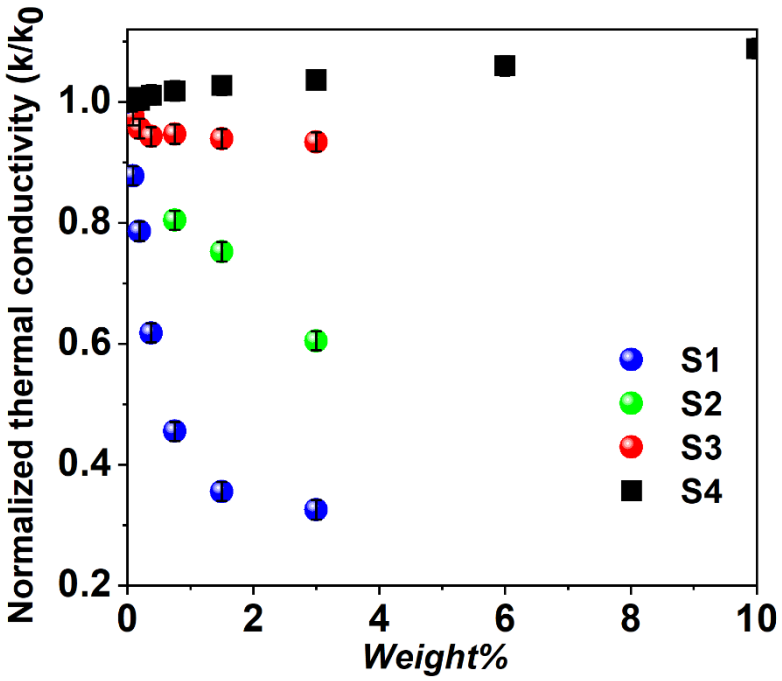

Figure 3.5: Thermal conductivity of samples S1, S2, S3 and S4 with different weight percentages of magnetite nanoparticles

3.4 Thermal conductivity measurement results of cellulose nanocomposites

The thermal conductivity of the CNF, iron oxide@CNF nanohybrids has been measured by the transient hot wire method at room temperature. The slope of the linear portion of the plot ΔV vs ln(t) for each sample was considered for the thermal conductivity calculation by the formula given in Eq. 3.1 as shown in Figure 3.6(a)

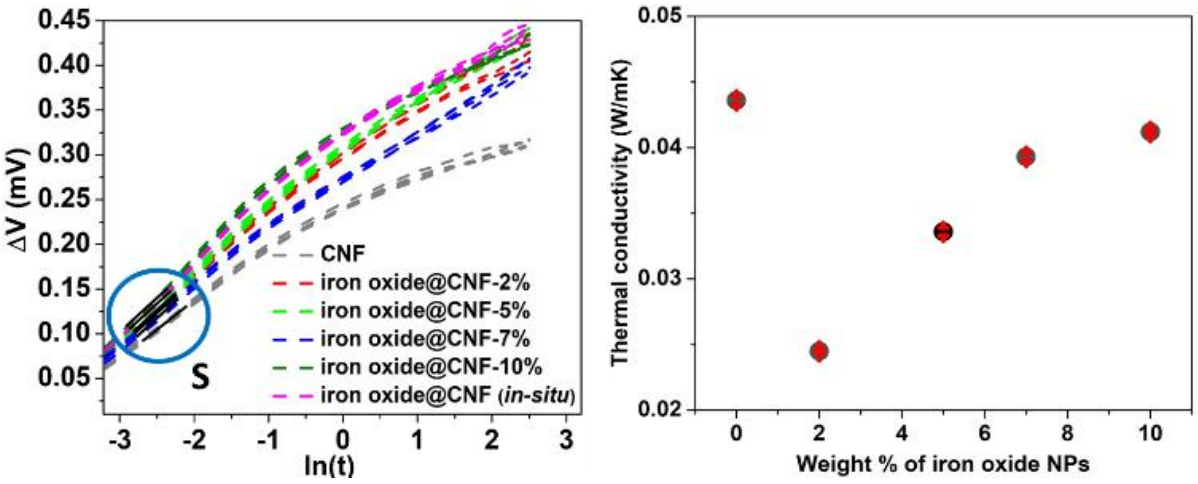

Figure 3.6: (a) The graphs of change in voltage of platinum wire (ΔV) with logarithmic of time of the measurement ln(t) for CNF**,** iron oxide**@**CNF nanohybrids by one-pot (2, 5, 7 and 10 weight% of iron oxide NPs) and iron oxide**@**CNF nanohybrid by in-situ, S is the slope of linear potion (b) The change in thermal conductivity with increase in weight% of iron oxide NPs.

We observed linear portion S in ΔV vs ln(t) graph for all the samples. There are different thermal conductivities k corresponding to different slopes S which represents the characteristics of the microstructure.[13] We observed the thermal conductivity k of the CNF, iron oxide@CNF nanohybrid by one-pot (2, 5, 7, and 10 % iron oxide NPs) and iron oxide@CNF nanohybrid by in-situ are in the range of 0.024-0.043 W/mK (see Figure 3.6(b)). Thus from the above results, very low thermal conductivity as low as 0.0245 W/mK for iron oxide@CNF-2% is observed which is lower than the air thermal conductivity at room temperature. The possible reason for this observed low thermal conductivity is the introduction of more fibril-fibril interaction which provides increased thermal resistance due to the dense pore walls in the assembled CNF. Thus, the dense pore walls of micron-sized pores are more effective to decrease the thermal conductivity of CNF nanohybrid compared to the Knudsen effect for nanoscale porous aerogel materials.[14] CNF Heat conduction through CNF is

reduced due to phonon surface scattering from the CNF aerogel, which results in the decrease of the overall thermal conductivity of the nanohybrid (see Figure 42(b)). The simple kinetic heat conduction model can be retained as

$$k = \frac{1}{3} C_v \nu \lambda_p \tag{2.15}$$

where k is the heat conductivity, C_v is the heat capacity, ν is velocity and λ_p is the mean free path of phonon.[15] The reported value of $C_v$and ν are 1.212 J K^{-1} g^{-1} and 2973 m S^{-1} respectively for bulk cellulose.[16], [17] Using λ_p, as cellulose nanofibers diameter around 20 nm, k = 0.024 W/mK (thermal conductivity only by heat conductivity). This value still suggests higher thermal conductivity than experimentally obtained value for iron oxide@CNF-2% nanohybrid. Hence the dense walls in the assembled CNF plays a crucial role in reducing both the thermal conduction and convection of nanohybrid. It is also to be noted that the thermal conductivity was increased with increasing the wt% of iron oxide (5, 7, 10 wt%) NPs. The thermal conductivity of porous aerogel materials depends on three parameters such as solid thermal conductivity, gaseous thermal conductivity, and radiation thermal conductivity.[18] It could be possible that the iron oxide nanoparticle is taking part as a contributor to solid conduction after a certain limit (2 wt% of iron oxide nanoparticles) which results in the increased thermal conductivity of CNF-based nanohybrids (5, 7, and 10 wt%). In this context, iron oxide has a thermal conductivity of 0.58 W/mK.[19] Hence, beyond 2% of the iron oxide NPs doping in CNF may have contributed towards enhancement in the conductivity.

3.5 Conclusion

In conclusion, the thermal transport properties in nanofluids and cellulose nanocomposites are investigated by a homemade transient hot wire experimental setup. We found that the surfactant plays an important role in the reduction of thermal conductivity in polar (water) nanofluids. A threefold reduction in thermal conductivity is found in water-based nanofluids with 3 wt% nanoparticles at 37 wt% of surfactant from 7 wt% of surfactant. In most biological applications such as hyperthermia and heat-triggered drug delivery, surfactant-coated nanoparticles are used; this study will be useful to design an experimental set-up and fine-tune clinical applications. On the other hand, After the incorporation of iron oxide NPs into the CNF

aerogel, the size of the pore is decreased resulting in a very low thermal conductivity value of 0.024 W/mK which is lower than the traditional thermal insulating materials polystyrene and mineral wool. Also, the thermal conductivity of the nanohybrid is lower than the air thermal conductivity at room temperature. These initial results provide sustainable motivation to augment the use of renewable thermal insulating material for applications in smart buildings.

References:

[1] K. Parekh and H. S. Lee, "Magnetic field induced enhancement in thermal conductivity of magnetite nanofluid," *J. Appl. Phys.*, vol. 107, no. 9, p. 09A310, 2010.

[2] D. Lee, J.-W. Kim, and B. G. Kim, "A new parameter to control heat transport in nanofluids: surface charge state of the particle in suspension," *J. Phys. Chem. B*, vol. 110, no. 9, pp. 4323–4328, 2006.

[3] W. Williams, I. Bang, E. Forrest, L. Hu, and J. Buongiorno, "Preparation and characterization of various nanofluids," 2019, pp. 285–288.

[4] H. Ong, T. Mahlia, and H. Masjuki, "A review on energy scenario and sustainable energy in Malaysia," *Renew. Sustain. Energy Rev.*, vol. 15, no. 1, pp. 639–647, 2011.

[5] K. Yucel, C. Basyigit, and C. Ozel, "Thermal insulation properties of expanded polystyrene as construction and insulating materials," 2003, pp. 54–66.

[6] J. K. Lee, G. L. Gould, and W. Rhine, "Polyurea based aerogel for a high performance thermal insulation material," *J. Sol-Gel Sci. Technol.*, vol. 49, no. 2, pp. 209–220, 2009.

[7] M. Koebel, A. Rigacci, and P. Achard, "Aerogel-based thermal superinsulation: an overview," *J. Sol-Gel Sci. Technol.*, vol. 63, no. 3, pp. 315–339, 2012.

[8] Y. Habibi, "Key advances in the chemical modification of nanocelluloses," *Chem. Soc. Rev.*, vol. 43, no. 5, pp. 1519–1542, 2014.

[9] Y.-Y. Li, B. Wang, M.-G. Ma, and B. Wang, "Review of recent development on preparation, properties, and applications of cellulose-based functional materials," *Int. J. Polym. Sci.*, vol. 2018, 2018.

[10] N. Hüsing and U. Schubert, "Aerogels—airy materials: chemistry, structure, and properties," *Angew. Chem. Int. Ed.*, vol. 37, no. 1-2, pp. 22–45, 1998.

[11] R. Lenin, A. Singh, and C. Bera, "Effect of dopants and morphology on the electrical properties of polyaniline for various applications," *J. Mater. Sci. Mater. Electron.*, vol. 32, no. 20, pp. 24710–24725, 2021.

[12] R. Gowda *et al.*, "Effects of particle surface charge, species, concentration, and dispersion method on the thermal conductivity of nanofluids," *Adv. Mech. Eng.*, vol. 2, p. 807610, 2010.

[13] B. Merckx, P. Dudoignon, J. Garnier, and D. Marchand, "Advances in Civil Engineering, 2012," *Artic. ID*, vol. 625395.

[14] K. Sakai, Y. Kobayashi, T. Saito, and A. Isogai, "Partitioned airs at microscale and nanoscale: thermal diffusivity in ultrahigh porosity solids of nanocellulose," *Sci. Rep.*, vol. 6, no. 1, pp. 1–7, 2016.

[15] K. Sato, Y. Tominaga, and Y. Imai, "Nanocelluloses and related materials applicable in thermal management of electronic devices: a review," *Nanomaterials*, vol. 10, no. 3, p. 448, 2020.

[16] A. V. Blokhin *et al.*, "Thermodynamic properties of plant biomass components. Heat capacity, combustion energy, and gasification equilibria of cellulose," *J. Chem. Eng. Data*, vol. 56, no. 9, pp. 3523–3531, 2011.

[17] I. Diddens, B. Murphy, M. Krisch, and M. Müller, "Anisotropic elastic properties of cellulose measured using inelastic X-ray scattering," *Macromolecules*, vol. 41, no. 24, pp. 9755–9759, 2008.

[18] X. Lu, R. Caps, J. Fricke, C. Alviso, and R. Pekala, "Correlation between structure and thermal conductivity of organic aerogels," *J. Non-Cryst. Solids*, vol. 188, no. 3, pp. 226–234, 1995.

[19] J. F. Shackelford and W. Alexander, *CRC materials science and engineering handbook*. CRC press, 2000.

Chapter 4

Effect of dopants and morphology on the electrical properties of polyaniline (PANI)

4.1 Introduction

The conducting polymers have been focused in recent years for many applications because their electrical conductivity ranges from semiconductors to metals. The polymer-based materials are flexible, lightweight, less toxic, cost-effective, easy to synthesize, and ease of processability than inorganic materials.[1]–[3] Moreover, the electrical conductivity of the conducting polymers can be tuned by doping in the polymeric matrix.[4], [5] Owing to the many attractive features, conducting polymers are being focused in many applications such as flexible electronics [1], flexible thermoelectrics [6], electrochemical energy storage and conversion[7], electromagnetic shielding [8], sensors [9]–[12], actuators[13], and hydrogen storage [14], etc. Although there are many advantages, some drawbacks, such as low electrical conductivity, thermal stability, and solubility of the polymers in solvents, limit their use in many applications [15]. The electrical conductivity of the conducting polymer can be improved in different ways, such as doping the polymer matrix with appropriate dopant material, changing the concentration of the dopant material in the polymer matrix , and changing the structural morphology of the polymer chain [16]. Moreover, doping the polymer matrix improves the polymer's solubility and makes it easy for the solution processability of the polymer.[15]

Doping in the polymer matrix is one of the easiest ways to improve the electrical conductivity of the conducting polymer.[17], [18] The type of dopant material (p-type or n-type) decides

whether the polymer matrix is a p-type or n-type material.[19], [20] The p-type doping removes an electron from the HOMO, creating a hole in the polymer backbone. The n-type doping adds an electron to the LUMO and creates an electron in the backbone of the conducting polymer .[21] The electrical conductivity of the polymer matrix can also be tuned by changing the doping concentration in the polymer matrix, which can be improved from 10-8 Scm^{-1} (undoped state) to 104 Scm^{-1} (doped state). Many organic and inorganic acids have been used as doping molecules, such as hydrochloric acid (HCl) [22], camphor sulfonic acid (CSA) [23], [24] naphthalene sulfonic acid [25], phosphoric acid [26], and other organic acids.[27] In case of polyaniline, the protonic acid dopants initially protonate the nitrogen atoms in the quinonoid structure and form the bi-polaron structure. Then, the bi-polaron dissociates immediately and forms polaron structure (radical cation) and this polaron separates and forms a polaron lattice. The polarons' moves in the lattice lead to improved electrical conductivity in the polymer.[28] However, in thermoelectric applications, the higher doping concentration increases the carrier concentration in the polymer matrix, leading to increases in electrical conductivity, but this pushes the Fermi energy inside the conduction band, leading to decreases in the Seebeck coefficient.[20] This trade-off relationship between the electrical conductivity (σ) and Seebeck coefficient (S) strongly influences the power factor ($P = \sigma S^2$) of the polymers.

The one-dimensional polymer nanostructures, such as nanowires, nanofibers, and nanorods, show improved electrical conductivity.[25], [29] The electrical conductivity (σ) of a semiconductor depends on the concentration of the charge carriers (n) and the mobility of the charge carriers (μ), i.e., $\sigma = ne\mu$.[6] These one-dimensional polymer nanostructures show higher charge carrier mobility due to the ordered arrangement of polymer chains compared to the entangled polymer chains in the bulk structure.[30] In thermoelectrical applications, the recent research is focusing on improving the power factor ($P = \sigma S^2$) of the polymer-based materials by decoupling the interdependent parameters such as electrical conductivity (σ) and Seebeck coefficient (S) by making polymer nanostructures and nanocomposites with the polymer.[30], [31] Improving electrical conductivity without increasing the charge carriers has been achieved by making the nanostructures of polymers such as nanowires, nanorods, and nanosheets. In chemiresistor or conductometric sensor applications, the one-dimensional nanowire shows high sensitivity and fast current response. The smaller diameter of the nanowire improves the current response in the axial direction, and the high surface area of the nanowire improves the sensitivity of the nanowire.[32] The one-dimensional conducting polymer nanowires and their composite nanowires are recently being focused on the energy

storage and conversion devices such as supercapacitors and batteries.[33] Out of various conducting polymers, polyaniline (PANI) has many attractive features over the other conducting polymers such as inexpensive, environmental stability, easy synthesis protocol, easy processability, and tunable electrical conductivity.[34], [35] The conducting polyemeraldine salt shows conductivity of 1–5 Scm^{-1}, and the conductivity of the polymers can be tuned up to 400 Scm^{-1} by doping with acids in the polymer matrix. In the present work, we have synthesized the HCl-doped polyaniline at different dopant (HCl) concentrations by simple oxidative polymerization method and studied the effect of dopant concentration on the electrical properties of polyaniline. We also prepared HCl-doped, CSA-doped, and citric acid (CA)-doped polyaniline nanofibers using the interfacial polymerization method and studied the effect of doping materials on the electrical properties of the polyaniline. Moreover, we also prepared the polyaniline in different morphologies with the same doping material and studied the effect of morphology on the electrical properties of the polyaniline.

4.2 Characterization results

The powder XRD pattern of the polyaniline samples synthesized using different synthesis methods is shown in Figure 4.1. There are three peaks observed in all the samples between the 2θ values 10^0 and 30^0, and all the three peaks are broad that indicates the formation of the amorphous or semi-crystalline nature of polyaniline. Moreover, the observed patterns for the polyaniline samples are due to the parallel and perpendicular periodicity of the polymer. The peaks observed at the $2\ \theta$ values 15.3^0, 20.8^0, and 25.4^0 correspond to the reflection from the planes (011), (020), and (200), respectively, and the corresponding d-spacing values are 5.786, 4.267, and 3.504 Å, respectively. The sample prepared using simple oxidative polymerization (PANI-ED) shows sharp peaks, and this could be due to the formation of semicrystalline polyaniline, as shown in Figure 4.1(a). Whereas, the peak broadness is observed in the samples prepared by oxidative polymerization (PANI-NW) and interfacial polymerization (PNF-HCl, PNF-CSA, and PNF-CA) indicates that the amorphous nature of the polyaniline (Figure 4.1 (b and c). Moreover, the intensity of the peaks at 15.3^0, 20.8^0, and 25.4^0 are considerably reduced for those samples. The amorphous nature and the reduction in the intensity could be due to the formation of the smaller size (nanosize) particles.

The TEM images of the prepared polyaniline samples are shown in Figure 4.2. The images show the formation of different morphologies for the samples synthesized using different synthesis methods. The simple oxidative polymerization of aniline using ammonium persulfate (PANI-ED) shows highly entangled polymer chains and forms micro-sized particles, as shown in Figure 4.2(a). But, the similar oxidative polymerization is carried out using a mixture of

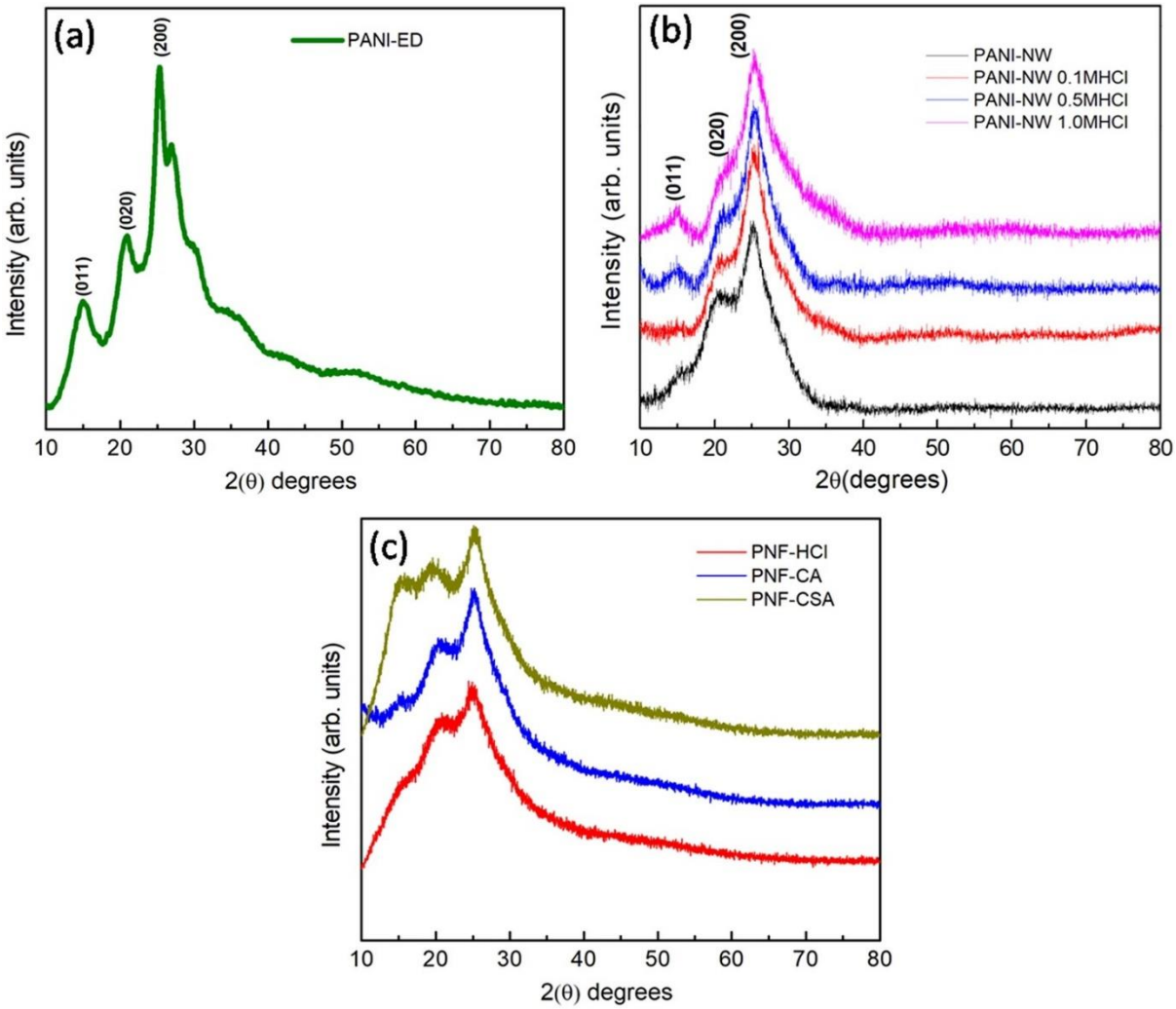

Figure 4.1: Powder XRD pattern of the polyaniline samples synthesized by (a) the oxidative polymerization using APS, (b) oxidative polymerization using APS + $FeCl_3$ and (c) interfacial polymerization using APS

ammonium persulfate and ferric chloride (PANI-NW) shows the formation of nanowhiskers with a diameter ~ 50 nm and length ~ 200 nm, as shown in Figure 4.2(b and c). The interfacial polymerization of aniline with APS produces fine nanofibers, and the diameter of nanofibers is ~ 50 nm and the length of the nanofibers is ~ 500 nm, as shown in Figure 4.2(d–f), and this is due to the controlled exposure of aniline to the oxidizing agent at the aqueous and non-

aqueous interface. Figure 4.2(d–f) are the nanofibers of polyaniline prepared by doping with HCl, CSA, and CA, respectively. From the TEM image, it is clearly seen that the CA-doped nanofibers (PNF-CA) have a rough surface as compared to HCl-doped (PNF-HCl) and CSA-doped (PNF-CSA) polyaniline nanofibers. The observed rough surface could be due to the irregular orientation of the polymer chains at the surface of the polyaniline nanofibers. From the microscopic images of prepared polyanilines, it is clear that the oxidative polymerization with different oxidants forms different morphologies, and also the different method of polymerization produces the different morphologies of polymer.

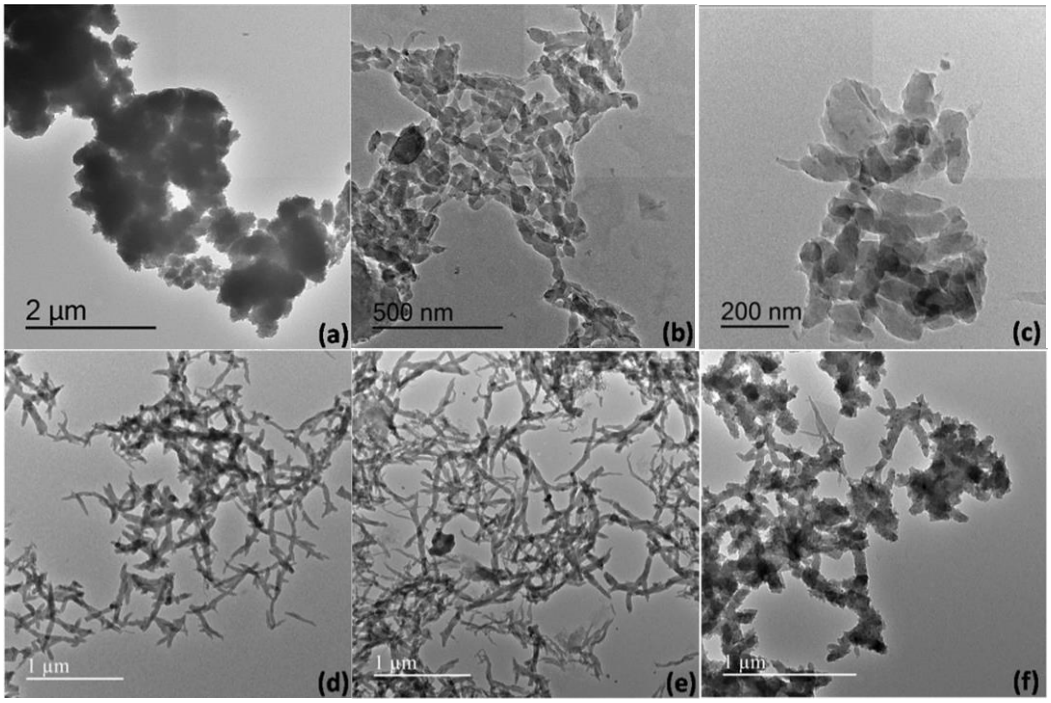

Figure 4.2: TEM images of the polyaniline prepared by simple oxidative polymerization (a–c) and interfacial polymerization (d–f)

The infrared spectra of the prepared HCl, CSA, and CA-doped polyaniline samples are shown in the Figure 4.3. All the three samples show almost similar pattern of transmittance, and the bands are observed at 3225 cm^{-1}, 1557 cm^{-1}, 1488 cm^{-1}, 1288 cm^{-1}, 1225 cm^{-1}, 1122 cm^{-1}, 801 cm^{-1}, and 590 cm^{-1}. The bands at 1557 cm^{-1} and 1488 cm^{-1} correspond to the C = C stretching frequencies of quinoid and benzenoid structures of polyaniline, respectively. The band at 801 cm^{-1} corresponds to the out-of-plane bending vibration of the C–H bond in the 1,4-disubstituted benzene ring. The band at 1122 cm^{-1} is due to the in-plane bending vibration of the C–H bond in the quinoid structure. The bands at 1288 cm^{-1} and 1225 cm^{-1} correspond to the C–N stretching frequencies of the benzenoid ring in the polyaniline. The broad band centered at

3225 cm^{-1} is due to the N–H stretching frequency. The bands from 590 cm^{-1} correspond to the chloride ions in the polyaniline samples which could be from the doped HCl.[36], [37] The observed bands in the prepared polyaniline samples indicate that the formation of the emeraldine base (EB).

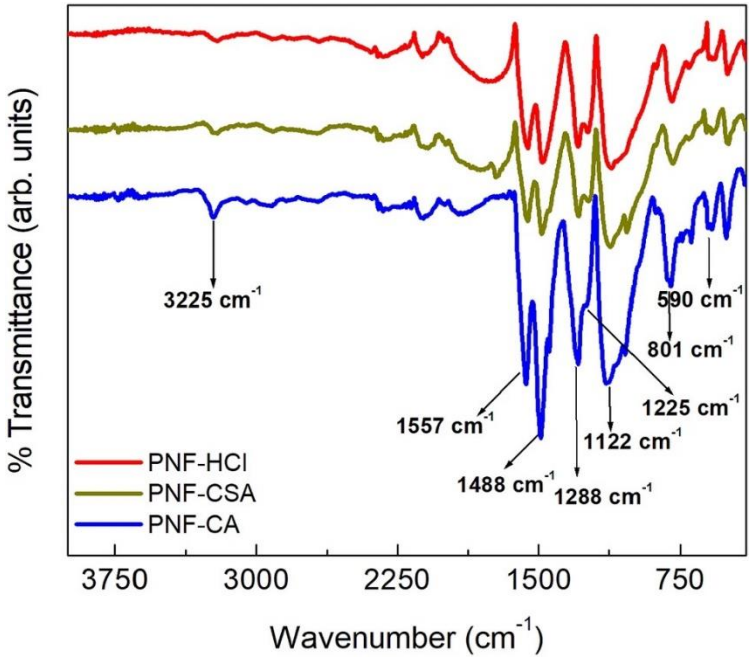

Figure 4.3: Infrared spectra of polyaniline samples synthesized using different acids

Thermogravimetric analysis curves of the undoped and different acid-doped polyaniline samples are shown in Figure 4.4 (a and c), and the corresponding derivative curves are shown in Figure 4.4(b and d). The TGA curves of undoped polyaniline sample (PANI-NW) and the HCl-doped samples at different concentration are (see Figure 4.4a) following almost similar trend in the weight loss. The TGA curves in Figure 4.4a and DTG curves in Figure 4.4b clearly indicate that there are three-step weight losses for the prepared polyaniline samples. Similar kinds of weight loss have been reported in the literature for the acid doped polyanilines.[38], [39] The first weight loss (~ 10%) below 120 ^{0}C for all the samples is due to the loss of adsorbed water molecules in the polymer matrix, unreacted monomers. The second weight loss from 120 to 380 C (~ 19%) for the sample PANINW (undoped) is due to the water molecules attached to the polymer matrix as dopants, and the weight loss from 120 to 315 ^{0}C (~ 7%) for HCl-doped samples could be due to the loss of dopant materials and the loss of lower molecular weight oligomers in addition to the water molecules attached to the polymer matrix. The third weight loss from 380 to 650 ^{0}C for the undoped sample (~ 20%) and 315 to 650 ^{0}C for the

HCl-doped samples (~ 25%) could be due to the decomposition of the polymer matrix (see Figure 4.4(a and b)) [38].

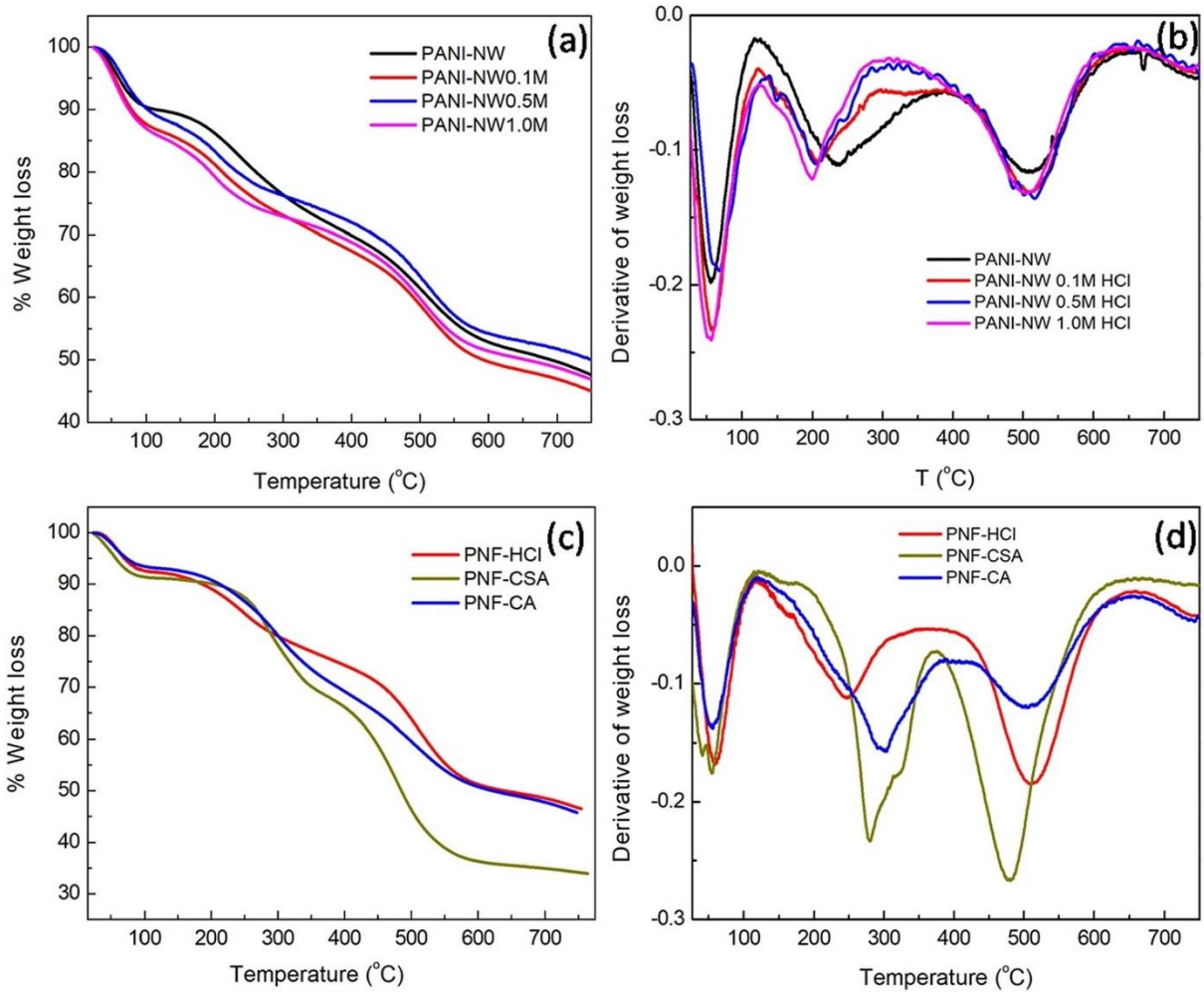

Figure 4.4: (a) TGA curves of polyaniline doped with different concentrations of HCl and the corresponding (b) DTG curves, and (c) the TGA curves of polyaniline doped with different dopant materials and (d) the corresponding DTG curves.

The thermogravimetric curves of polyaniline samples prepared by interfacial polymerization with different dopant materials (PNF-HCl, PNF-CSA, and PNF-CA) also show similar pattern of weight loss (Figure 4.4(c)), but the position of the weight loss in the temperature scale is different for different dopant materials. The first weight loss below 120 ^{0}C is almost same (~ 9%) for all the three different acid-doped polyaniline samples. But the second and third weight losses are different for different acid-doped polyaniline nanofiber samples. The observed second weight loss for the HCl-, CA-, and CSA-doped polyaniline samples are ~ 16% (120 to 360 ^{0}C), ~ 22% (120 to 375 ^{0}C), and ~ 25% (120 to 400 ^{0}C), respectively (see Figure 4.4(d)), and the difference in the weight loss is due to the difference in the thermal stability of the

dopant materials.[39], [40] The observed third weight loss for the HCl-, CA-, and CSA-doped samples are ~ 25% (360 to 650 ^{0}C), ~ 21% (375 to 650 ^{0}C), and ~ 31% (400 to 650 ^{0}C), respectively, and this corresponds to the structural decomposition of the polymer matrix.

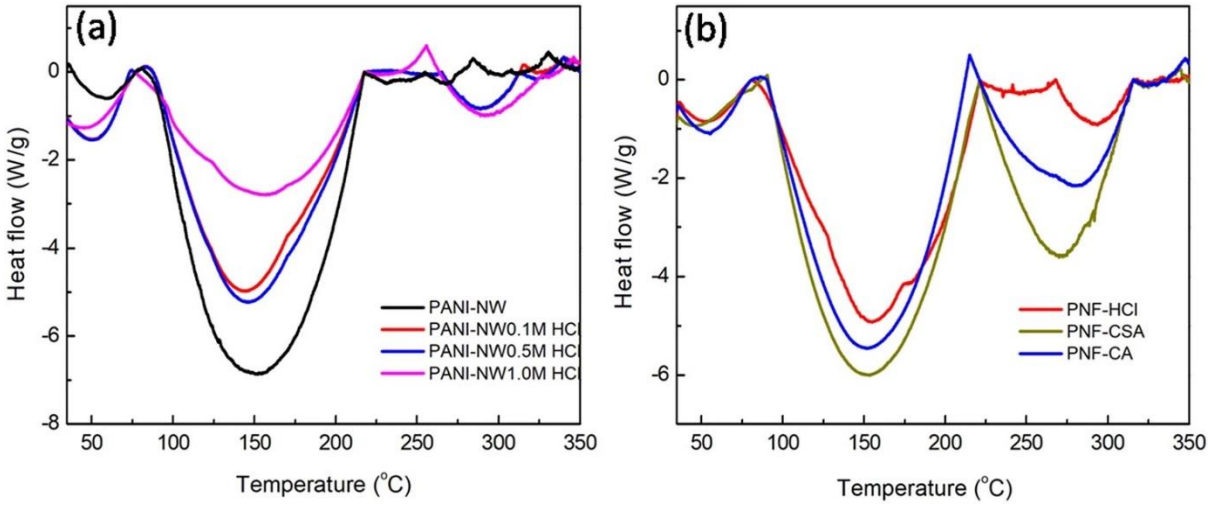

Figure 4.5: DSC curves of polyaniline samples doped (a) with different concentration of doping material and (b) with different types of dopant materials

The DSC studies of all prepared polyaniline samples show three endothermic peaks (see in Figure 4.5). The first low-intensity endothermic peak below 100 ^{0}C could be due to the removal of moisture or solvent molecules present in the sample, and the corresponding weight loss is observed below 120 ^{0}C in TGA [48]. The second more intense endothermic peak around ~ 150 ^{0}C corresponds to the removal of water molecules attached to the polymer matrix as secondary dopants [46, 49] and the less-intense endothermic peak around ~ 300 ^{0}C corresponds to the removal of the dopant materials and oligomers present in the sample. The weight loss corresponds to these second and third endothermic peak observed between 120 and 350 ^{0}C in the TGA analysis. The endothermic peak corresponds to the breakage of amine bonds in the polymer chain (decomposition of the polymer) is not seen in the DSC data and it may be appear at higher temperature (above 400 ^{0}C) [41]. The observed intensity of the endothermic peak at ~ 150 ^{0}C decreases with increasing the concentration of the doping in polymer matrix (as shown in Figure 4.5a) which indicates decreasing the concentration of the water molecules attached to the polymer matrix as secondary dopants. The intensity of the endothermic peak at ~ 300 ^{0}C increases with increasing the doping concentrations indicates that the peak corresponds to the removal of the dopant molecules in the polymer matrix. The peak positions of the less-intense endothermic peak at ~ 300 ^{0}C in polyaniline nanofiber samples doped with

different dopant materials are different (as shown in Figure 4.5b), and this could be due to the difference in the thermal stability of the dopant materials

The UV–Visible spectrum of the entangled polyaniline sample (PANI-ED) shows two absorption bands, one at 379 nm and another at 648 nm, as shown in Figure 4.6(a). The first absorption band at the lower wavelength (379 nm) corresponds to the $\pi - \pi^*$ transition in the benzenoid segment of the polyaniline and the band at a higher wavelength (648 nm) corresponds to the $n - \pi^*$ transition in the quinoid segment, i.e., the transition from the HOMO of the benzenoid ring to LUMO of the quinoid ring and this band indicates the oxidation state of the polyaniline.[42], [43] The observed intensity of the quinoid band is larger than the intensity of the benzenoid band, which indicates that the degree of oxidation of polyaniline could be slightly higher than that of the emeraldine base (EB) phase. The corresponding optical

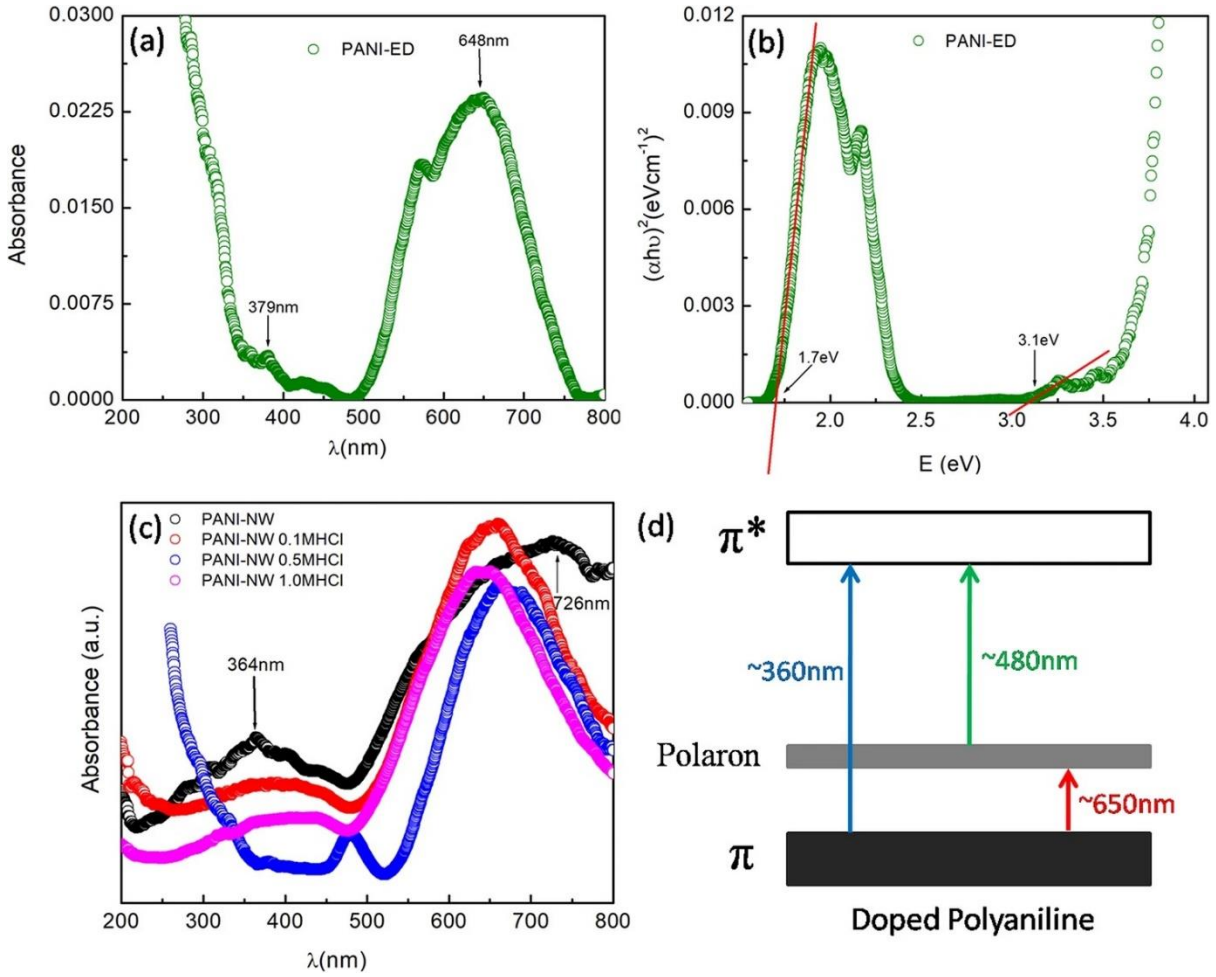

Figure 4.6: The absorption spectrum (a) and their corresponding optical band gap (b) of entangled polyaniline sample (PANI-ED), (c) absorption spectra of the HCl-doped polyaniline nanowhiskers with different concentrations and (d) the possible energy transitions.

band gap calculated using tauc plot is 3.1 eV and 1.7 eV for the benzenoid and quinonoid segments, respectively, as shown in Figure 4.6(b). The UV–Visible spectra of the prepared polyaniline nanowhisker samples (PANI-NW) treated with HCl solution of different concentrations is shown in Figure 4.6(c). The freshly prepared polyaniline nanowhiskers treated only with water (PANI-NW) show two absorbance bands, one at 364 nm and another at 726 nm. The band at the lower wavelength (364 nm) corresponds to the $\pi - \pi^*$ transition in the benzenoid segment of the polyaniline, and the band at a higher wavelength (726 nm) corresponds to the $n - \pi^*$transition in the quinoid segment, as observed in the sample PANI-ED (see Figure 4.6(a)).[42] But, the observed difference in band positions could be due to the formation of nanowhiskers morphology in the PANINW sample (as seen from the TEM image in Figure 4.2(c and d). In case of HCl-treated samples, the first absorbance band at 364 nm is red-shifted, which indicates that the doping of HCl in polyaniline matrix, and this reduces the $\pi - \pi^*$ band energy. Moreover, new absorbance bands are appeared around ~ 650 nm and ~ 480 nm (only in PANI-NW 0.5 M HCl), and these new bands at longer wavelength region (~ 480 nm and ~ 650 nm) are due to the excitonictype transition such as polaron and bi-polaron transition in the doped polyaniline samples, as shown in Figure 4.6 (c and d) [44], [45].

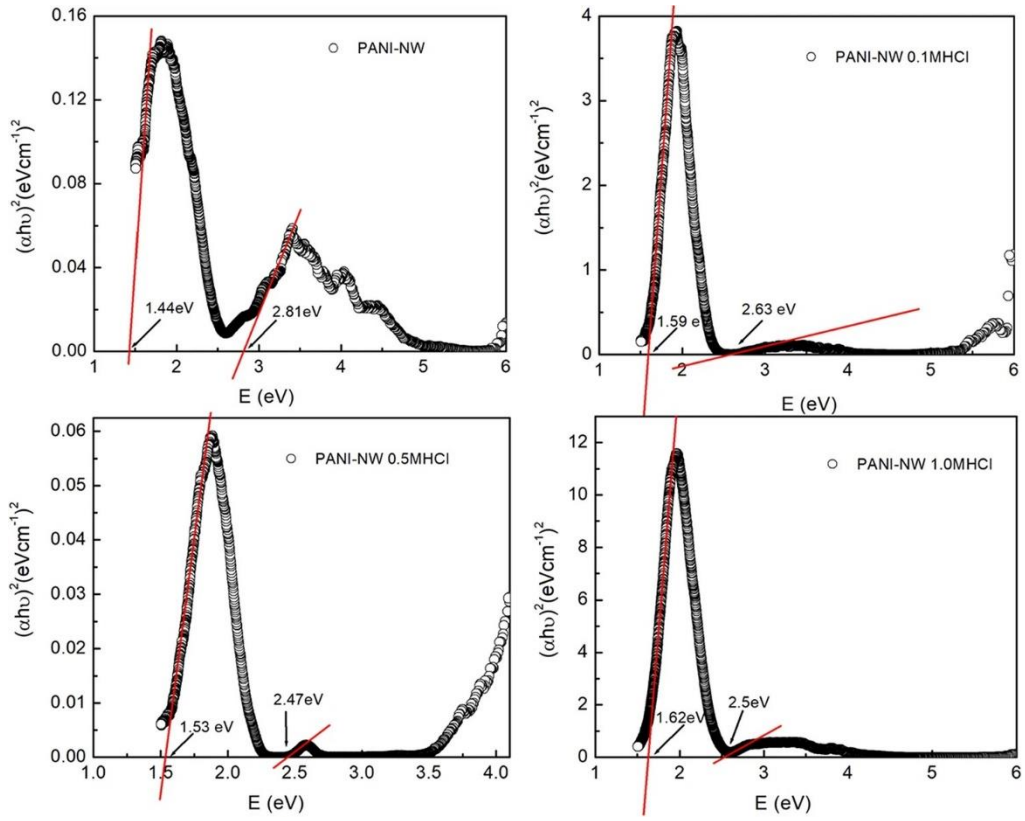

Figure 4.7: The optical bandgap of the acid-doped polyaniline nanowhiskers

Moreover, the intensity of the band at 364 nm decreases with increasing the concentration of HCl, which indicates that the excitonic type transitions due to polarons and bi-polarons are dominated in the doped polyaniline samples over the $\pi - \pi^*$ transition. In case of the PANI-NW 0.5 M HCl sample, the intensity of the band at $\sim$ 360 nm ($\pi - \pi^*$ transition) has almost diminished, and the polaron bands are dominating in the transitions. Moreover, the observed intensity ratio of the quinoid to the benzenoid band, i.e., quinoid (π-polaron)/benzenoid ($\pi - \pi^*$), increases with the concentration of the HCl and indicates that doping increases with the concentration of the HCl [46].

The optical band gap calculated from the absorption bands of the HCl-doped polyaniline nanowhisker samples at different concentrations is shown in Figure 4.7. In the pure polyaniline sample, two optical band gaps are observed, one at 1.44 eV, which corresponds to the $n - \pi^*$ transition in the quinonoid segment, and another at $\sim$ 2.81 eV due to the $\pi - \pi^*$ transition at the benzenoid segment.[47] The observed bandgaps are less than that of the bandgaps in the PANI-ED (1.77 eV and 3.01 eV) sample, as shown in the Figure 4.6(b). This could be due to the formation of nanowhisker morphology in the PANI-NW sample. The bandgap due to the $\pi - \pi^*$ transition decreases with increasing dopant (HCl) concentration, and which reduces from 2.8 to $\sim$ 2.5 eV for the concentration from 0 M HCl to 1.0 M HCl. But, the trend was not followed for the π-polaron band at $\sim$ 650 nm ($\sim$ 1.5 eV), and this could be attributed to the contribution of the high-energy polaron-π* transitions in addition to the low energy π-polaron transition (as shown in the Figure 4.6(d)). The observed low bandgap (2.47 eV) in the PANI-NW 0.5M HCl sample corresponds to the polaron-π* transition (479 nm), as shown in Figure 4.7(d). The polaron-π* and π-polaron transitions are more dominated in the PANI-NW 0.5M HCl sample as compared to the $\pi - \pi^*$ transition, that could be the reason for the absence of the transition at high-energy region ($\pi - \pi^*$). The variation absorption position and the optical bandgap of the doped samples are compared in Table 4.1. The absorption spectra of the polyaniline nanofiber samples (PNF) synthesized by interfacial polymerization (IP) with different dopants (HCl, CSA, and CA), and their corresponding optical band gaps are shown in Figure 4.8. The exact band positions and their corresponding bandgaps are shown in Table 1. All the three samples show almost similar absorption pattern with three absorption bands which correspond to the $\pi - \pi^*$, polaron-π*, and π-polaron transitions [43], [46], [48]. The position of the polaron-π* band is observed at $\sim$ 480 nm for all the samples with the band energy gap 2.4 eV, but the positions of the π-polaron and $\pi - \pi^*$, absorption bands are different for the different acid-doped samples. The π-polaron bands at a higher wavelength

region are 665 nm (1.59 eV), 695 nm (1.55 eV), and 611 nm (1.77 eV) for the PNF-HCl, PNF-CSA, and PNF-CA samples, respectively. This indicates that the energy gap for π-polaron transition is large

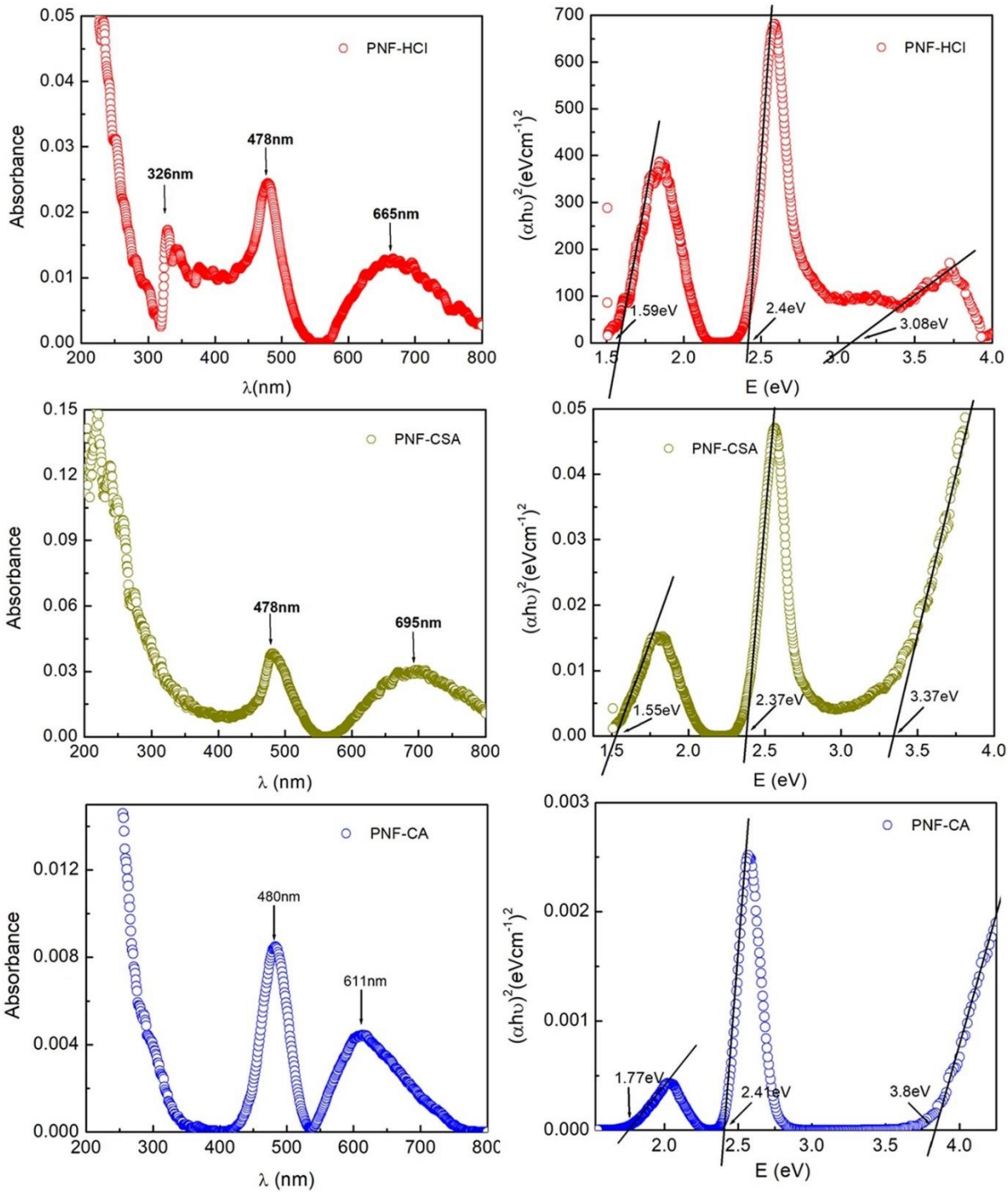

Figure 4.8: The absorption spectra and the optical bandgap of the HCl-, CSA-, and CA-doped polyaniline nanofiber samples

for PNF-CA (1.77 eV) sample as compared to the PNF-HCl and PNF-CSA polyaniline nanofibers. The $\pi - \pi^*$, band for the PNFHCl sample is observed at 326 nm (3.08 eV), and this absorption band is not visible clearly for the PNFCSA and PNF-CA samples, but a small shoulder is observed below 300 nm (i.e., ~ 290 nm). This low intensity $\pi - \pi^*$ bands at low wavelength region (< 300 nm) also confirmed by the calculated larger band energy for the

Table 4.1: The bands observed spectra and their corresponding optical band

Sample name	Wavelength (nm)			Band gap (eV)			σ (Scm^{-1})	Activation energy E_g (eV)
	$\pi - \pi^*$	Polaron-π^*	$\pi - polaron$	$\pi - \pi^*$	Polaron-π^*	$\pi - polaron$		
PANI-ED	379	-	648	3.1	-	1.70	0.26	0.187
PANI-NW	364	-	726	2.81	-	1.44	1.98	0.174
PANI-NW-0.1MHCl	383	-	661	2.63	-	1.59	3.14	0.155
PANI-NW-0.5MHCl	-	479	661	-	2.47	1.53	9.8	0.084
PANI-NW-1.0MHCl	405	-	640	2.50	-	1.62	10.2	0.147
PNF-HCl	326	478	665	3.08	2.40	1.59	1.75	0.109
PNF-CSA	< 300	478	695	3.37	2.37	1.55	1.27	0.122
PNF-CA	< 300	480	611	3.80	2.41	1.77	0.22	0.165

PNF-CSA (3.37 eV) and PNF-CA (3.80 eV) samples as compared with the PNF-HCl (3.08 eV) samples. This indicates that the polaron transitions are more prominent in the CSA- and CA doped samples as compared to the larger bandgap $\pi - \pi^*$ transition. The difference in the absorption spectrum in the three different acid-doped samples could be due to the extent of doping and the difference in the degree of oxidation state in the polyaniline structure, i.e., the difference in the benzenoid and quinonoid rings ratio.[45], [49] This indicates that the different

types of doping in the polyaniline matrix alter the electronic transitions in the backbone of the polymer.

The effect of the different levels of HCl doping on the work function of PANI nanocomposites was studied using the X-ray photoelectron spectroscopy (XPS). As shown in the Figure 4.9 (a), the work function (Φ) of different samples was determined by Ultraviolet photoelectron spectroscopy (UPS) as $\Phi = h\nu - E_{cutoff}$, where, $h\nu$ is the UV source energy (21.2 eV) and E_{cutoff} is the cut-off point of secondary electron edge (SEE) where tangent cut the x-axis. From Figure 4.9 (a), it can be observed that the SEE is shifting when the concentration of HCl varied in PANI. The estimated work function of the PANI-ED, PANI-NW, and PANI-NW with different concentrations of HCl is shown in Figure 4.9(b). The work function of the PANI-NW decreases with increasing HCl concentration levels. The measured work function on the surface of PANI samples decreased from 4.04 ±0.1 eV for PANI-NW to 3.81± 0.1 eV for PANI-NW-0.5 M HCL and further increased to 3.91±0.1 eV for PANI-NW-1 M HCl. This change in work

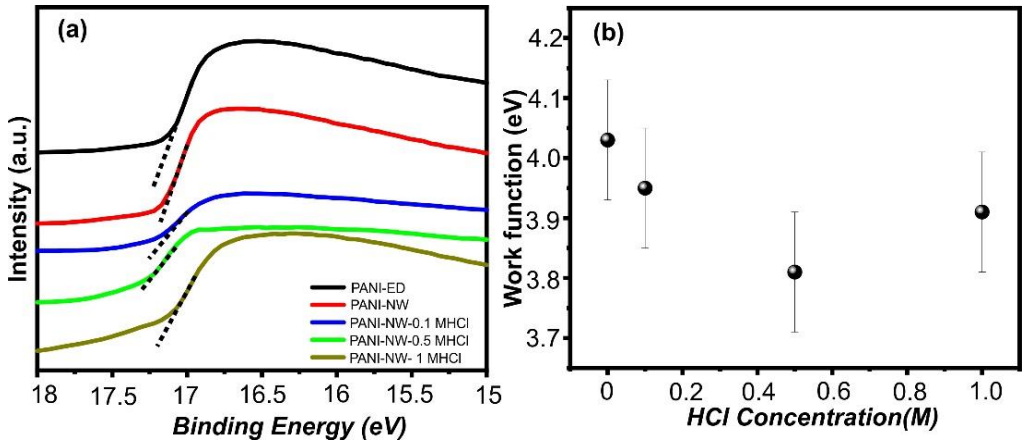

Figure 4.9: (a) UPS spectra of PANI-HCl samples. (b) the work function of the PANI -NW as a function of HCl doping concentrations.

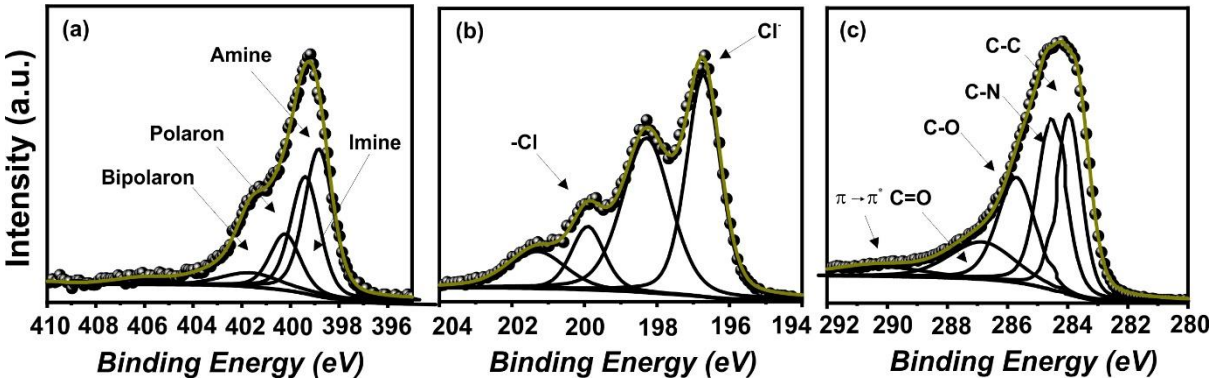

Figure 4.10: The high resolution XPS spectra of N 1s, Cl 2p andC 1s core level spectra of PANI-ED sample

function occurs due to the effect of protonation on the electronic structure of the PANI. A large number of free holes in the form of polaron and bi-polarons in the polymer chains result in lower work function values.[24], [50], [51] The electronic structure of the PANI undergoes an internal redox, which forms bipolarons.[52].

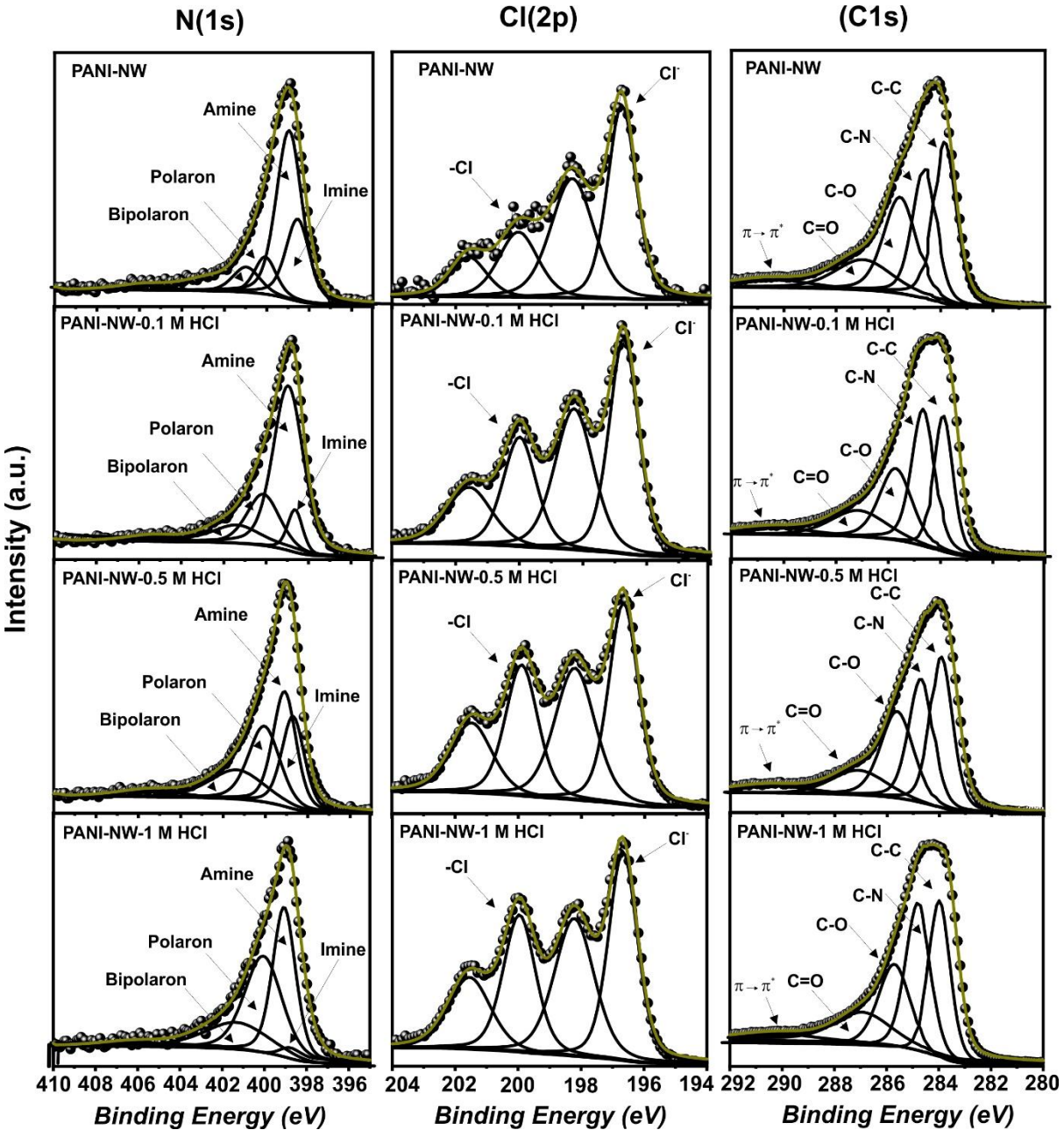

Figure 4.11: First, second and third column is the core level spectra and deconvolution of the N 1s, Cl 2p and C 1s respectively for PANI-NW, PANI-NW-0.1 M HCl, PANI-NW-0.5 M HCl and PANI-NW-0.1 M HCl.

In the XPS analysis of PANI samples, the relative contribution from the various polymeric components is resolved. XPS is the useful tool to explain the electronic features of polaron/bi-polarons and the degree of doping as the ratio of the positively charged nitrogen species to the total nitrogen (N^+/N).[53], [54]. The core level spectra and deconvolution of N 1s, Cl 2p and C 1s for PANI-ED are shown in the Figure 4.9. Similarly, the core level spectra of N 1s, Cl 2p and C 1s for PANI-NW, PANI-NW-0.1 M HCl, PANI-NW- 0.5 M HCl and PANI-NW-1 M HCl are shown in the Figure 4.10. The N 1s spectra resolved into four peaks, C 1s spectra resolved into five peaks and Cl 2p spectra resolved into four peaks using the gaussian function as reported in the literature.[55], [56] The Binding energy of the four N 1s peaks are located at 398.6 eV(imine), 399.3 eV(amine), 400.4 eV (polaron) and 401.5 (bi-polaron) eV. The two high binding energy peaks at the tail are corresponding to the two different positively charges species. The peak at 400.4 eV is attributed to the delocalized radical cations [53] and other component at 401.5 eV is allocated to the positively charges imine cation. C 1s spectra deconvolute into five peaks corresponds to C-C, C-N , C-O,C=O and $\pi \rightarrow \pi^*$ shake-up satellite at 284.2 eV, 285 eV, 286 eV, 287.2 eV and 289.5 eV.[56] The presence of the C-O and C=O components in the spectra indicated about some level of oxidation of the samples. Further, Cl 2p spectra decomposed into four peaks at binding energy of 196.8 eV, 198.3 eV, 200.1 eV and 201.5 eV. The first and third components confirmed the presence of chlorine anions (Cl^-) and covalent bonded chlorine (-Cl) species. In C 1s spectra, smallest peak having highest binding energy observes at the end of the tail indicated about well-doped states.

Table 4.2: The detail of the doping level in the PANI-NW samples are listed below.

Sample	$= N -$	$-NH -$	N^+	N^+/N	σ (S/cm)
PANI-NW	0.21	0.51	0.26	0.26	1.98
PANI-NW-0.1M HCl	0.08	0.60	0.32	0.32	3.14
PANI-NW-0.5 M HCl	0.23	0.30	0.47	0.47	9.8
PANI-NW-1 M HCl	0.02	0.38	0.60	0.60	10.2

The N 1s core level spectra give the information about the doping level in the different samples of PANI. The ratio of N^+/N of different HCl doped PANI-NW samples is shown in the table 4.2. It shows that the protonation level increases from 0.26 to 0.60 when doping of HCl increases from 0 to 1 M. This trend of protonation level follows the electrical conductivity

measurement results of the PANI-NW samples. This increase in protonation level with Increasing the HCl concentration results in enhanced electrical conductivity of PANI-NW.

4.3 Electrical conductivity measurement results

The electrical conductivity of the polyaniline nanowhiskers (PANI-NW) doped with different concentrations of HCl is measured at different temperatures, from 80 to 300 K (as shown in Figure 4.12). The electrical conductivity increases with increasing the temperature for all the samples, but the rate of increase is different for the different HCl-doped samples. The measured electrical conductivities at 300 K for the HCl-doped samples PANI-NW, PANI-NW 0.1 M HCl, PANI-NW 0.5 M HCl, and PANI-NW 1.0 M HCl are 1.94 Scm^{-1}, 3.14 Scm^{-1}, 9.8 Scm^{-1}, and 10.2 Scm^{-1}, respectively. The observed increase in electrical conductivity with the doping concentration could be due to the increase in polaron formation (bands at ~ 480 nm and at ~ 650 nm in Figure 4.6 (c)), as observed from the absorption studies. The electrical conductivity of polyaniline increases up to 10.2 Scm^{-1} for the higher concentration (1.0 M HCl) of the acid doping, which is almost five times higher than that of the pure polyaniline (PANI-NW) electrical conductivity (1.94 Scm^{-1}). However, from Figure 4.12, it is seen that the electrical conductivity of the 0.5 M HCl-doped polyaniline shows a higher value at all temperatures except at 300 K.

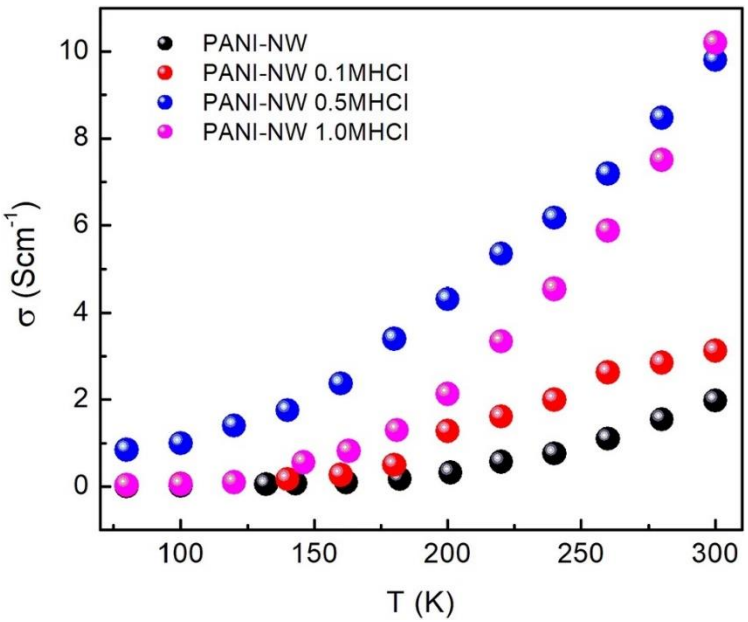

Figure 4.12: Electrical conductivity of the polyaniline nanowhisker samples doped with different concentrations of HCl.

The excess concentration of HCl could lead to structural distortion and that could be the reason for the observed decrease in electrical conductivity beyond the 0.5 M HCl concentration.[22] The maximum electrical conductivity for the sample doped with 0.5 M HCl is due to the increased exciton (polaron/bi-polaron) transition as compared with the other samples, and it is clearly seen from the new polaron band (polaron-π*) observed at 480 nm, and also the intensity of the $\pi - \pi^*$ transition is diminished considerably (see in Figure 4.6(c)). The electrical conductivities of all the samples are compared with the optical bandgap of the different transitions in Table 4.1.

The electrical conductivities of the polyaniline nanofiber samples prepared by interfacial polymerization (IP) with different acid dopants are shown in Figure 4.13. All these samples are prepared in the same conditions, washed with water to remove the excess acids in the sample, and the only difference is dopant acid. The temperature-dependant electrical conductivity results show that the rate of variation is different for different acid-doped polyaniline nanofibers, which is larger for the PNF-HCl sample and smaller for the PNF-CA sample. The electrical conductivity at 300 K for the samples PNF-HCl, PNFCSA, and PNF-CA are 1.75 Scm^{-1} , 1.28 Scm^{-1} , and 0.22 Scm^{-1} , respectively. The observed difference in the electrical

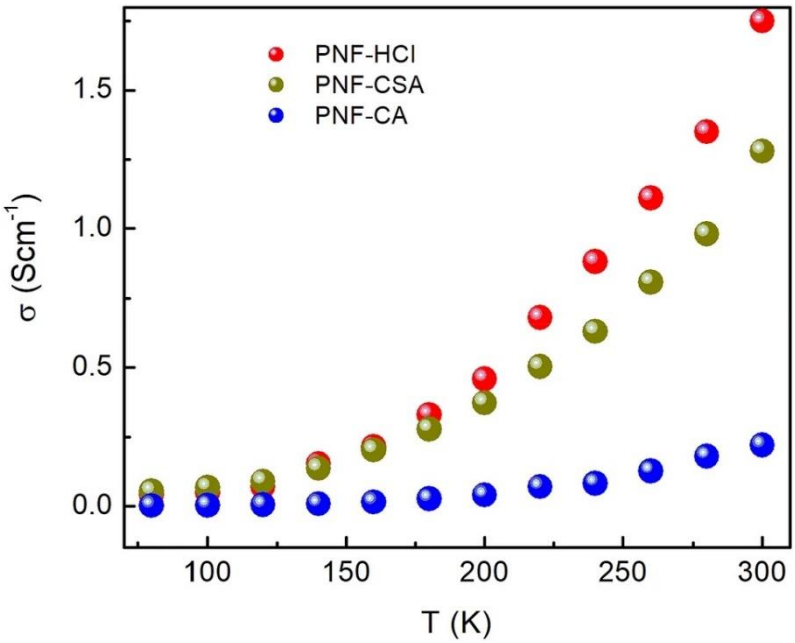

Figure 4.13: Electrical conductivity of polyaniline nanofibers with different acid doping

conductivity could be due to the difference in the band energies of the polymer samples. The electrical conductivity values are in-line with the optical bandgap of the $\pi - \pi^*$ transitions which are 3.03 eV, 3.37 eV, and 3.80 eV for PNF-HCl, PNF-CSA, and PNF-CA samples,

respectively, i.e., the electrical conductivity decreases with increasing the band energy. Similarly, the electrical conductivity values are in-line with the optical band gap of π-polaron transition (> 600 nm) of the samples. The observed lowest electrical conductivity for the PNF-CA (0.22 Scm^{-1}) sample is attributed to the larger bandgap (1.77 eV), and the higher electrical conductivity values for the PNF-HCl (1.75 Scm^{-1}) and PNF-CSA (1.28 Scm^{-1}) samples are attributed to the smaller bandgap (~ 1.55 eV). But the polaron-π* transition for all the samples observed at ~ 480 nm with the optical band gap around ~ 2.4 eV (see Figure 4.8). Moreover, the electrical conductivity is also strongly influenced by the charge carrier mobility at the polymer backbone. From the TEM image (see Figure 4.2), the PNF-CA sample shows more roughness at the surface of the nanofibers as compared to the PNF-HCl and PNF-CSA nanofiber samples. This could be due to the larger CA molecule induce disorder at the surface of the polyaniline nanofibers, and this may be the reason for the observed lowest electrical conductivity (0.22 Scm^{-1}) for the PNF-CA sample [57]. From the above discussion, it is clear

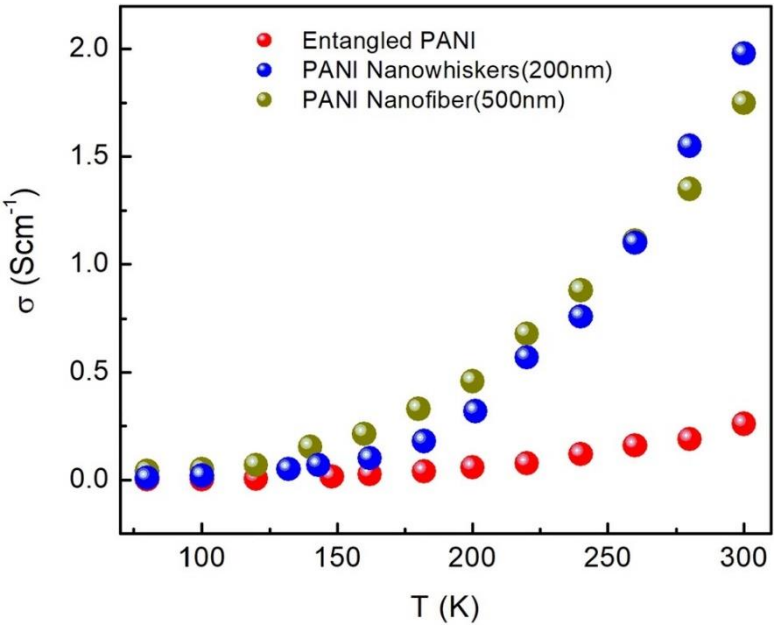

Figure 4.14: Electrical conductivity of polyaniline in different morphologies

that the type of dopant material alters the electronic energy levels which leads to changes in the electrical conductivity.

From the TEM images (see Figure 4.2), it is clear that the simple oxidative polymerization of aniline using APS produces highly entangled polyaniline (PANI-ED) chains, whereas the oxidizing agent APS + $FeCl_3$ produces the nanowhisker (PANI-NW) of length 200 nm and diameter 50 nm. But, the interfacial polymerization produces the nanofibers (PNF-HCl) of ~ 500 nm length and ~ 50 nm diameter. The electrical conductivity of polyaniline samples with

different morphologies, prepared under different synthesis conditions was studied, and the results are shown in Figure 4.14. In all three cases, HCl was used as dopant acid. From the electrical conductivity studies, it is clear that the polyaniline samples PANI-NW (nanowhisker) and PNF-HCl (nanofiber) show electrical conductivities 1.98 Scm^{-1} and 1.75 Scm^{-1}, respectively, which is almost eight times higher than that of the electrical conductivity of the highly entangled polyaniline chains in PANI-ED (0.26 Scm^{-1}) sample. The larger electrical conductivity for the nanowhisker and nanofiber samples could be attributed to the ordered arrangement of polymer chains as compared with the entangled polyaniline chains. The ordered arrangement of the polymer chains in the nanowhisker and nanofiber morphologies promote the charge carrier mobility, and this leads to an increase in electrical conductivity.[25] From the above studies, it is clear that the concentration of the dopant materials and type of the dopant materials changes the electrical properties of the polyaniline. Moreover, making the one-dimensional nanostructures improves the electrical conductivity by increasing the charge carrier mobility, which is one of the prime requirements for the thermoelectrical materials to improve the electrical conductivity without much affecting the Seebeck coefficient.

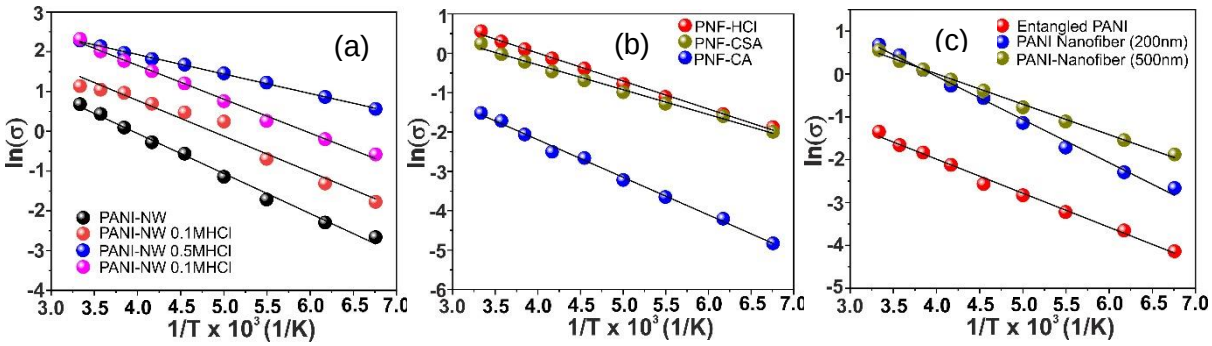

Figure 4.15: Arrhenius plot for (a) PANI-NW and PANI-NW with different HCl concentration (b) PNF with different acid dopants (HCl, CSA, CA) and (c) Entangled PANI, PANI Nanofibers (200nm) and PANI Nanofibers (500nm).

The activation behaviour of the samples are studied using the Arrhenius Equation shown below

$$\sigma = \sigma_0 e^{\frac{-E_g}{k_B T}} \tag{4.1}$$

Where k_B is the Boltzmann's constant and σ_0 represents the value of σ at 1/T =0. The variation of the conductivity σ as a function of 1/T is shown in the Figure 4.15. E_g is the activation energy

of conductivity which is obtained from the slope of the linear portion of the graph log(σ) versus 1/T fits to the Arrhenius Eq 4.1**.** The temperature dependence of conductivity and the follow up arrehenius behaviour indicate that the conduction in polyaniline hybrid ion exchange is predominantly performed by variable range hopping process. The value of activation energy of all the Polyaniline samples is summarized in Table 4.2. The value of activation energy is indicating that the charge carrier has to overcome the same energy barrier while conducting. Thus, the polarons acts as charge carrier hopping from state in all the polymer samples.

4.4 Conclusion

In this chapter, we have studied the effect of the concentration of dopant material, type of dopant material, and the morphology of the polymer on the electrical conductivity of polyaniline. The experimental electrical conductivity results are compared with the electronic transition and optical band gap observed in the absorption spectra. The electrical conductivity of the polyaniline increases from 1.98 to 10.2 Scm^{-1} while increasing the concentration of the dopant acid from 0 to 1.0 M. The observed five-fold increase could be attributed to the generation of polarons in the polymer chain with increasing the acid doping. The absorption spectra and the calculated optical band gap are also in-line with the experimental electrical conductivity results, i.e., the intensity of the $\pi - \pi^*$ band and corresponding optical band gap decreases while the intensity of the polaron band increases with the doping. The electrical conductivity of polyaniline nanofiber doped with different acids show higher conductivity for PNF-HCl (1.75 Scm^{-1}) and PNF-CSA (1.27 Scm^{-1}) samples and lower conductivity for the PNF-CA sample (0.22 Scm^{-1}). The observed lower electrical conductivity for the PNF-CA sample could be due to an increase in the optical band gap in the $\pi - \pi^*$ (3.8 eV) as well as π-polaron (1.77 eV) transition. Moreover, the reduced electrical conductivity in the PNF-CA sample could also be attributed to the reduced charge carrier mobility due to the disordered polyaniline chains at the surface of the nanofibers. The nanowhisker and nanofiber morphology polymer samples show larger electrical conductivity as compared to the entangled polymer chains as larger particles. This could be due to the ordered arrangement of the polymer chains in nanowhiskers and nanofibers improves the charge carrier mobility compared with the entangled polymer chains. Overall, many factors need to be considered for achieving higher electrical conductivity with high charge carrier mobility of the polymers. We hope that our

findings will be useful for the researchers to choose the proper dopants with optimum concentration to achieve high electrical conductivity and high charge carrier mobility in polyaniline for flexible electronics and flexible thermoelectric application.

References:

[1] S. Logothetidis, "Flexible organic electronic devices: Materials, process and applications," *Mater. Sci. Eng. B*, vol. 152, no. 1–3, pp. 96–104, 2008.

[2] Q. Zhang, Y. Sun, W. Xu, and D. Zhu, "Organic thermoelectric materials: emerging green energy materials converting heat to electricity directly and efficiently," *Adv. Mater.*, vol. 26, no. 40, pp. 6829–6851, 2014.

[3] S. Lee *et al.*, "Recent progress in organic thermoelectric materials and devices," *Macromol. Res.*, vol. 28, no. 6, pp. 531–552, 2020.

[4] B. Lüssem, M. Riede, and K. Leo, "Doping of organic semiconductors," *Phys. Status Solidi A*, vol. 210, no. 1, pp. 9–43, 2013.

[5] W. Zhao, J. Ding, Y. Zou, C. Di, and D. Zhu, "Chemical doping of organic semiconductors for thermoelectric applications," *Chem. Soc. Rev.*, vol. 49, no. 20, pp. 7210–7228, 2020.

[6] Y. Du, J. Xu, B. Paul, and P. Eklund, "Flexible thermoelectric materials and devices," *Appl. Mater. Today*, vol. 12, pp. 366–388, 2018.

[7] A. Kausar, "Overview on conducting polymer in energy storage and energy conversion system," *J. Macromol. Sci. Part A*, vol. 54, no. 9, pp. 640–653, 2017.

[8] Y. Wang and X. Jing, "Intrinsically conducting polymers for electromagnetic interference shielding," *Polym. Adv. Technol.*, vol. 16, no. 4, pp. 344–351, 2005.

[9] A. Ramanavičius, A. Ramanavičienė, and A. Malinauskas, "Electrochemical sensors based on conducting polymer—polypyrrole," *Electrochimica Acta*, vol. 51, no. 27, pp. 6025–6037, 2006.

[10] U. Lange, N. V. Roznyatovskaya, and V. M. Mirsky, "Conducting polymers in chemical sensors and arrays," *Anal. Chim. Acta*, vol. 614, no. 1, pp. 1–26, 2008.

[11] H. Bai and G. Shi, "Gas sensors based on conducting polymers," *Sensors*, vol. 7, no. 3, pp. 267–307, 2007.

[12] M. Gerard, A. Chaubey, and B. Malhotra, "Application of conducting polymers to biosensors," *Biosens. Bioelectron.*, vol. 17, no. 5, pp. 345–359, 2002.

[13] K. Kaneto, "Research trends of soft actuators based on electroactive polymers and conducting polymers," 2016, vol. 704, no. 1, p. 012004.

[14] N. F. Attia and K. E. Geckeler, "Polyaniline as a material for hydrogen storage applications," *Macromol. Rapid Commun.*, vol. 34, no. 13, pp. 1043–1055, 2013.

[15] S. Bhadra, D. Khastgir, N. K. Singha, and J. H. Lee, "Progress in preparation, processing and applications of polyaniline," *Prog. Polym. Sci.*, vol. 34, no. 8, pp. 783–810, 2009.

[16] K. Zhang, J. Qiu, and S. Wang, "Thermoelectric properties of PEDOT nanowire/PEDOT hybrids," *Nanoscale*, vol. 8, no. 15, pp. 8033–8041, 2016.

[17] M. Culebras, C. M. Gómez, and A. Cantarero, "Review on polymers for thermoelectric applications," *Materials*, vol. 7, no. 9, pp. 6701–6732, 2014.

[18] M. He, F. Qiu, and Z. Lin, "Energy Environ. Sci. 6, 1352 (2013)".

[19] Y. Sun, C. Di, W. Xu, and D. Zhu, "Advances in n-type organic thermoelectric materials and devices," *Adv. Electron. Mater.*, vol. 5, no. 11, p. 1800825, 2019.

[20] N. Dubey and M. Leclerc, "Conducting polymers: efficient thermoelectric materials," *J. Polym. Sci. Part B Polym. Phys.*, vol. 49, no. 7, pp. 467–475, 2011.

[21] L. M. Cowen, J. Atoyo, M. J. Carnie, D. Baran, and B. C. Schroeder, "Organic materials for thermoelectric energy generation," *ECS J. Solid State Sci. Technol.*, vol. 6, no. 3, p. N3080, 2017.

[22] J. Li, X. Tang, H. Li, Y. Yan, and Q. Zhang, "Synthesis and thermoelectric properties of hydrochloric acid-doped polyaniline," *Synth. Met.*, vol. 160, no. 11–12, pp. 1153–1158, 2010.

[23] E. Holland, S. Pomfret, P. Adams, and A. Monkman, "Conductivity studies of polyaniline doped with CSA," *J. Phys. Condens. Matter*, vol. 8, no. 17, p. 2991, 1996.

[24] H. Anno, M. Hokazono, F. Akagi, M. Hojo, and N. Toshima, "Thermoelectric properties of polyaniline films with different doping concentrations of (±)-10-camphorsulfonic acid," *J. Electron. Mater.*, vol. 42, no. 7, pp. 1346–1351, 2013.

[25] Y. Sun, Z. Wei, W. Xu, and D. Zhu, "A three-in-one improvement in thermoelectric properties of polyaniline brought by nanostructures," *Synth. Met.*, vol. 160, no. 21–22, pp. 2371–2376, 2010.

[26] M. Amrithesh, S. Aravind, S. Jayalekshmi, and R. Jayasree, "Polyaniline doped with orthophosphoric acid—A material with prospects for optoelectronic applications," *J. Alloys Compd.*, vol. 458, no. 1–2, pp. 532–535, 2008.

[27] M. V. Kulkarni, A. K. Viswanath, R. Marimuthu, and T. Seth, "Synthesis and characterization of polyaniline doped with organic acids," *J. Polym. Sci. Part Polym. Chem.*, vol. 42, no. 8, pp. 2043–2049, 2004.

[28] S. Stafström *et al.*, "Polaron lattice in highly conducting polyaniline: Theoretical and optical studies," *Phys. Rev. Lett.*, vol. 59, no. 13, p. 1464, 1987.

[29] Y. Xue, C. Gao, L. Liang, X. Wang, and G. Chen, "Nanostructure controlled construction of high-performance thermoelectric materials of polymers and their composites," *J. Mater. Chem. A*, vol. 6, no. 45, pp. 22381–22390, 2018.

[30] Y. Du, S. Z. Shen, W. Yang, R. Donelson, K. Cai, and P. S. Casey, "Simultaneous increase in conductivity and Seebeck coefficient in a polyaniline/graphene nanosheets thermoelectric nanocomposite," *Synth. Met.*, vol. 161, no. 23–24, pp. 2688–2692, 2012.

[31] J. Sun *et al.*, "Simultaneous increase in seebeck coefficient and conductivity in a doped poly (alkylthiophene) blend with defined density of states," *Macromolecules*, vol. 43, no. 6, pp. 2897–2903, 2010.

[32] E. Song and J.-W. Choi, "Conducting polyaniline nanowire and its applications in chemiresistive sensing," *Nanomaterials*, vol. 3, no. 3, pp. 498–523, 2013.

[33] L. Bach-Toledo, B. M. Hryniewicz, L. F. Marchesi, L. H. Dall'Antonia, M. Vidotti, and F. Wolfart, "Conducting polymers and composites nanowires for energy devices: A brief review," *Mater. Sci. Energy Technol.*, vol. 3, pp. 78–90, 2020.

[34] N. Toshima, "Conductive polymers as a new type of thermoelectric material," 2002, vol. 186, no. 1, pp. 81–86.

[35] G. Liao, Q. Li, and Z. Xu, "The chemical modification of polyaniline with enhanced properties: A review," *Prog. Org. Coat.*, vol. 126, pp. 35–43, 2019.

[36] A. Hussain and A. Kumar, "Electrochemical synthesis and characterization of chloride doped polyaniline," *Bull. Mater. Sci.*, vol. 26, no. 3, pp. 329–334, 2003.

[37] P. Kong *et al.*, "Conjugated HCl-doped polyaniline for photocatalytic oxidative coupling of amines under visible light," *Catal. Sci. Technol.*, vol. 9, no. 3, pp. 753–761, 2019.

[38] F. R. Rangel-Olivares, E. M. Arce-Estrada, and R. Cabrera-Sierra, "Synthesis and characterization of polyaniline-based polymer nanocomposites as anti-corrosion coatings," *Coatings*, vol. 11, no. 6, p. 653, 2021.

[39] M. J. R. Cardoso, M. F. S. Lima, and D. M. Lenz, "Polyaniline synthesized with functionalized sulfonic acids for blends manufacture," *Mater. Res.*, vol. 10, pp. 425–429, 2007.

[40] M. Das, A. Akbar, and D. Sarkar, "Investigation on dielectric properties of polyaniline (PANI) sulphonic acid (SA) composites prepared by interfacial polymerization," *Synth. Met.*, vol. 249, pp. 69–80, 2019.

[41] E. Gomes and M. Oliveira, "Chemical polymerization of aniline in hydrochloric acid (HCl) and formic acid (HCOOH) media. Differences between the two synthesized polyanilines," *Am J Polym Sci*, vol. 2, no. 2, pp. 5–13, 2012.

[42] K. Gupta, P. Jana, and A. Meikap, "Optical and electrical transport properties of polyaniline–silver nanocomposite," *Synth. Met.*, vol. 160, no. 13–14, pp. 1566–1573, 2010.

[43] K. A. Ibrahim, "Synthesis and characterization of polyaniline and poly (aniline-co-o-nitroaniline) using vibrational spectroscopy," *Arab. J. Chem.*, vol. 10, pp. S2668–S2674, 2017.

[44] S. Sinha, S. Bhadra, and D. Khastgir, "Effect of dopant type on the properties of polyaniline," *J. Appl. Polym. Sci.*, vol. 112, no. 5, pp. 3135–3140, 2009.

[45] A. Pron and P. Rannou, "Processible conjugated polymers: from organic semiconductors to organic metals and superconductors," *Prog. Polym. Sci.*, vol. 27, no. 1, pp. 135–190, 2002.

[46] S. Gul and S. Bilal, "Synthesis and characterization of processable polyaniline salts," 2013, vol. 439, no. 1, p. 012002.

[47] M. Scully, M. Petty, and A. Monkman, "Optical properties of polyaniline thin films," *Synth. Met.*, vol. 55, no. 1, pp. 183–187, 1993.

[48] R. Borah, S. Banerjee, and A. Kumar, "Surface functionalization effects on structural, conformational, and optical properties of polyaniline nanofibers," *Synth. Met.*, vol. 197, pp. 225–232, 2014.

[49] W. Huang and A. MacDiarmid, "Optical properties of polyaniline," *Polymer*, vol. 34, no. 9, pp. 1833–1845, 1993.

[50] K. Mamma, K. Siraj, and N. Meka, "Effect on poly (C6H5NH2) emeraldine salt by FeCl3 and KMnO4 as secondary dopants," *Am. J. Polym. Sci. Eng.*, vol. 1, no. 1, pp. 1–13, 2013.

[51] J. Park, D. Bang, K. Jang, S. Haam, J. Yang, and S. Na, "The work function of doped polyaniline nanoparticles observed by Kelvin probe force microscopy," *Nanotechnology*, vol. 23, no. 36, p. 365705, 2012.

[52] D. M. Tigelaar *et al.*, "Role of solvent and secondary doping in polyaniline films doped with chiral camphorsulfonic acid: preparation of a chiral metal," *Chem. Mater.*, vol. 14, no. 3, pp. 1430–1438, 2002.

[53] B. Sreedhar, M. Sairam, D. Chattopadhyay, P. P. Mitra, and D. M. Rao, "Thermal and XPS studies on polyaniline salts prepared by inverted emulsion polymerization," *J. Appl. Polym. Sci.*, vol. 101, no. 1, pp. 499–508, 2006.

[54] M. B. Inoue, K. W. Nebesny, Q. Fernando, and M. Inoue, "X-Ray photoelectron spectroscopy of new soluble polyaniline perchlorates: evidence for the coexistence of polarons and bipolarons," *J. Mater. Chem.*, vol. 1, no. 2, pp. 213–216, 1991.

[55] G. M. Barra, M. E. Leyva, M. M. Gorelova, B. G. Soares, and M. Sens, "X-ray photoelectron spectroscopy and electrical conductivity of polyaniline doped with dodecylbenzenesulfonic acid as a function of the synthetic method," *J. Appl. Polym. Sci.*, vol. 80, no. 4, pp. 556–565, 2001.

[56] S. Golczak, A. Kanciurzewska, M. Fahlman, K. Langer, and J. J. Langer, "Comparative XPS surface study of polyaniline thin films," *Solid State Ion.*, vol. 179, no. 39, pp. 2234–2239, 2008.

[57] M. Khalid, M. A. Tumelero, I. Brandt, V. C. Zoldan, J. J. Acuña, and A. A. Pasa, "Electrical conductivity studies of polyaniline nanotubes doped with different sulfonic acids," *Indian J. Mater. Sci.*, vol. 2013, 2013.

Chapter 5

Effect of light on the conductivity of 2DEG at the oxide interface $LaVO_3/SrTiO_3$ and $EuO/KTaO_3$

5.1 Introduction

The quasi-two-dimensional electron gas (2DEG) at the oxide interface opens new possibilities both for the fundamental and applied physics.[1]–[3] The 2DEG formed between transition metal oxides possesses high mobility and other fascinating properties like magnetism, superconductivity, electric field tuning, planar Hall effect, photoconductivity (PC), etc.[2], [4]–[11] These interesting properties motivates researchers to investigates a number of oxide interfaces like $LaTiO_3/SrTiO_3$ (LTO/STO), $LaGaO_3$/ $SrTiO_3$(LGO/STO), $NdGaO_3$/ $SrTiO_3$ (NGO/STO), etc.[12]–[15] The properties of 2DEG can be tuned using various external stimuli such as magnetic fields, light, stress, electric fields, particle bombardment, etc.[2], [7], [10], [11], [16], [17] Among them, the effect of light on the 2DEG conductivity has attracted considerable interest in optoelectronics applications.[10], [17] The observation of high persistent photoconductivity (PPC), where the material even persists in a higher conductivity state with a large relaxation time after turning the light illumination off, becomes an attractive subject for investigators.[17]–[19] This PPC has shown many applications in holographic memory, phototransistor, photodiode, optical memories, and photodetectors.[17], [20]–[24] This PPC phenomenon is well recognized mainly in semiconductor materials.[20], [25] But the magnitude of the PPC observed in semiconductor materials like silicon membranes, and GaN nanowires at room temperature is very small.[26], [27] Another type of material that manifest persistent photoconductivity is oxides. [28], [29] So, observing the room temperature PPC in

oxides can be very interesting and may open up vast opportunities for the oxides in optoelectronics.[22]

In this chapter, we have shown the effect of visible light illumination on the conducting interface of LVO (5 u.c.)/STO(bulk) and insulating interface LVO (3 u.c.)/STO(bulk) at a different temperature from 76K to 300K under the different wavelength of laser light. The EuO/ KTO interface is the only non-perovskite/perovskite interface. The conductivity at this interface's origin is still unclear; nevertheless, it shows exciting phenomena like Shubnikov-de Hass oscillations, anomalous magnetoresistance, planar Hall effect, PC, etc. [30], [31] These properties motivate us to perform a PC experiment on samples of EuO/KTO (non-perovskite/perovskite) with different intrinsic charge carrier densities at temperatures 76K and 300K under different wavelengths of laser light at different power values.

5.2 Experimental details

We have used the photoconductivity measurement setup discuss in measurement methods section of chapter 2 to measure the sheet resistance of the prepared samples. The schematic of

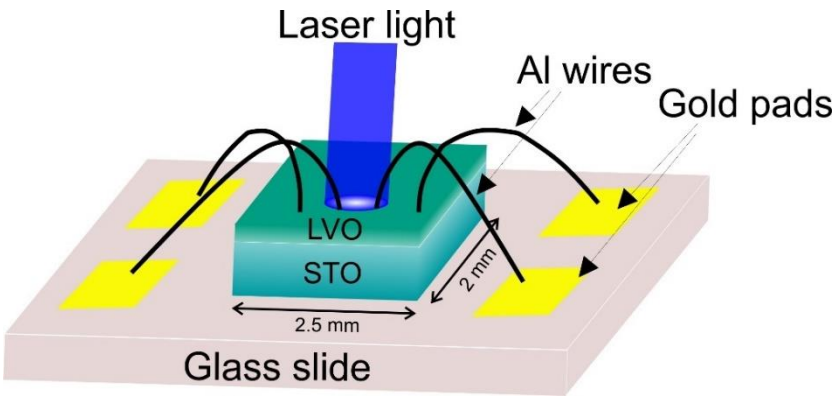

Figure 5.1: The schematic diagram of measurement sample geometry

the device geometry to perform photoconductivity measurement is shown in the Figure 5.1. The ultrasonic wire bonder is used to connect device to four gold pads on the glass slide. We made four gold pads on the cornors of the glass slide using EXCEL e-beam deposition process. A hard mask has been used to made gold pads of specific size (2mm x 2mm) and position on

the glass slide as shown in the schematic Figure 5.1. Four probe I-V measurement are performed for sheet resistance (ρ_{2D}) measurement. In both experiments we have used two lasers of different wavelengths one is 405 nm (blue) and other is 532 nm (green). In the schematic LVO is deposited on the STO substrate, similar sample geometry is used for the EuO/KTO samples.

5.3 Photoconductivity measurement results on LVO/STO

We choose two different interface to investigate the photoconductivity behavior of the 2DEG at the interface, one is LVO(3 u.c.)/STO and other is LVO(5 u.c.)/STO. First, we check the transport properties of the LVO(3 u.c.)/STO insulating sample in the absence and presence of blue light (405 nm) as shown in the Figure 5.2. The graph shows that in the absence of the light or in dark interface behave as an insulator but under the blue light illumination the sample shows a transition from insulator to metal at 220 K. This type of behavior has also been observed in the LAO/STO interface.[32]

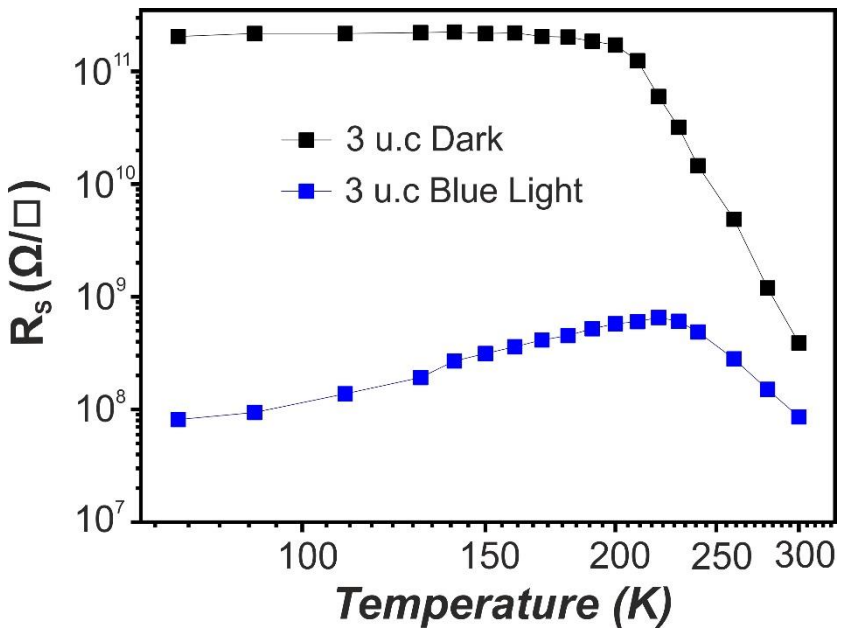

Figure 5.2: Sheet resistance of the LVO (3 u.c.)/STO interface as a function of the temperature in the absence and presence of blue (405 nm) laser light at constant power of 75 mW. Blue color square represents data in the presence of light and black square in the dark.

Further, we study the time dependent change in resistance or photo response for both of the sample under the blue (405 nm) and green (532 nm) at different temperatures from 76 K to 300K. First for the LVO(3 u.c.)/STO sample, we have plotted the percentage change in resistance of the sample in the presence of the light as a function of time and the percentage change in resistance ($\delta R\,\%$) is defined as $\delta R\,\% = ((R(t)-R_D)/R_D)$, where R(t) is the resistance at a time t and R_D is the initial value of the resistance in the dark or in the absence of the light. Before start the experiment, samples kept in the dark place and wait until the resistance of the sample becomes constant. After that a blue or green laser which is placed at a constant distance (40 cm) from the sample having power of 75 mW is illuminated on the sample for the 5 min and continuously measure the resistance as a function of time. After 5 minutes, the laser light is turned off but measured resistance continuously as a function of time as shown in the Figure 5.3. The same process is repeated twice at different fixed temperature between 76 K to 300K. In the Figure 5.3(a and b), the data for the change in the resistance as function of

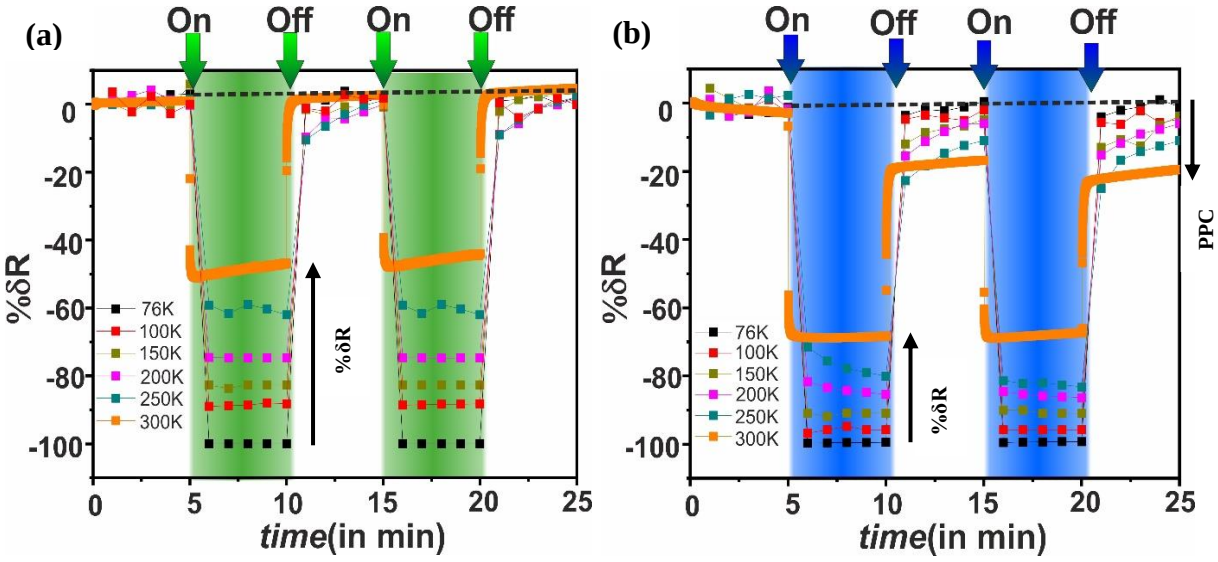

Figure 5.3: Percentage change in resistance with time (a) at 76 K, 100K, 150K, 200K, 250K, and 300K under laser light (532 nm) and (b) at 76 K, 100K, 150K, 200K, 250K, and 300K 3 under blue light (405 nm) for insulating (LVO (3 u.c.)/STO) sample.

time at 76 K, 100K, 150K, 200K, 250K, and 300K under 532 nm(green) and 405 nm (blue) laser light, respectively for the insulating sample is plotted. Similarly, we have study the time dependent photo response for the LVO(5 u.c.)/STO sample and plotted the percentage change in resistance as a function of time at 76 K, 100K, 150K, 200K, 250K, and 300K under 532 nm (green) and 405 nm (blue) laser light respectively is shown in the Figure 5.4. The power of the both lasers are set at same value equal to 75 mW.

Figure 5.3 (a) shows the photoconductivity behavior of the LVO (3 u.c.)/STO interface under the presence of 532 nm laser light ar different temperature between 76K to 300K. This graph suggest that the magnitude of the change in resistance or transient photoconductivity (TPC: no persistent photoconductivty) increases as the temperature increases from 300K to 76 K. But there is no PPC observed in that temperature range. In Figure 5.3 (b) shows the photoconductivity behavior of the LVO (3 u.c.)/STO interface under the 405 nm laser light. This plot clearly shows that the percentage change in resistance increase as we go from 300 K to 76 K but the persistent photoconductivity increases as temperature increases from 76 K to

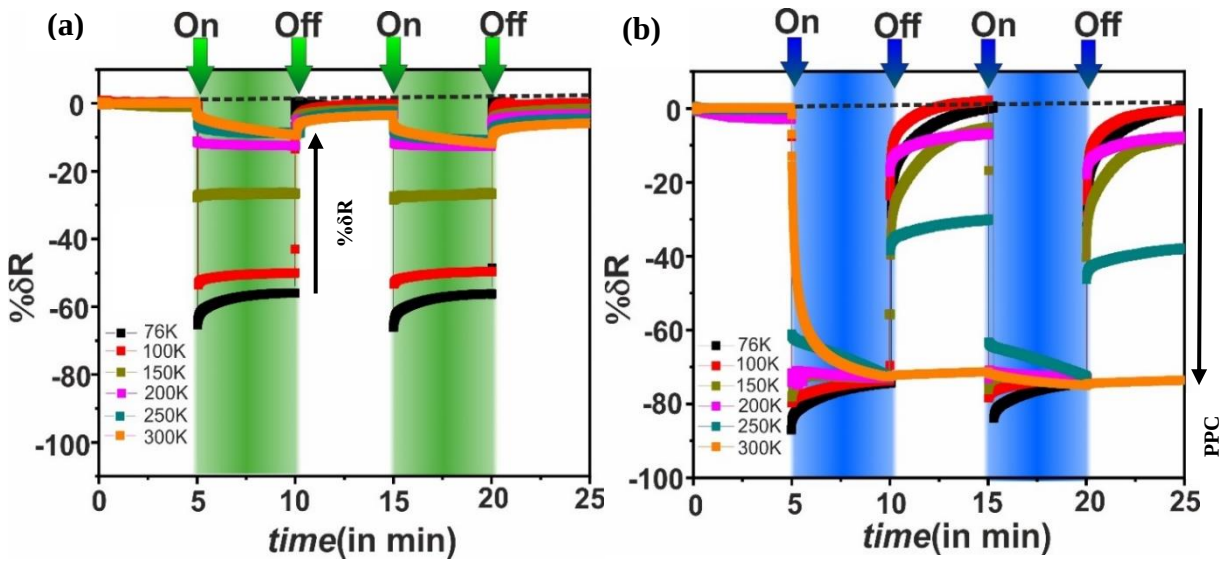

Figure 5.4: Percentage change in resistance with time (a) at 76 K, 100K, 150K, 200K, 250K, and 300K under green laser light (532 nm) and (b) at 76 K, 100K, 150K, 200K, 250K, and 300K under blue light (405 nm) for conducting (LVO (5 u.c.)/STO) sample.

300 K. After compairing both wavelengths, 3 u.c. sample shows persistent photoconductivity only in the presence of 405 nm laser light and change in percentage resistance is almost same for both lasers at 76 k but more change at 300K for the blue laser light.

The effect of 532 nm laser on the 2DEG conductivity at the LVO (5 u.c.)/STO interface is shown in the Fig. 5.4 (a) at different temperatures. The δR % decrease as temperature increase from 76 K to 300 K but the amount of PPC increases with increase in temperature. In case of green the maximum amount of PPC observed at 300K is 8%. On the other hand, in the presence of 405 nm laser light the δR % is almost same at all the temperatures but the PPC increases with increase in temperature and maximum PPC is ~ 72 %. When we compare both samples

then insulating (3 u.c.) samples shows large %δR as compare to conducting sample in the presence of 405 nm and 532 nm light at all the temperatures. But conducting sample shows large PPC as compare to the insulating sample under both laser lights. Further, the conducting interface in Figure 5.5 shows the decay of the induced photoconductivity in the absence of light is quite slow and even after 24 hours these is still 8% persistent photoconductivity is present in the sample. This type of property of the conducting interface consistent with the other reports by Huijben et al.[33] and Tebano et al.[17] for the LAO/STO interface.

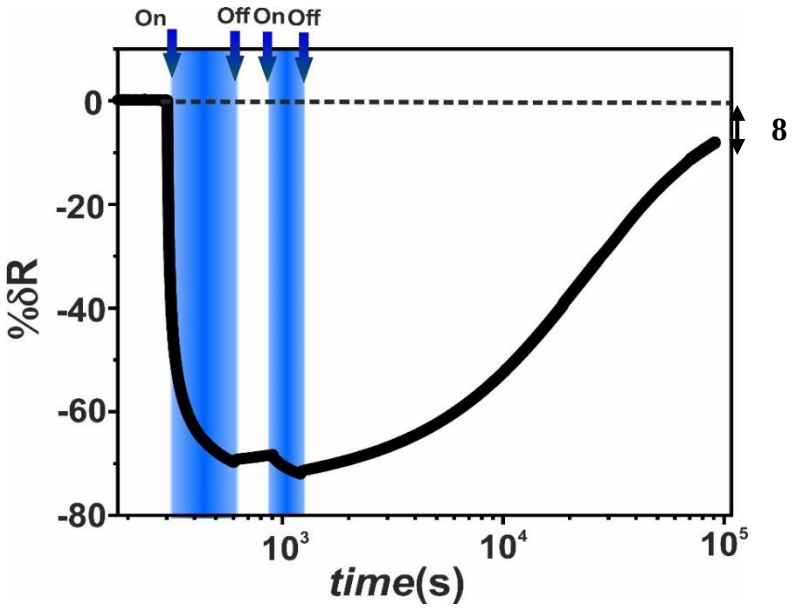

Figure 5.5: The decay of the induced photoconductivity in the dark after the blue light illumination on the LVO (5 u.c.)/STO sample. The decay is extremely slow and even after 24 hours sample persists in low resistance state.

5.4 Photoconductivity measurement results on EuO/KTO

In this work we choose two conducting (nonperovskite/perovskite) EuO/KTO interfaces S2 and S8 having different charge carrier densities. The value of charge carrier density of the sample S2 and S8 are $(1.5 \pm 0.016) \times 10^{13}$ cm^{-2} and $(1.4 \pm 0.012) \times 10^{14}$ cm^{-2}, respectively. First, we have investigated the photoresponce behavoir of the sample S2 under the illumination of the 405 nm and 532 nm laser light with different power values at two fixed

temperatures 76 K and 300 K. Before the start of experiment both samples kept in the dark place until the resistance values becomes constant. Then the laser light of known wavelength was shined on the sample from the fixed distance (40 cm).

The photoresponse data of the sample S2 under green and blue laser light at fixed temperature 300K and 76K are shown in the Figure 5.6 (a and b) and Figure 5.6 (c and d) respectively. Here also data plotted in terms of change in resistance (δR %) as a function of time. The laser kept on and off for 5 min in 2 cycles as shown in Figure 5.6 and continuously monitor the resistance of the sample S2. Similarly, we have measured and plotted the photoconductivity behavior of the sample S8 under green and blue light at constant temperature 300K and 76 K, which are shown in Figure 5.7.

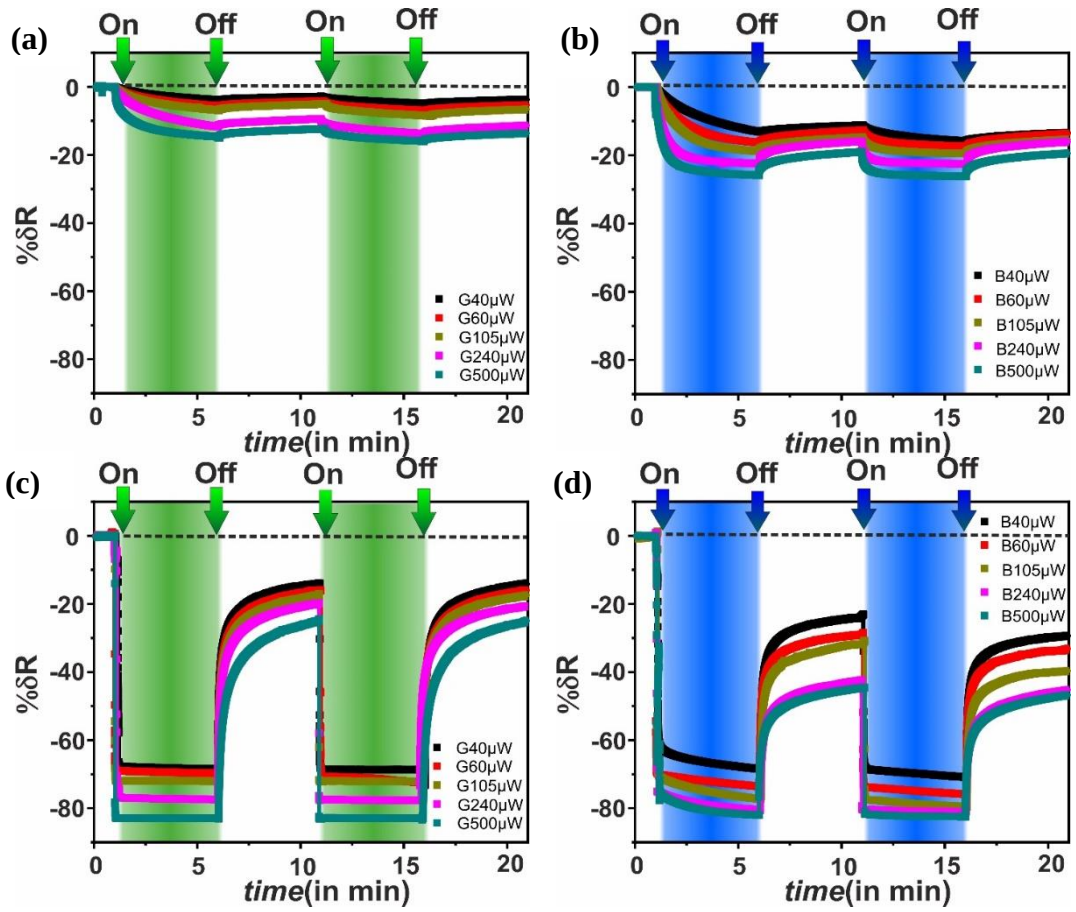

Figure 5.6: Percentage change in resistance with time (a and b) under 532 nm laser light and 405 nm laser light respectively with different power values of 40μW, 60μW, 105μW, 240μW, and 500 μW at a constant temperature of 300 K (c and d) under 532 nm laser light and 405 nm laser light respectively with different power values of 40μW, 60μW, 105μW, 240μW, and 500 μW at a constant temperature of 76 K of sample S2.

A significant amount of PC (~80%) observed in case of sample S2 under very low power (500μW) of blue light and this might have an important technological application. Figure 5.8 shows the varation of %δR and %PPC as a function of laser power under both laser light for both the samples S2 and S8. Figure 5.8 (a and b) at 300K shows that %δR and %PPC is large for blue light as compared to green and the change is large for the sample S2 under both lights as compared to high chagre carrier density sample S8. Similar trend follows in the Figure 5.8 (c and d) at temperature 76K. When we compared the measurement data of %δR and %PPC at 76K and 300K then it shows that the both samples have higher %δR and %PPC at 76 K.

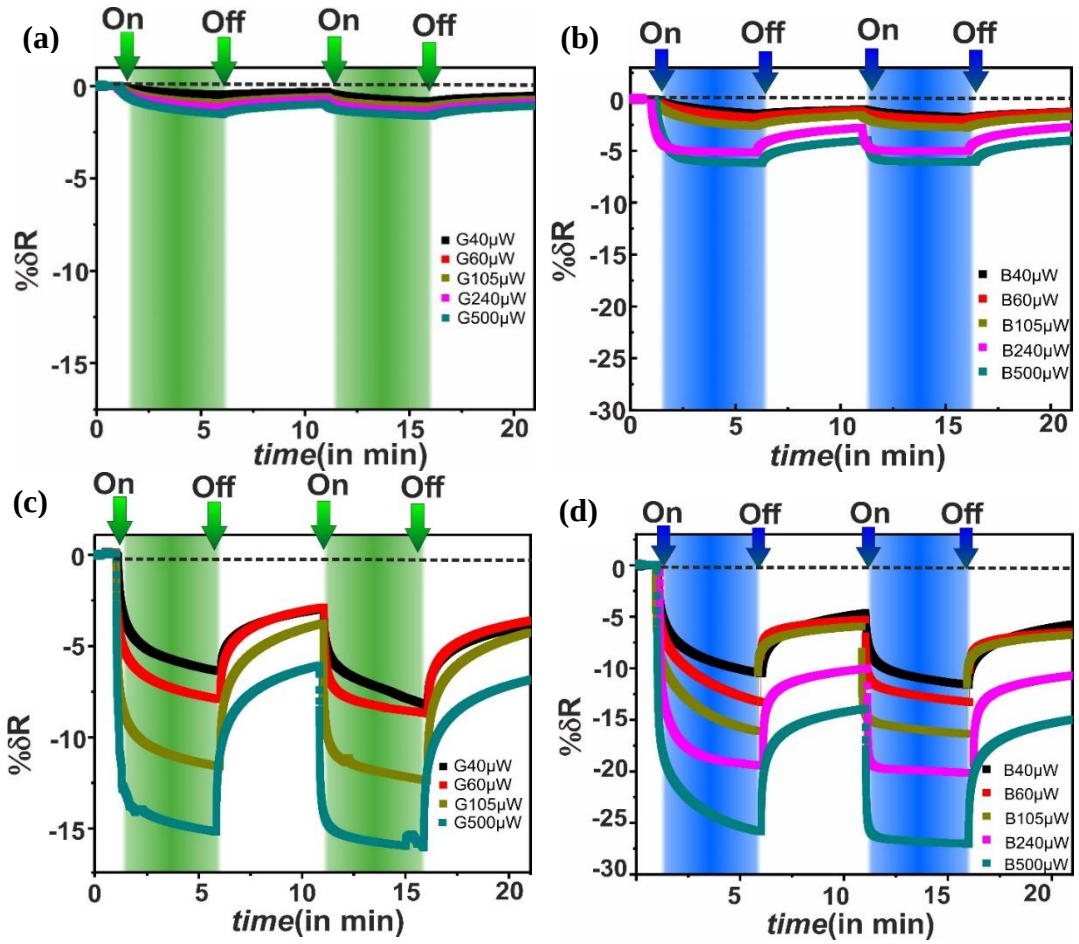

Figure 5.7: Percentage change in resistance with time (a and b) under 532 nm laser light and 405 nm laser light respectively with different power values of 40μW, 60μW, 105μW, 240μW, and 500 μW at a constant temperature of 300 K (c and d) under 532 nm laser light and 405 nm laser light respectively with different power values of 40μW, 60μW, 105μW, 240μW, and 500 μW at a constant temperature of 76 K of sample S8.

Both samples possess PPC at both 300K and 76K under green and blue light laser. As the sample S2 has more PPC as compare to S8 at both temperatures under green and blue light so it reveals that PPC decreases with increase increase in carrier density of 2DEG at the interface. The large PPC and large photoconductivity under 405 nm light compare to 532 nm.This could be because 405 nm laser light has energy approximately similar to the KTO band gap (~3.5 eV) and also larger than the EuO band gap (~1.1 eV). So the electrons from both the valence band of KTO as well as from the valence band of EuO are excited to the interface to increase the photoconductivity.

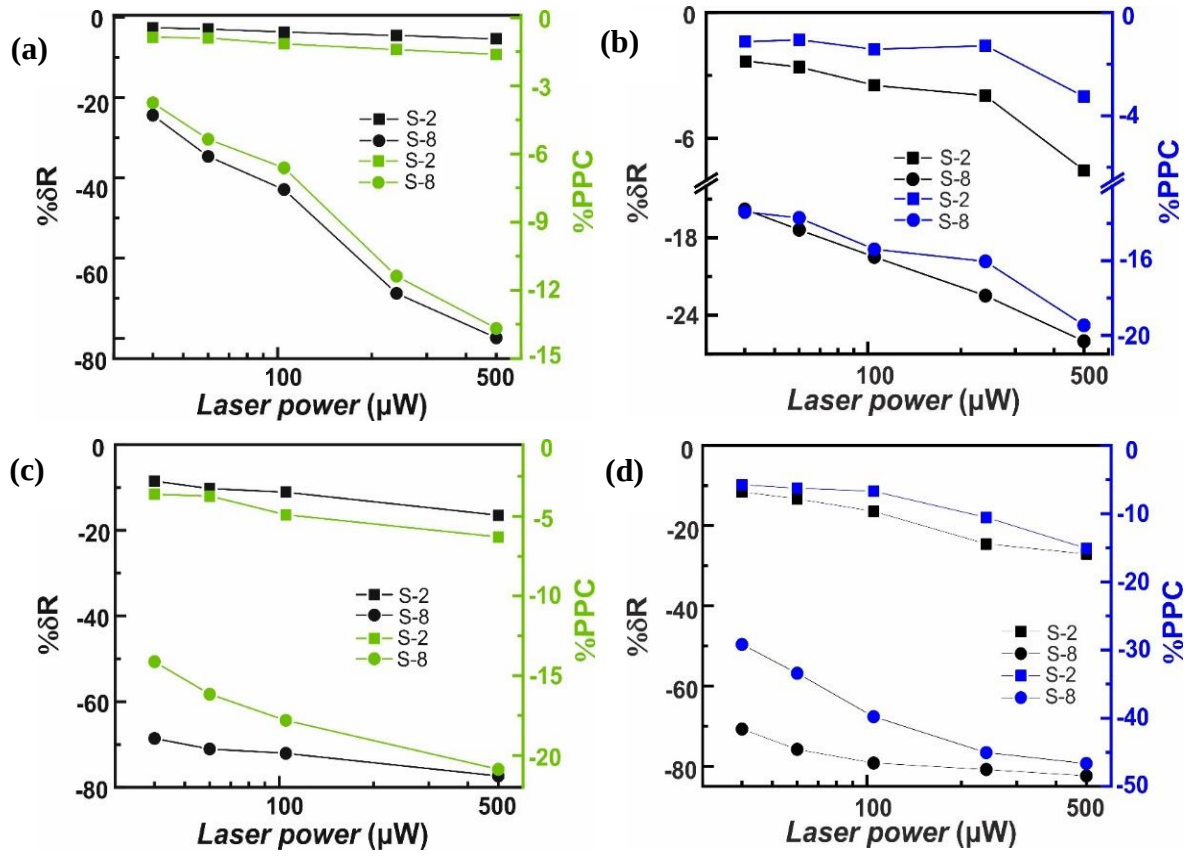

Figure 5.8: The variation of percentage change in resistance and percentage change in PPC as a function of laser light power (a and b) under 532 nm and 405 nm laser light illumination at 300K, respectively and (c and d) under 532 nm and 405 nm laser light illumination at 76K, respectively.

5.5 Conclusion

In conclusion, we have checked the effect of light on the LVO/STO and EuO/KTO interfaces. For LVO(3 u.c.)/STO interface, at low temperature (76K) a light induced insulator to metal transition has been observed with ∼3 orders of resistance change. For the LVO(5 u.c.)/STO interface, PPC state achieve at all temperatures within the range of 76K to 300K in the presence of blue laser light. A transition from transient photoconductivity state to persistent photoconductivity state has been observed at temperature ∼ 200 K under the 532 nm light illumination. Unlike insulating interface of LAO/STO, we have observed PPC state above 150 K under 405 nm light illumination. Conducting LVO (5 u.c.)/STO interface persists in low resistance state in the dark place even after 24 hrs. Further, we found the conducting interface of EuO/KTO shows a large PPC and PC under minimal power blue laser light and lower carrier density the higher the effect is. The wavelength of light and temperature in photoconductivity effect to realize PPC or TPC. This will encourage further investigation on the photo response and persistent current of oxide interface. Our results give an important clue to design future generation solar cell and holographic storage media.

References:

[1] A. Ohtomo and H. Hwang, "A high-mobility electron gas at the LaAlO3/SrTiO3 heterointerface," *Nature*, vol. 427, no. 6973, pp. 423–426, 2004.

[2] S. Thiel, G. Hammerl, A. Schmehl, C. W. Schneider, and J. Mannhart, "Tunable quasi-two-dimensional electron gases in oxide heterostructures," *Science*, vol. 313, no. 5795, pp. 1942–1945, 2006.

[3] J. Mannhart and D. G. Schlom, "Oxide interfaces—an opportunity for electronics," *Science*, vol. 327, no. 5973, pp. 1607–1611, 2010.

[4] H. Y. Hwang, Y. Iwasa, M. Kawasaki, B. Keimer, N. Nagaosa, and Y. Tokura, "Emergent phenomena at oxide interfaces," *Nat. Mater.*, vol. 11, no. 2, pp. 103–113, 2012.

[5] B. Förg, C. Richter, and J. Mannhart, "Field-effect devices utilizing LaAlO3-SrTiO3 interfaces," *Appl. Phys. Lett.*, vol. 100, no. 5, p. 053506, 2012.

[6] N. Reyren *et al.*, "Superconducting interfaces between insulating oxides," *Science*, vol. 317, no. 5842, pp. 1196–1199, 2007.

[7] A. Caviglia *et al.*, "Electric field control of the LaAlO3/SrTiO3 interface ground state," *Nature*, vol. 456, no. 7222, pp. 624–627, 2008.

[8] A. Caviglia, M. Gabay, S. Gariglio, N. Reyren, C. Cancellieri, and J.-M. Triscone, "Tunable Rashba spin-orbit interaction at oxide interfaces," *Phys. Rev. Lett.*, vol. 104, no. 12, p. 126803, 2010.

[9] J. A. Bert *et al.*, "Direct imaging of the coexistence of ferromagnetism and superconductivity at the LaAlO3/SrTiO3 interface," *Nat. Phys.*, vol. 7, no. 10, pp. 767–771, 2011.

[10] Y. Lei *et al.*, "Visible-light-enhanced gating effect at the LaAlO3/SrTiO3 interface," *Nat. Commun.*, vol. 5, no. 1, pp. 1–7, 2014.

[11] Y. Xie, Y. Hikita, C. Bell, and H. Y. Hwang, "Control of electronic conduction at an oxide heterointerface using surface polar adsorbates," *Nat. Commun.*, vol. 2, no. 1, pp. 1–5, 2011.

[12] Y. Hotta, T. Susaki, and H. Hwang, "Polar discontinuity doping of the LaVO 3/SrTiO 3 interface," *Phys. Rev. Lett.*, vol. 99, no. 23, p. 236805, 2007.

[13] R. Tomar, R. M. Varma, N. Kumar, D. Sarma, D. Maryenko, and S. Chakraverty, "Conducting LaVO3/SrTiO3 Interface: Is Cationic Stoichiometry Mandatory?," *Adv. Mater. Interfaces*, vol. 7, no. 6, p. 1900941, 2020.

[14] E. Jin *et al.*, "A high density two-dimensional electron gas in an oxide heterostructure on Si (001)," *APL Mater.*, vol. 2, no. 11, p. 116109, 2014.

[15] P. Perna *et al.*, "Conducting interfaces between band insulating oxides: The LaGaO 3/SrTiO 3 heterostructure," *Appl. Phys. Lett.*, vol. 97, no. 15, p. 152111, 2010.

[16] Y. Chen, J. Zhao, J. Sun, N. Pryds, and B. Shen, "Resistance switching at the interface of LaAlO 3/SrTiO 3," *Appl. Phys. Lett.*, vol. 97, no. 12, p. 123102, 2010.

[17] A. Tebano, E. Fabbri, D. Pergolesi, G. Balestrino, and E. Traversa, "Room-temperature giant persistent photoconductivity in SrTiO3/LaAlO3 heterostructures," *Acs Nano*, vol. 6, no. 2, pp. 1278–1283, 2012.

[18] M. C. Tarun, F. A. Selim, and M. D. McCluskey, "Persistent photoconductivity in strontium titanate," *Phys. Rev. Lett.*, vol. 111, no. 18, p. 187403, 2013.

[19] E. Di Gennaro *et al.*, "Persistent photoconductivity in 2D electron gases at different oxide interfaces," *Adv. Opt. Mater.*, vol. 1, no. 11, pp. 834–843, 2013.

[20] T. P. Saragi, R. Pudzich, T. Fuhrmann-Lieker, and J. Salbeck, "Ultraviolet-sensitive field-effect transistor utilized amorphous thin films of organic donor/acceptor dyad," *Appl. Phys. Lett.*, vol. 90, no. 14, p. 143514, 2007.

[21] M. Kim *et al.*, "Flexible organic phototransistors based on a combination of printing methods," *Org. Electron.*, vol. 15, no. 11, pp. 2677–2684, 2014.

[22] H.-L. Lu *et al.*, "Reversible insulator-metal transition of LaAlO3/SrTiO3 interface for nonvolatile memory," *Sci. Rep.*, vol. 3, no. 1, pp. 1–6, 2013.

[23] S. Jeon *et al.*, "Gated three-terminal device architecture to eliminate persistent photoconductivity in oxide semiconductor photosensor arrays," *Nat. Mater.*, vol. 11, no. 4, pp. 301–305, 2012.

[24] A. Rastogi and R. Budhani, "Solar blind photoconductivity in three-terminal devices of LaAlO 3/SrTiO 3 heterostructures," *Opt. Lett.*, vol. 37, no. 3, pp. 317–319, 2012.

[25] A. Hamed and H. Fritzsche, "Persistent photoconductance in a-Si: H/a-SiNx: H multilayers," *Philos. Mag. B*, vol. 63, no. 1, pp. 33–46, 1991.

[26] P. Feng, I. Mönch, S. Harazim, G. Huang, Y. Mei, and O. G. Schmidt, "Giant persistent photoconductivity in rough silicon nanomembranes," *Nano Lett.*, vol. 9, no. 10, pp. 3453–3459, 2009.

[27] R. Calarco *et al.*, "Size-dependent photoconductivity in MBE-grown GaN− nanowires," *Nano Lett.*, vol. 5, no. 5, pp. 981–984, 2005.

[28] J. Reemts and A. Kittel, “Persistent photoconductivity in highly porous ZnO films,” *J. Appl. Phys.*, vol. 101, no. 1, p. 013709, 2007.

[29] A. Dixit *et al.*, “Robust room temperature persistent photoconductivity in polycrystalline indium oxide films,” *Appl. Phys. Lett.*, vol. 94, no. 25, p. 252105, 2009.

[30] S. Goyal, R. Tomar, and S. Chakraverty, “Photodynamics Study of KTaO3-Based Conducting Interfaces,” *ACS Appl. Electron. Mater.*, vol. 3, no. 2, pp. 905–911, 2021.

[31] N. Kumar *et al.*, “Observation of Shubnikov–de Haas Oscillations, Planar Hall Effect, and Anisotropic Magnetoresistance at the Conducting Interface of EuO–KTaO3,” *Adv. Quantum Technol.*, vol. 4, no. 1, p. 2000081, 2021.

[32] Y. Lei and J. Sun, “Visible light illumination-induced phase transition to the intermediate states between the metallic and insulating states for the LaAlO3/SrTiO3 interfaces,” *Appl. Phys. Lett.*, vol. 105, no. 24, p. 241601, 2014.

[33] M. Huijben, A. Brinkman, G. Koster, G. Rijnders, H. Hilgenkamp, and D. H. Blank, “Structure–property relation of SrTiO3/LaAlO3 interfaces,” *Adv. Mater.*, vol. 21, no. 17, pp. 1665–1677, 2009.

Chapter 6

Summary and future perspectives

6.1 Summary

In this thesis research work, we have worked on the thermal, electrical, and photoconductivity investigations of nanomaterials and explored the effect of surface or interface on the performance of many potential devices. In chapter 1, we have briefly discussed nanofluids and their importance in various heat transfer applications. We have presented a thorough study of the effect of the multiple parameters of the nanofluids on thermal conductivity enhancement. In addition, we have described the significant discrepancy in nanofluids' experimental thermal conductivity results due to the ignorance of some specific parameters in most of the reports. We have also given an overview of the different thermal conductivity, electrical conductivity, and photoconductivity measurement techniques used by various investigators efficiently to reveal the thermal and transport properties. The literature survey found that the transient hot wire method is the easiest and most preferred among the present thermal conductivity measurement technique. For electrical and photoconductivity measurement, the researchers generally employ Van der Pauw and four-point probe methods. In chapter 2, we have briefly discussed the different characterization techniques such as TEM, XRD, TGA, IR spectroscopy, and UV-VIS-NIR spectroscopy used to perform the thesis work. We have also given a detailed description and working of the homemade transient hot wire method, Van der Pauw, and four-point probe method in the measurement methods section of the second chapter. These measurement methods are used to carry out all the nanomaterials' thermal and electrical transport investigations.

In the next chapter, we have investigated the thermal conductivity of the iron oxide nanoparticles dispersed in water and toluene at different weight percentages using the

calibrated homemade transient hot wire measurement setup. The water-based polar nanofluids show a deterioration in thermal conductivity with an increase in the weight percentage of iron oxide nanoparticles. This deterioration is further enhanced with an increase in the amount of the surfactant in the nanofluids is confirmed by the TGA analysis. On the other hand, toluene-based nonpolar nanofluid shows an enhancement in the thermal conductivity with an increase in the weight percentages of nanoparticles. Different surfactants have been used in both nanofluids to suspend the iron oxide nanoparticles. This indicates that the type, as well as the amount of the surfactant, plays an essential role in controlling the thermal transport behavior of the nanofluids. In addition, the thermal conductivity of iron oxide@CNF nanohybrids is investigated using the homemade THW measurement technique for thermal insulation applications. Iron oxide-2% shows the lowest thermal conductivity value, 0.0245 W/mK, which is lower than the air thermal conductivity at room temperature. The reduction in thermal conductivity is explained based on fibril-fibril interaction and phonon surface scattering from the CNF aerogels.

Further in our subsequent work, we have investigated the electrical conductivity of the polyaniline with different types of dopants (HCl, CSA, and CA) as well as by varying the concentration of a dopant (HCl) from 80K to 300K. All the electrical transport measurements were carried out using the Van der Pauw technique. The enhancement in the electrical conductivity has been observed from 1.94 S/cm to 10.2 S/cm with increasing the HCl concentration from 0 to 1 M as a dopant. Electrical conductivity enhancement results are consistent with the absorption band gap studies. The formation of the polaron band in the polymer chains could be contributed to the five-fold enhancement of electrical conductivity. The electrical conductivity of the polyaniline nanofibers doped with different acids is in the order HCl > CSA > CA. The lowest electrical conductivity of the CA-doped polyaniline nanofibers could be due to the irregular polyaniline chains on the surface of the nanofibers, which further affects the charge carrier mobility. Different synthesis process leads to the formation of different morphologies, which further affects the electrical conductivity of the polyaniline. The observed higher electrical conductivity of polyaniline nanowhisker and polyaniline nanofibers compared to pure polyaniline could be due to higher charge mobility from highly ordered polymer chains.

In the following work, we explored the effect of visible light illumination on the conductivity of 2DEG at two different types of interfaces: LVO/STO and EuO/KTO. The LVO (3 u.c.)/STO

interface shows an insulator to metal transition under 405 nm laser light illumination. Conducting LVO/STO interface shows persistent photoconductivity under the 405 nm laser light at all the temperature values, but under 532 nm illumination, it shows the persistent photocurrent only above 150K. For insulating LVO/STO interface, PPC increases as the temperature increases from 76K to 300K under 405 nm light. Still, there is no persistent current under 532 nm light at all the temperature values. The conducting interface shows a maximum PPC of ~72%, which decays very slowly even after 24 hr; an 8% PPC is present in the sample. Further, we have also performed PC measurements on the two EuO/KTO interfaces having different charge carrier densities. The sample having high charge carrier density shows less effect of the light on the conductivity of 2DEG at the interface. The less conducting sample shows large PPC and PC under 405 nm light with the power of 500μW at 76K.

6.2 Future perspective

This thesis work discusses the effect of the different surfactants and base fluids on the nanofluids' thermal conductivity. However, this work is restricted to a few surfactants, solvents, and nanoparticles. The shape and the size of the nanoparticles are also limited in this thesis work. Toluene and water are used as based fluids with oleic acid and citric acid as surfactants to suspend magnetite nanoparticles. More studies can be carried out using different surfactants and solvents to understand the compatibility, dispersibility, interfacial effects, and the role of the particle-fluid interface on the heat transfer capability of the nanofluids. The thermal conductivity measurement studies with nanoparticles of different morphologies can enlighten the various factors that affect the thermal conductivity of nanofluids because all thermal interactions occur on the nanoparticle's surface in the nanofluids.

The enhancement in electrical conductivity of polyaniline with different dopant concentrations is discussed. This study gives an idea of the type and amount of dopant to enhance the conductivity of polyaniline up to the desired level. The morphology of the polyaniline improves the electrical conductivity without changing carrier concentration leading to the possibility of flexible thermoelectrical applications. The conducting PANI-based nanocomposite represents a new area of quantum dots where promising results and unresolved technology challenges call for deeper study and developed research.

The oxide heterostructures have promising potential for future generation optoelectronic devices due to their tunable photoresponse behavior. This thesis work discusses the effect of light as a function of temperature for the LVO/STO and EuO/KTO heterostructure. But to understand the intrinsic mechanism of persistent photoconductivity and transient photoconductivity as a function of temperature, a detailed theoretical study is required. We have used wavelengths in visible regions in this study up to max power of 75 mW. High-energy lasers with an extensive power range may further improve the persistent photoconductivity. Carrier density-dependent photoconductivity of EuO/KTO is discussed, which is non-perovskite/perovskite oxide heterostructure. The comparison of photoresponse with LVO/STO reveals that the thin film's structural properties also significantly affect the photoresponse behavior. So a large variety of combinations of perovskite/perovskite and non-perovskite/perovskite oxide heterostructures opens a door for enhanced electronics devices.

List of publications:

(A) Publications included in the thesis

1. **A. Singh**, R. Lenin, N. K. Bari, C. Bakli, and C. Bera, *Mechanistic Insights into Surface Contribution towards Heat Transfer in a Nanofluid*, Nanoscale Adv. **2**, 3507 (2020).
2. R. Lenin, **A. Singh**, and C. Bera, *Effect of Dopants and Morphology on the Electrical Properties of Polyaniline for Various Applications*, J. Mater. Sci. Mater. Electron. **32**, 24710
3. S. Goyal, **A. Singh**, R. Tomar, R. Kaur, C. Bera, and S. Chakraverty, *Persistent Photoconductivity at LaVO3–SrTiO3 Interface*, Solid State Commun. **316**, 113930 (2020).
4. S. Goyal, **A. Singh**, R. Tomar, C. Bera, and S. Chakraverty, *Tuning the Electronic Properties of 2DEG at Oxide Interface*, in Vol. 2265 (AIP Publishing LLC, 2020), p. 030275.
5. M. Dumen, **A. Singh**, S. Goyal, C. Bera, and S. Chakraverty, *Photoconductivity of the EuO–KTO Interface: Effect of Intrinsic Carrier Density and Temperature*, J. Phys. Chem. C **125**, 15510 (2021).
6. S. Sen, **A. Singh**, K. Kailasam, C. Bera and S.Roy, *Biomass-derived nano fibrillar cellulose and iron oxide-based nanohybrids for thermal insulation application*. Nanoscale Advances (2022)**.**

(B) Publications not included in the thesis

1. R. Lenin, **A. Singh**, and C. Bera, *Role of Nanoparticle Interaction in Magnetic Heating*, MRS Commun. **9**, 1034 (2019).
2. S. Sen, **A. Singh**, C. Bera, S. Roy, and K. Kailasam, *Recent Developments in Biomass Derived Cellulose Aerogel Materials for Thermal Insulation Application: A Review*, Cellulose 1 (2022).
3. D. Rani, **A. Singh**, R. Ladhi, L. Singla, A. R. Choudhury, K. K. Bhasin, C. Bera, and M. Singh, *Nanochannel Mediated Electrical and Photoconductivity of Metal-Organic Nanotubes,* ACS Sustain. Chem. Eng. (2022)

Appendix

Uncertainty analysis of the Transient hot wire method:

The main sources of the non-measurement errors cause differences between the real conditions and the assumptions of the analytical model i.e., that the heating wire has a finite non-zero diameter and the real heat capacity, that there is a thermal barrier between the wire and the sample, that the sample and the wire have finite dimensions and that the heat exchange between the sample surface may occur there. The random component of the uncertainty is evaluated statistically by analyzing the repeated measurement.

Table 6.1: Results of water thermal conductivity measurement

Sr. No.	**k ($Wm^{-1}K^{-1}$)**
1	0.590
2	0.595
3	0.588
4	0.599
5	0.591
6	0.589
Mean	**0.592**
Standard deviation	**0.0042**

Table 6.1 summarizes the results of the thermal conductivity for the one set of measurements performed by the independent measurement on the test sample of water. The thermal conductivity values presented here are the values calculated for each measurement as the average of five values, obtained from a least square-fit of the linear part of the ΔV vs ln(t). The average thermal conductivity results as well as the calculated standard deviation are summarized in Table 6.1.

The relative standard deviation value in Table 6.1 represents first type of uncertainty. It can be conducted that the value 0.71% represents first type of uncertainty component. The manufacturer specifies the stability in the data acquisition time system. The uncertainty is better than 0.01%. The error is so small that we do not have to consider it as a source of the thermal

conductivity uncertainty. But we calculate the thermal conductivity using the slope of the ΔV vs ln(t), the influence of the uncertainty of the thermal conductivity is better than 0.1%.

In the measurement, we let the stabilized direct current flow through the platinum heating wire. The current is produced by the stabilized power source (SMU 2450) working in the stabilized current supply mode. The manufacturer specifies the current stability at the level of 0.05%. The influence on the thermal conductivity uncertainty is less than 0.1%.

All the components of the uncertainty are considered to be independent. Using the law of uncertainty propagation we can ensure that the combined standard uncertainty of the thermal conductivity is better than 1.1%.

Permissions for Content Reused

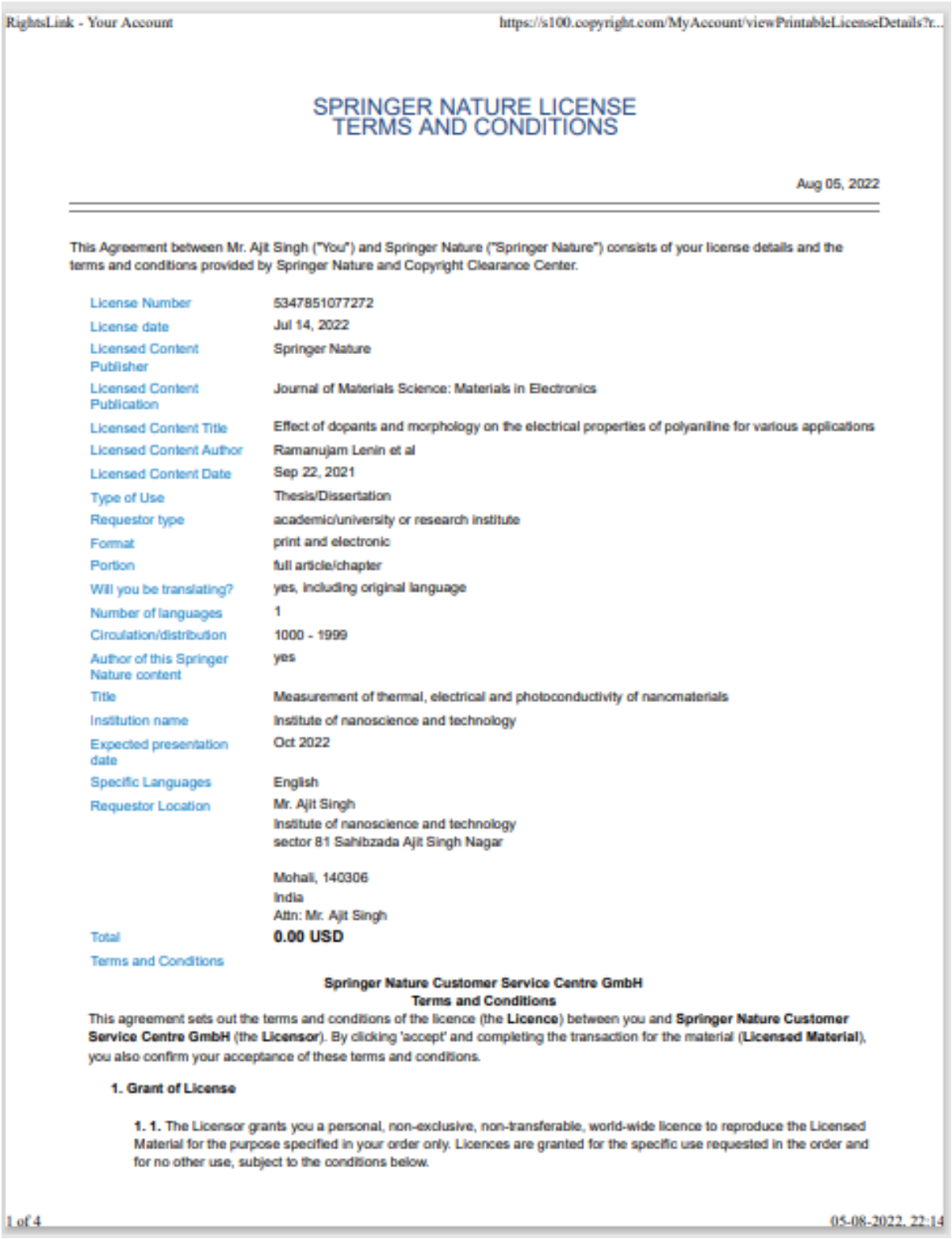

RightsLink - Your Account https://s100.copyright.com/MyAccount/viewPrintableLicenseDetails?r...

SPRINGER NATURE LICENSE TERMS AND CONDITIONS

Aug 05, 2022

This Agreement between Mr. Ajit Singh ("You") and Springer Nature ("Springer Nature") consists of your license details and the terms and conditions provided by Springer Nature and Copyright Clearance Center.

License Number	5347851077272
License date	Jul 14, 2022
Licensed Content Publisher	Springer Nature
Licensed Content Publication	Journal of Materials Science: Materials in Electronics
Licensed Content Title	Effect of dopants and morphology on the electrical properties of polyaniline for various applications
Licensed Content Author	Ramanujam Lenin et al
Licensed Content Date	Sep 22, 2021
Type of Use	Thesis/Dissertation
Requestor type	academic/university or research institute
Format	print and electronic
Portion	full article/chapter
Will you be translating?	yes, including original language
Number of languages	1
Circulation/distribution	1000 - 1999
Author of this Springer Nature content	yes
Title	Measurement of thermal, electrical and photoconductivity of nanomaterials
Institution name	Institute of nanoscience and technology
Expected presentation date	Oct 2022
Specific Languages	English
Requestor Location	Mr. Ajit Singh Institute of nanoscience and technology sector 81 Sahibzada Ajit Singh Nagar Mohali, 140306 India Attn: Mr. Ajit Singh
Total	**0.00 USD**
Terms and Conditions	

Springer Nature Customer Service Centre GmbH
Terms and Conditions

This agreement sets out the terms and conditions of the licence (the **Licence**) between you and **Springer Nature Customer Service Centre GmbH** (the **Licensor**). By clicking 'accept' and completing the transaction for the material (**Licensed Material**), you also confirm your acceptance of these terms and conditions.

1. Grant of License

1. 1. The Licensor grants you a personal, non-exclusive, non-transferable, world-wide licence to reproduce the Licensed Material for the purpose specified in your order only. Licences are granted for the specific use requested in the order and for no other use, subject to the conditions below.

1 of 4 05-08-2022, 22:14

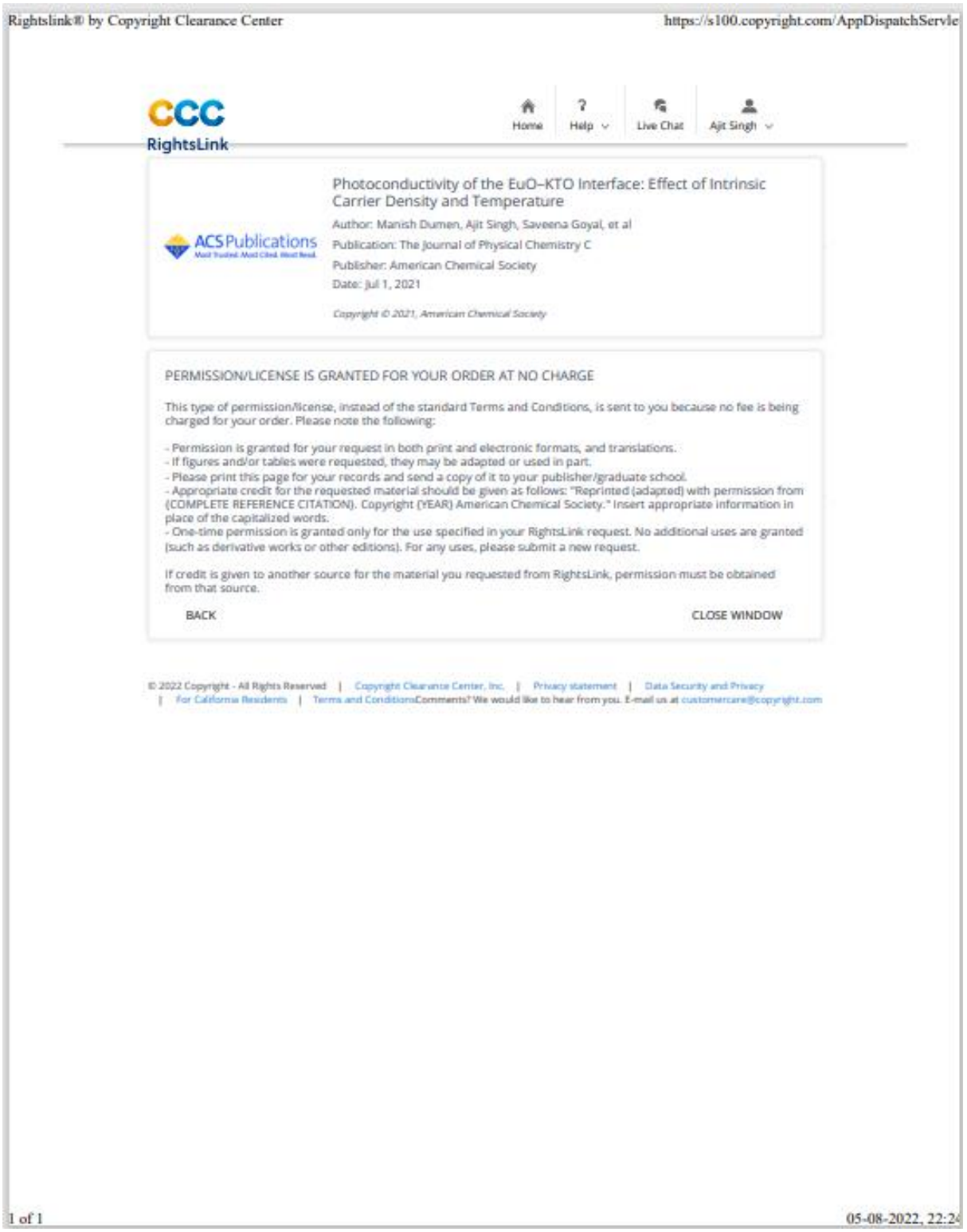

Rightslink® by Copyright Clearance Center https://s100.copyright.com/AppDispatchServle

CCC RightsLink

Home | Help | Live Chat | Ajit Singh

ACS Publications

Photoconductivity of the EuO–KTO Interface: Effect of Intrinsic Carrier Density and Temperature

Author: Manish Dumen, Ajit Singh, Saveena Goyal, et al

Publication: The Journal of Physical Chemistry C

Publisher: American Chemical Society

Date: Jul 1, 2021

Copyright © 2021, American Chemical Society

PERMISSION/LICENSE IS GRANTED FOR YOUR ORDER AT NO CHARGE

This type of permission/license, instead of the standard Terms and Conditions, is sent to you because no fee is being charged for your order. Please note the following:

- Permission is granted for your request in both print and electronic formats, and translations.
- If figures and/or tables were requested, they may be adapted or used in part.
- Please print this page for your records and send a copy of it to your publisher/graduate school.
- Appropriate credit for the requested material should be given as follows: "Reprinted (adapted) with permission from (COMPLETE REFERENCE CITATION). Copyright (YEAR) American Chemical Society." Insert appropriate information in place of the capitalized words.
- One-time permission is granted only for the use specified in your RightsLink request. No additional uses are granted (such as derivative works or other editions). For any uses, please submit a new request.

If credit is given to another source for the material you requested from RightsLink, permission must be obtained from that source.

BACK CLOSE WINDOW

© 2022 Copyright - All Rights Reserved | Copyright Clearance Center, Inc. | Privacy statement | Data Security and Privacy | For California Residents | Terms and ConditionsComments? We would like to hear from you. E-mail us at customercare@copyright.com

1 of 1 05-08-2022, 22:24

For RSC journals like Nanoscale Advances, "**permission is not required**" to reuse the whole article for **thesis/dissertation** as highlighted below. Two articles published in Nanoscale Advances have gone into the thesis.

Mechanistic insights into surface contribution towards heat transfer in a nanofluid

A. Singh, R. Lenin, N. K. Bari, C. Bakli and C. Bera, *Nanoscale Adv.*, 2020, **2**, 3507 **DOI:** 10.1039/D0NA00452A

Biomass-derived cellulose nanofibers and iron oxide-based nanohybrids for thermal insulation application

S. Sen, A. Singh, K. Kailasam, C. Bera and S. Roy, *Nanoscale Adv.*, 2022, Advance Article , **DOI:** 10.1039/D2NA00010E